Computed Tomography

Advances in Research and Applications

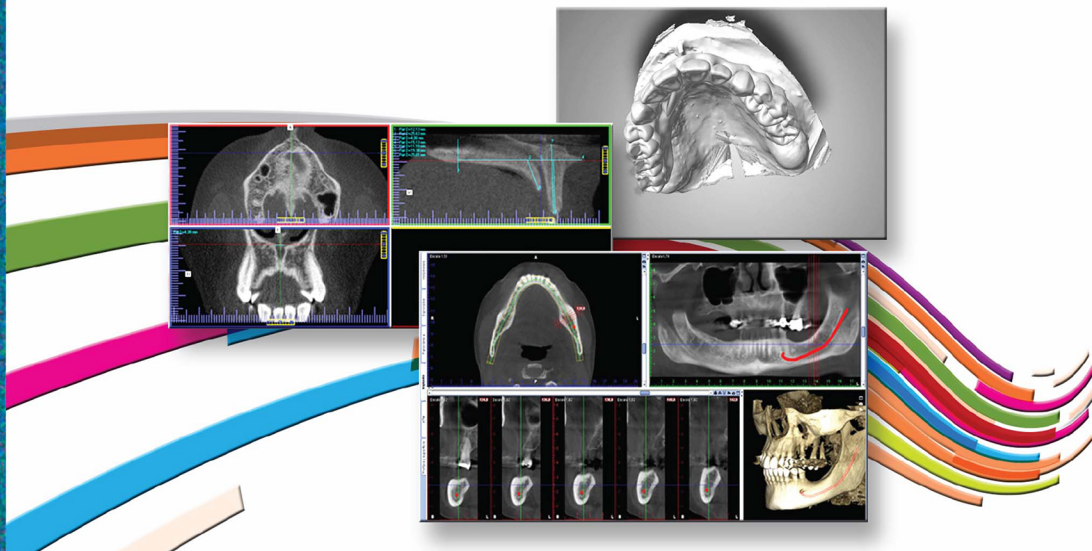

Deborah Carter
Editor

Medical Procedures, Testing and Technology

Novinka

Nova Biomedical

MEDICAL PROCEDURES, TESTING AND TECHNOLOGY

COMPUTED TOMOGRAPHY

ADVANCES IN RESEARCH AND APPLICATIONS

MEDICAL PROCEDURES, TESTING AND TECHNOLOGY

Additional books in this series can be found on Nova's website under the Series tab.

Additional e-books in this series can be found on Nova's website under the eBooks tab.

MEDICAL PROCEDURES, TESTING AND TECHNOLOGY

COMPUTED TOMOGRAPHY

ADVANCES IN RESEARCH AND APPLICATIONS

DEBORAH CARTER
EDITOR

nova biomedical
New York

Library of Congress Cataloging-in-Publication Data

Names: Carter, Deborah, editor.
Title: Computed tomography : advances in research and applications / editor, Deborah Carter.
Description: Hauppauge, New York : Nova Science Publisher's, Inc., [2017] | Series: Medical procedures, testing and technology | Includes bibliographical references and index.
Identifiers: LCCN 2016058973 (print) | LCCN 2017005049 (ebook) | ISBN 9781536107661 (softcover) | ISBN 9781536107852 (ebook) | ISBN 9781536107852 (eBook)
Subjects: LCSH: Diagnostic imaging--Research. | Tomography. | Imaging systems in medicine.
Classification: LCC RC78.7.D53 C657 2017 (print) | LCC RC78.7.D53 (ebook) | DDC 616.07/54--dc23
LC record available at https://lccn.loc.gov/2016058973

Published by Nova Science Publishers, Inc. † New York

CONTENTS

Preface		**vii**
Chapter 1	Strategies for Computer-Aided Designing of Surgical Guides for Dental Implant Procedures Based on Cone Beam Computed Tomography *Piotr Malara and Lech B. Dobrzanski*	**1**
Chapter 2	Anatomic Variations of Mandibular Canal and Mental Foramen: An In-Depth Analysis Using Cone Beam Computed Tomography *J. Muinelo-Lorenzo, A. Fernández Alonso and M. M. Suárez-Cunqueiro*	**23**
Chapter 3	Accurate Analysis of Nasopalatine Canal Using Cone Beam Computed Tomography *A. Fernández-Alonso, J. Muinelo-Lorenzo and M. M. Suárez-Cunqueiro*	**45**
Chapter 4	An Assessment of Morphometric Characteristics of the Greater Palatine Canal Using Cone Beam Computed Tomography *O. Rapado-González, J. C. Pérez-Varela and M. M. Suárez-Cunqueiro*	**67**
Chapter 5	Using High Resolution Computed Tomography Images to Assess the Risks of Pathological Change of Pulmonary Parenchyma *Hongyang Jiang, He Ma and Mengdi Gao*	**89**
Index		**109**

PREFACE

This book provides new research on computed tomography. Chapter One presents strategies for computer-aided designing of surgical guides for dental implant procedures based on cone beam computed tomography (CBCT). Chapter Two gives an in depth analysis of using CBCT in anatomic variations of the mandibular canal and the mental foramen. Chapter Three discusses the use of CBCT for an accurate analysis of the nasopalatine canal. Chapter Four reviews the use of CBCT to assess morphometric characteristics of the greater palatine canal. Chapter Five reviews and discusses the application of state-of-art content based image retrieval schemes in pathological risk analysis of lung computed tomography images.

Chapter 1 – Reconstruction of missing teeth with dental implants is a frequently used procedure in the rehabilitation of the stomatognathic system. An important factor in the success of the therapy, is proper planning of the implant position in the alveolar bone using three-dimensional imaging. The transfer of the planned position of the implants in the patient's mouth during surgery is a difficult stage in the procedure. This chapter presents the design strategies for surgical guides based on CBCT and scans of the intraoral situation. The use of these guides during surgical procedures helps to carry out the implant placement in a predictable, fast and minimally invasive manner. It also helps to increase the predictability and safety of the treatment, to reduce pain and to shorten the recovery time after surgery.

Chapter 2 – Cone beam computed tomography (CBCT) is increasingly being used as a diagnostic tool in dentistry, especially in the field of oral surgery. Its high resolution three dimensional images reveal anatomic structures more clearly.

The mandibular canal hosts the inferior alveolar nerve and vessels, which are critical anatomic structures for surgical procedures. The mandibular canal in several cases doesn't appear uniformly as a single canal, it may present various branching patterns. These bifid mandibular canals must be taken into consideration to avoid clinical complications.

A number of classifications have been developed on anatomic and panoramic radiography surveys. However, the true incidence of bifid mandibular canal is underestimated on panoramic images due to the two-dimensional nature of panoramic radiography. The overlap of anatomic structures such as soft palate, airway, milohioid groove, and submandibular fossa may interfere with the visualization of these neurovascular bifid canals. Also, the buccolingual type of canals may be missed on panoramic images, but can be easily identified on CBCT images. CBCT allows for better depiction of small vascular canals regardless trabecular pattern.

The mental foramen is a bilateral opening in the anterolateral region of the mandible through which the mental nerve emerges. The mental nerve represents one of the terminal branches of the inferior alveolar nerve, and supplies the lower lip, cheeks, chin, and the vestibular gingiva of mandibular incisors. Although the mental foramen is one of the most important neurovascular landmarks in the anterior mandible, its identification is not always possible using panoramic radiographs. The visualization on panoramic images is influenced by mental foramen size, trabecular pattern, mental foramen emergence, and patient's age. However, a CBCT image improves mental foramen depiction, offering advantages over two-dimensional radiological images.

The mental foramen usually remains as a single structure, however in some cases, the mental nerve branches before exiting the mandible originating small foramina in the area surrounding the mental foramen known as accessory mental foramina. This anatomic landmark is not rare, it has been reported a rate of occurrence up to 20% in CBCT studies, and its position is crucial for surgical procedures involving this region, such as surgical rehabilitation after mandibular trauma, bone harvesting from the chin, root resection of mandibular premolars, and particularly for dental implants placement.

An accessory mental foramen located above the mental foramen directly affects the treatment planning using dental implants, since their position may limit surgical procedures. This was found in up to 4% of the population, which means it is necessary to consider these accessory foramina to the main mental foramen. An accessory mental foramen located closely to the apex of the

lower teeth can simulate false periapical pathology. By using the CBCT, continuity with the mandibular canal can be easily identified which avoids unnecessary damage. Therefore, a CBCT image examination may be a very important aid before surgical treatments in the mandible.

Chapter 3 – The nasopalatine canal is an anatomic limitation that interferes with implant placement when ridge resorption is present. The nasopalatine canal is connected to the nasal cavity through the foramina of Stenson, and to the oral cavity through the incisive foramen. The nasopalatine canal contains the terminal branch of the descending nasopalatine artery and the nasopalatine nerve. Due to nasopalatine canal anatomy being highly variable, for dental implant treatment planning and placement, a precise anatomic description is necessary.

The critical region anterior to the nasopalatine canal is defined as an anatomic area that should not invaded surgically, to avoid neurovascular complications and failure of implant osseointegration. Due to bone ridge resorption after tooth loss, the nasopalatine canal can occupy up to 58% of buccal plate width, the area available for implant placement. This critical region may be evaluated with accuracy three dimensionally using cone beam computed tomography (CBCT) to ensure proper implant position.

This chapter shows the morphometric characteristics of the nasopalatine canal, the nasopalatine angle, the dimensions of the buccal bone plate, and the palatal bone plate relative to the nasopalatine canal. This description is based on the analysis of three anatomic planes by CBCT.

Chapter 4 – Lorem ipsum dolor sit amet, consectetuer adipiscing elit. Maecenas porttitor congue massa. Fusce posuere, magna sed pulvinar ultricies, purus lectus malesuada libero, sit amet commodo magna eros quis urna. Nunc viverra imperdiet enim. Fusce est. Vivamus a tellus. Pellentesque habitant morbi tristique senectus et netus et malesuada fames ac turpis egestas. Proin pharetra nonummy pede. Mauris et orci. Cone Beam Computed Tomography (CBCT) is a useful tool for evaluating the greater palatine canal morphometrically on the three anatomic planes. The greater palatine canal is located in a critical anatomic area and has a great clinical relevance. The pterygopalatine fossa is connected to the oral cavity by the greater palatine canal. The pterygopalatine fossa contains the maxillary nerve, the maxillary artery, the venous rami and the pterygopalatine ganglion. The palatine nerves descend since pterygopalatine fossa through the greater palatine canal. The greater palatine nerve emerges on the palate through the greater palatine foramen and the lesser palatine nerves emerge through the lesser palatine foramina. The position of the greater palatine foramen is of great interest to

dentists, maxillofacial surgeons and otolaryngologists for anesthetic purposes, and also for obtaining connective tissue grafts for periodontal purposes. The greater palatine canal allows blocking of the maxillary nerve and therefore allows anesthesia of the sinus, the maxillary teeth, the tissue palatal and the nasal region. Due to the greater palatine foramen being hidden by palatal mucosa thickness, a clinical and radiological location is necessary for treatment planning of several oral surgical procedures. CBCT images of the greater palatine foramen describe the dimensions and position of each greater palatine foramen with respect to different landmarks. An exact location of the greater palatine foramen is necessary to avoid damaging the greater palatine neurovascular bundle. Morphometric classifications of the greater palatine canal are important to applying anesthesia correctly and to avoid hemorrhagic risks. It is necessary to keep in mind that the greater palatine canal is a bone structure with numerous morpho-anatomical variations. The anatomy of the greater palatine canal can be a limiting factor in the block of the maxillary nerve. Nowadays, CBCT images provide an exhaustive anatomic description of the greater palatine foramen and the greater palatine canal in the axial, sagittal and coronal slices.

Chapter 5 – Lung cancer is one of the most concerned diseases around the world. Generally, its mortality is very high because the malignant tissue of lung cannot be checked out timely. Once cancerous cells in pulmonary parenchyma are detected in the early stage, the cure rate can be enhanced. A large collection of high resolution computed tomography (CT) images and their diagnostic information make it possible to analyze a new suspected case based on these historical data using data mining technologies. Although lung CT images provide us much valuable pathological information about cancerization,it is tough to extract and utilize it directly due to its irregularity in content. Thus, applying the current content based image retrieval (CBIR) schemes to assess a medical image can produce an exciting and promising effect. In this chapter, we will review and discuss the application of the state-of-art CBIR schemes in pathological risk analysis of lung CT images.

In: Computed Tomography
Editor: Deborah Carter
ISBN: 978-1-53610-766-1

Chapter 1

STRATEGIES FOR COMPUTER-AIDED DESIGNING OF SURGICAL GUIDES FOR DENTAL IMPLANT PROCEDURES BASED ON CONE BEAM COMPUTED TOMOGRAPHY

Piotr Malara[1,*] and Lech B. Dobrzanski[2]
[1]Institute of Engineering Materials and Biomaterials,
Silesian University of Technology, Gliwice, Poland
[2]Centre of Medicine and Dentistry SOBIESKI, Gliwice, Poland

ABSTRACT

Reconstruction of missing teeth with dental implants is a frequently used procedure in the rehabilitation of the stomatognathic system. An important factor in the success of the therapy, is proper planning of the implant position in the alveolar bone using three-dimensional imaging. The transfer of the planned position of the implants in the patient's mouth during surgery is a difficult stage in the procedure. This chapter presents the design strategies for surgical guides based on CBCT and scans of the intraoral situation. The use of these guides during surgical procedures helps to carry out the implant placement in a predictable, fast and minimally invasive manner. It also helps to increase the predictability and

[*]Corresponding author email: malara@dentaris.pl

safety of the treatment, to reduce pain and to shorten the recovery time after surgery.

Keywords: surgical guides, guided surgery, dental implants, cone beam computed tomography

INTRODUCTION

Implantoprosthetic treatment is becoming a very popular form of treatment for patients with missing teeth (Bornstein et al., 2008). Traditional prostheses replace only the occlusal surface or an anatomical crown of the lost teeth (Silveira Rodrigues et al., 2013). In these prosthetic appliances, the transmission of occlusal forces take place through the oral mucosa or periodontium of the remaining teeth (Bornstein et al., 2008). Thus, transmission of the chewing forces in traditional prosthetic restorations is carried out in a non-physiological manner. This is because soft tissues are not adapted to transfer the chewing forces. Loading the oral soft tissues with dentures which carry on repeated bite load, often leads to micro-injuries, inflammations, fungal, bacterial and viral infections. In addition, the mucosa, when subjected to occlusal loads, undergoes involution and thinning due to compression of blood vessels. The mucosal load gets deeper into the alveolar bone and the process may lead to bone loss and consequently, deficits of the prosthetic field. It should be noted that the prostheses supported by the oral mucosa are mobile and must be removed by the patient at least for hygienic procedures. Such prostheses are perceived as uncomfortable and awkward in many cases (Silveira Rodrigues et al., 2013). Prosthetic restorations supported by periodontium of the remaining dentition also lead to non-physiological loading as a result of occlusal loading. This may lead to some degree of overload of the teeth and consequently, loosening and loss. Prostheses supported by periodontium are often fixed, that is, attached permanently to the residual dentition of the patient (Silveira Rodrigues et al., 2013). They cannot be taken out of the mouth by the patient. In addition to the adverse impact on the residual dentition, fixed dentures cannot be modified and expanded in most cases. The prosthesis must be manufactured again; this is time-consuming and it involves expensive treatment procedures.

The major solutions in reconstructive dentistry which, in addition to restoring the lost tooth crown also rebuilds its root, are implantoprosthetic restorations (Ramos et al., 2015). The basic element in these reconstructions is

the dental implant. It is an element in the shape of a cylinder or a cone with a threaded surface which is placed in the alveolar bone. This element is made of a biocompatible material, which nowadays in most cases is either titanium or an alloy of titanium, aluminum and vanadium. Zirconium dioxide is also often used in modern dentistry. Biocompatibility of the materials means that the human body does not recognize the material that make up the appliances and therefore treats it as a foreign body. It does not trigger a cascade of immune mechanisms that are responsible for the rejection of the implanted material. Thus, the alveolar bone heals around a dental implant in an undisturbed way. This leads to a fully functional connection between the bone and the implant. This process is called osseointegration (Javed and Romanos, 2010; Heinemann et al., 2015). The prerequisite for the process of osteointegration, is a minimum of 1mm thickness of the bone around the implant (Javed and Romanos, 2010). Therefore, it is extremely important to choose the correct location for the placement of the implant. In cases of alveolar bone deficits, it is necessary to carry out additional procedures aimed at augmenting the alveolar bone and restoring the place to host the implant (Malara, 2013).

The dental implant is an artificial tooth root, through which occlusal forces are transferred to the alveolar bone. An implant abutment is attached to the implant. It is a part that passes through the alveolar mucosa and enables attachment to the prosthetic suprastructure. There are many types of prosthetic superstructures. These may include crowns or bridges and overdentures.

It should be noted that the biomechanics of dental implants is not completely identical with the natural biomechanics of the teeth (Ramos et al., 2015). In the case of natural teeth, there is no direct connection between the bone and the surface of the root. Between these two structures, there is an intermediary tissue called periodontium. Periodontal membrane absorbs occlusal forces and can regulate the masticatory muscle activity in the feedback mechanism due to the presence of proprioreceptors. Hence, the load is transmitted to the teeth. In the case of implants, there is a direct connection between the bone and the implant and there is no connective tissue with proprioreceptors between the two layers. Therefore, there is no mechanism that regulates the chewing forces and no tissue to cushion these forces. Thus, the implantoprosthetic restorations may be exposed to an overload of occlusal forces (Silveira Rodrigues et al., 2013).

As stated above, the existence of a layer of the bone surrounding the implant with a minimum thickness of 1mm is a prerequisite for osseo-integration at the implantation site. Furthermore, it is very important to place the implant at a site and avoid damaging the neighbouring anatomical

structures. This mainly affects the inferior alveolar nerve in the mandible. A damage to the nerve leads to unpleasant sensory disorders in the lower lip. For the maxilla, attention must be paid to the location of maxillary sinus and the floor of the nasal cavity. Failure to maintain an appropriate distance from these structures may cause perforation, inflammation and functional disorders (Liaw et al., 2015).

A classic approach to determining the location for implant placement involves the execution of two-dimensional images of the jaw bones. The images are primarily panoramic x-rays, which are a summation of the visualized curved jaw bone structures on the plane. They allow an assessment of the vertical dimension available in the alveolar bone. It is possible to perform the measurements of the distance from the top of the alveolar ridge to the floor of the maxillary sinus, the floor of the nasal cavity and the inferior alveolar nerve canal (Dreiseidler et al., 2009). These measurements must be supplemented by intraoral measurement of the width of the alveolar process at the site of implantation. The measurement is done by subtracting from the total width of the alveolar ridge and the thickness of the mucous membrane covering the bone at the place (Perez et al., 2005). In order to perform these measurements, it is necessary to obtain the plaster model of the jaw, which is cut in width at the site of the planned implant placement (Figure 1). Then, it is necessary to create a template on which the sites of thickness measurements are marked. Oral mucosa is anesthetized and a previously formed template is introduced to the oral cavity. Then, at the respective measuring points the mucosa is pierced with a sharp probe until it reaches the surface of the bone (Figure 2). The readings of the thickness of the mucosa is transferred to the cross-section of the cast which makes the plotting of a cross-sectional outline of the bone possible (Figure 3). It should be noted that this study is relatively invasive, time consuming and subject to measurement error.

Implantological assessment most times requires the use of computed tomography to check the three-dimensional anatomy of the alveolar process before implant placement procedures (DeVos et al., 2009). For dental imaging, cone beam computed tomography (CBCT) is commonly used. The three-dimensional tomographic examination makes it possible to measure the available alveolar bone in vertical and transversal dimensions without additional clinical procedures (Cyganek and Siebert, 2009).

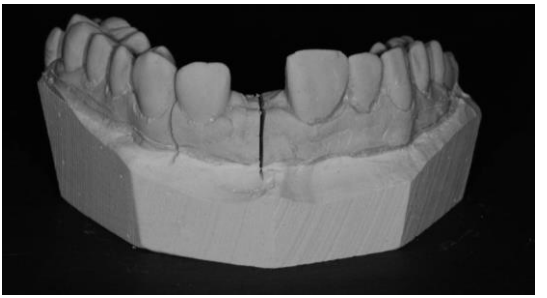

Figure 1. The plaster model of the jaw is cut in width at the site of the planned implant placement.

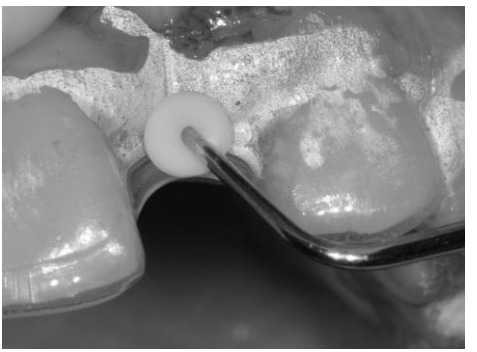

Figure 2. The mucosa is pierced with a sharp probe until it reaches the surface of the bone at the respective measuring points.

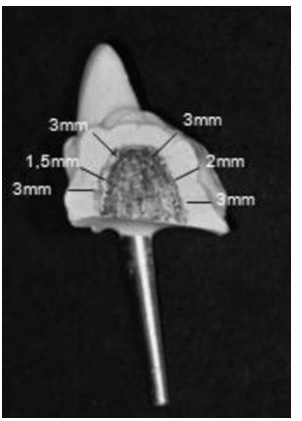

Figure 3. The readings of the thickness of the mucosa are transferred to the cross-section of the cast which allows plotting a cross-sectional outline of the bone.

With the development of modern imaging techniques, there has been a change in the approach to implantological treatment planning. In the past, it involved placing the implants at the most surgically suitable position of the alveolar process. That is, at places where there was sufficient volume of bone tissue. This approach was called "surgically-driven implantology". Unfortunately, in many cases, this approach turned out wrong from the perspective of a prosthetic suprastructure. Therefore, the present approach is applied to the reverse. First, the future design of the prosthetic restoration is planned, and only then is the location and a number of the implants adjusted. This approach is called "prostetically-driven implantology" (Papaspyridacos et al., 2012).

The planning of the restoration and position of the necessary implants are both performed virtually on the computer screen based on data from CBCT scans and the registered intraoral situation. The problem is to transfer the planned position of the implants to the patient's mouth during surgery (Greenberg, 2015; Meloni et al., 2014; Giordano et al., 2012). One of the possible methods is the use of surgical guides - appliances which allow for accurate drilling during preparation of the implant bed in bone. The drill is conducted through special holes in the surgical guide. As a result, the implant is placed in the alveolar bone in a pre-planned position (Mora et al., 2014).

The aim of this paper is to present strategies developed for designing surgical implant guides based on CBCT and scans of the intraoral situation. Strategies will be presented based on the real clinical case of a patient who has a significant deficit of alveolar bone previously subjected to augmentation procedures to improve the conditions for the implant placement.

APPLICATION OF CAD/CAM TECHNOLOGY TO DESIGNING AND MANUFACTURING OF SURGICAL IMPLANT GUIDES

The use of CAD/CAM technology makes it possible to produce a surgical guide that will not only allow the placement of the implants after the previously designed one on the basis of CBCT scans path, but also, function as a mock-up with the use of appropriate mounting screws - as immediate restoration. To do this, it is necessary to apply suitable materials which provide appropriate aesthetics of the whole appliance in the production process, and to ensure that the system that attaches the template to the

previously introduced implants uses plugs to close the pilot drill holes (Henriques et al., 2012; Mugoni et al., 2015; Roht et al., 2016)).

More time is taken to implement procedures for preparing a patient for the implantation procedure by carrying out early, routine CBCT examination. On the basis of CBCT, the bone anatomy can be assessed and the position of the implant may be planned together with the future design of the prosthetic suprastructure (Galanis et al., 2007). This way, common errors associated with the placement of dental implants outside the dental arch or at the place which makes it impossible to provide a satisfactory appearance of the whole prosthesis can be avoided. This procedure can be used both in cases of single tooth loss as well as multiple teeth or edentulous cases.

Production of the surgical guide requires close collaboration between an engineer and a dentist in the area of:

1. Designation of the areas of the alveolar process where dental implants can be placed from the clinical point of view.
2. Determination of the planned design of the restoration at the end of the treatment and the paths along which the dental implants can be favourably introduced from aesthetic point of view (using teh mock-up or traditional wax-up techniques).
3. Manufacturing a three-dimensional model of the base of the alveolar bone based on CBCT.
4. Combining the three-dimensional model of the alveolar bone with a three-dimensional model of the teeth and soft tissue in the oral cavity prepared on the basis of traditional intraoral impressions or a three-dimensional scan taken directly in the mouth.
5. Manufacturing the project of the restoration on the basis of a three-dimensional model of teeth and soft tissue in the mouth
6. Planning the placement of implants using a model created in point 4 and the three-dimensional project of the restoration from point 5.
7. Planning technological holes for guiding the pilot drill adjustment to the specific implant system.
8. Designing the final surgical guide.
9. Selection of the material from which the surgical guide will be made.
10. Manufacturing of the guide with 3D printing or CAD/CAM technology.

The stages described above require close cooperation between an implantologist and a dental engineer. Only the cooperation of the entire team at every step of the surgical guide production can develop the optimal design, taking into account all aspects shown earlier. In everyday practice, the planning of implant treatment is often done solely on CBCT without using a design software to ensure optimal technical effects (for example sufficient length of the implant abutments) and aesthetics. The proposed strategy varies widely from everyday practice. The dentist plans the whole treatment and the dental technician is supposed to produce only the final prosthesis. This strategy is proposed to promote the team work between the dental engineer and the dentist. They would have to develop a surgical guide at the planning stage and collaborate closely with the clinician until the final restoration has been made.

The dental engineer, using available engineering software is required to complete the following tasks:

- correct creation of a 3D model of the alveolar bone based on CBCT
- correct selection of parameters and generation of the model related properly to the model of soft tissue and teeth
- verification of implant treatment plan presented by implantologist in terms of endurance of the planned restoration on the basis of available materials
- verification of the correct location of the implants based on the combined two models: the model of alveolar bone and intraoral model
- proper selection of material to prepare a guide
- manufacturing of the guide based on CAD/CAM technology.

The range of clinical tasks during the preparation of the surgical guide is limited to an assessment of the situation in the mouth and an assessment of the quality of the bone. Implantologist must ensure that the patient qualifies for an implant treatment and specify the scope restorative constructions (for example fixed or removable solutions with regard to the number of implants).

Properly prepared surgical guides will accelerate the implantation procedure, reduce invasiveness, shorten recovery time of the patient and allow the preparation of the restoration without traditional impressions. In certain cases, it will also allow production of suprastructures for immediate implant loading.

CONVERSION OF DIGITAL IMAGING AND COMMUNICATIONS IN MEDICINE FORMAT TO STEREOLITHOGRAPHY FORMAT

For the success of the whole procedure, it is extremely important to properly convert the data from CBCT stored in DICOM format (ang. Digital Imaging and Communications in Medicine) in the form of slices defined by the resolution of the CBCT machine (usually from 100 to 200 micrometers) to three-dimensional stereolithography format (STL) used in software design (CAD) and manufacturing (CAM) (Almog et al., 2001).

It is also important to ensure proper quality of the CBCT scan. Due to limitations in the construction of detectors, the standard resolution of the CBCT machine oscillates within the range of 100-300 microns and in the case of imaging of the entire skull, it is up to 500 microns. As a result of the additional processing of the image in post-production, it is possible to achieve a greater resolution, but in most cases the image quality is poor. Resolution of 200 micrometers is sufficient for diagnosis in almost every clinical case. The values of radiation that reach the detectors are processed to be displayed in grayscale using rays to pass the useful values (VOI LUT). They provide definitions of the data module, which matches the values stored in the software to those that are to be displayed on the monitor screen.

Before creating the three-dimensional model, the DICOM format image must be filtered in order to select the processing area of the bone where the implants should be placed. Filtration is carried out by analyzing the image histogram, which is a vector with the number of elements equal to the number of existing levels of brightness. Subsequent elements of the histogram hist (q) determine the cardinality of the pixel brightness q (Figures 4 and 5). A tomogram contains information describing the space in the shape of a cylinder of a certain size (in this case, it is a cylinder with a height of 4 cm and 6 cm in diameter). This contains data that describe the space around the patient as well as information about the soft tissues and about the bone, which is in the area of interest. After extracting the area of interest and performing a visual inspection of the displayed data, it is possible to generate three-dimensional model in a format stereolithography (STL). This is widely used in manufacturing procedures. Files saved in STL format describe the body as a triangular mesh with a predefined deviation, which should be less than the minimum precision of the milling machine used to produce the final product.

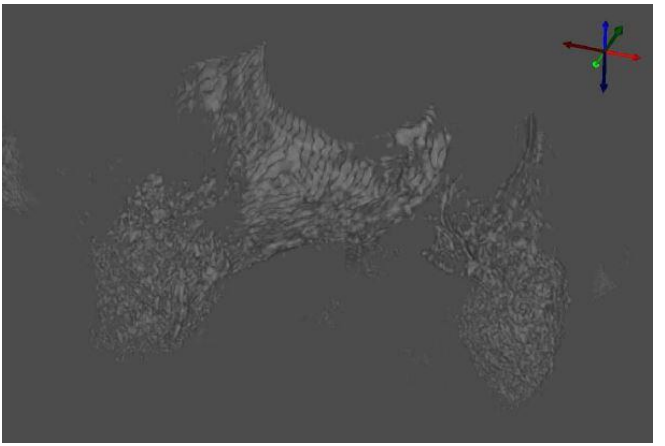

Figure 4. A 3-D image of the bone achieved by manual adjustment of the histogram under visual control.

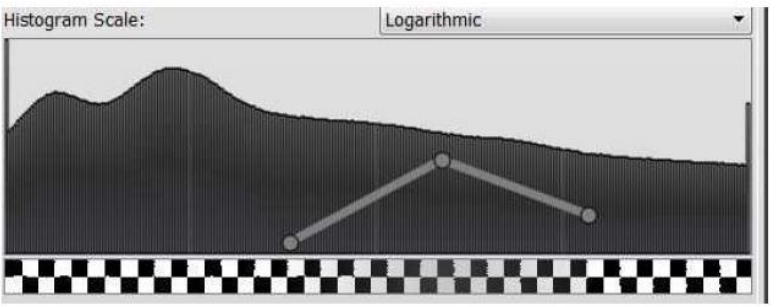

Figure 5. A histogram scale used for the reconstruction of a 3D image of the bone.

An important issue related to combining the model of the bone in STL format and the intraoral situation registered by traditional impressions or an intraoral digital scan is to provide the appropriate reference points which will allow proper combination of these two models. This is a step which requires some technical and clinical expertise.

STRATEGIES FOR DESIGNING THE SURGICAL GUIDES

It is possible to distinguish two methods of combining the model of the alveolar bone (Figure 6) from the model of intraoral situation (Figure 7) using:

1. Geometrical external markers.
2. Integrated internal markers.

Figure 6. Model of the alveolar bone achieved from CBCT.

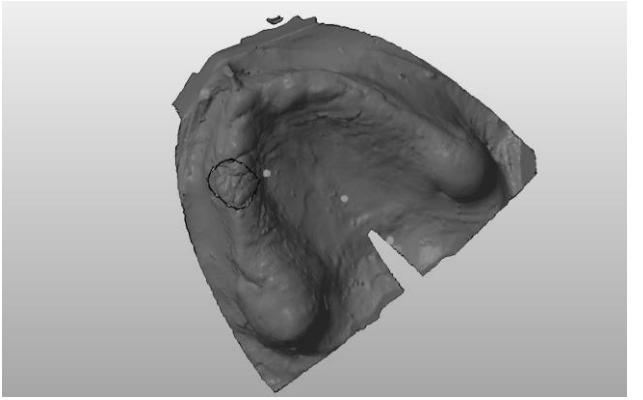

Figure 7. Model of the intraoral situation achieved from digital intraoral scans.

The first method involves the use of physical geometrical markers (minimum of 3), which need to be installed on the oral mucosa (Figure 8) or teeth adjacent the area of implantation using a temporary cement or gutta-percha before taking CBCT images (Figure 9). The markers need to be scanned at the same time in the oral cavity. During the combination process, the markers enable proper superimposition of the images. It is important that both CBCT and the intraoral scans are taken nearly at the same time, because even the smallest shift of the markers' position will affect the accuracy of mapping.

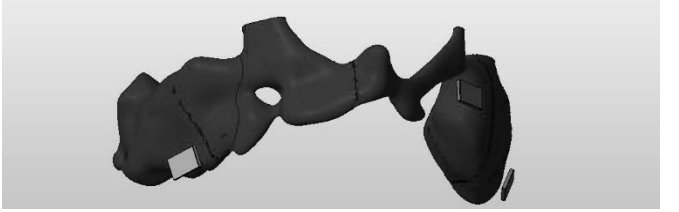

Figure 8. Markers visible on the STL model of the bone.

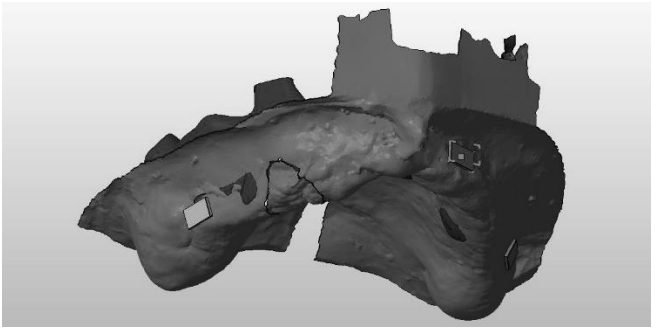

Figure 9. Markers visible on the model of the intraoral situation.

Also, it is advisable to use intraoral scans instead of traditional impressions. By doing so, it will be possible to scan the markers intraorally. The markers can also be placed on the plaster models. However, in this case, the risk of error is greater. The most important issue is to ensure that the markers remain in the impression mass, so that the same physical markers may be placed on the model. This is necessary because of the relatively low accuracy when mapping the cast sharp edges, especially at the stage of releasing the plaster model from the impression material. Thus, the models can be connected virtually to the images obtained from CBCT.

The other method is based on the use of characteristic points of reference located on the model of the bone and also the model of the intraoral situation. A dental engineer must determine these points at the beginning of the procedure. If there is a patient with residual dentition, this procedure requires selecting characteristic points of the teeth adjacent to the implant area that is clearly visible on both sides of the area for the planned implantation. Points that are at some distance to the implantation area which will serve as the reference points have to be determined. For the upper teeth, a good reference point is the middle point of *torus palatinus* as it is covered with a very thin layer of soft tissue (Figure 10) - basically with negligible thickness - which

allows for precise positioning of both models along the lines defined by the anatomical structure. This solution is specially recommended for restorations of edentulism where there is no possibility of finding other markers. In the case of the lower teeth, this method is impossible. The designer must look for areas where the mucosa is very thin. It is usually where the patient has had no teeth for many years. It is also possible to use the areas that have been subjected to load and exerted by removable dentures. If the areas fulfilling the criteria described above cannot be found, it is necessary to use the first method. For the second method, it is is very important that the designer has some experience in finding proper reference points. At the same time, the model of the bone must include a merger of the soft tissue and the hard tissue.

The models with visible markers prepared in the way described above should be superimposed with the use of designing software. This is going to be the digital master cast on which the prosthetic suprastructure as well as the surgical guide will be designed.

The designing process must start with the determination of the position of the upper (maxillary) and the lower (mandibular) models in the central occlusion position. Then, the shape of the dental arch (Figure 11) and the shape of the artificial teeth (Figure 12) are designed. The relation of the teeth against the opposing dentition must be checked (Figure 13). At this stage, consideration should be given to the characteristics of the material from which the final restoration will be made so as to not to reach the minimum thickness and be made permanent.

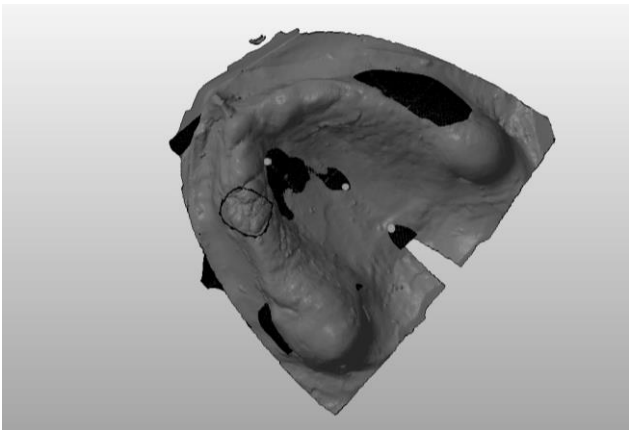

Figure 10. Reference points along *torus palatinus* at the area of very thin mucosa covering the bone.

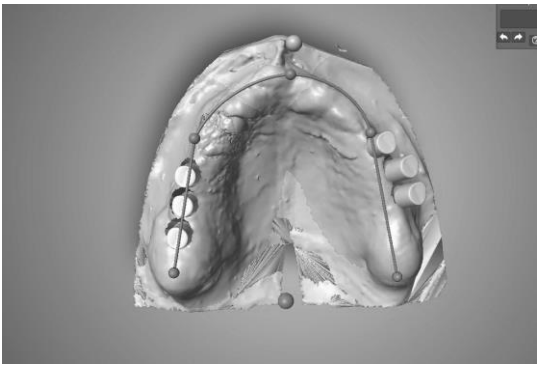

Figure 11. The shape of the dental arch has been planned.

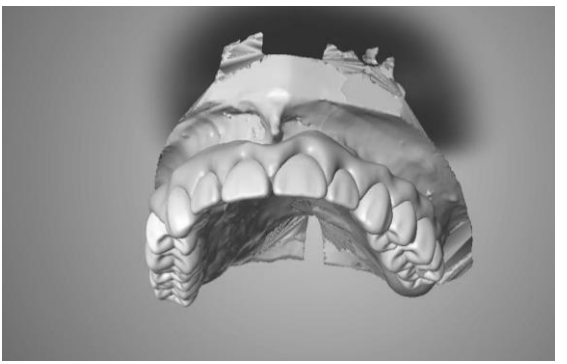

Figure 12. The number and the shape of the teeth have been planned.

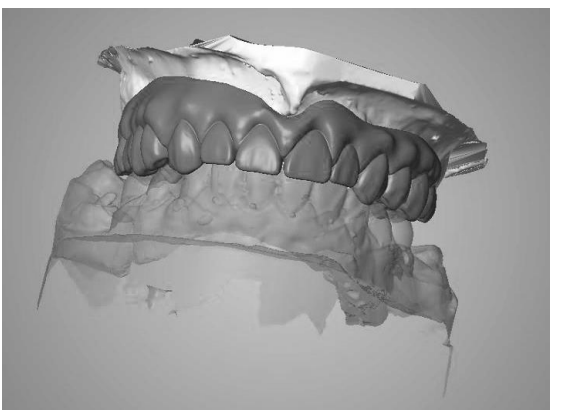

Figure 13. The occlusion has been checked against the opposing dentition.

The designer must also decide whether it is necessary to restore the soft tissue and teeth, or just the teeth, as well as specify the intended size and shape of the teeth. At the same time, how the final prosthesis is going to be attached to the implants must be decided. There are options of screw-retained suprastructures or cemented suprastructures. In the case of screw-retained suprastructures, it is necessary to plan the placement of implants so that they would be parallel to one another. In the case of the bone deficit, it is possible to apply screw-retained suprastructures. The last solution is the use of special mounting screws to allow the angled transmission of forces. Such a solution, however, requires the use of special switches with a larger diameter that cannot always be applied. The decision on fixing the final suprastructure should be taken on the basis of the possibility of implantation in each case at the stage of preparing the surgical guide.

Having checked the proper design of the arch and the shape of the teeth, the designer may proceed to plan the location of the implants in the bone in such a way that they are directly underneath the artificial teeth of the suprastructure (Figures 14 and 15). At the same time, all the implants must be fully engaged in the alveolar bone (Figure 16). Here, it is important to position the implant within a safe distance between the edge of the bone and the vital anatomical structures. This margin should be about 1.5mm, and the distance between the implants should be at least 2mm. Violation of these parameters can take place only with the approval of the implantologist.

The last step during preparation of the surgical guide is to design tunnels for a pilot drill which will help in finding the proper position during the implant bed preparation. The tunnel makes it easy to perform osteotomies for the implants at the pre-planned angles and the required depth. For this purpose, the implant system must be determined before designing the surgical guide.

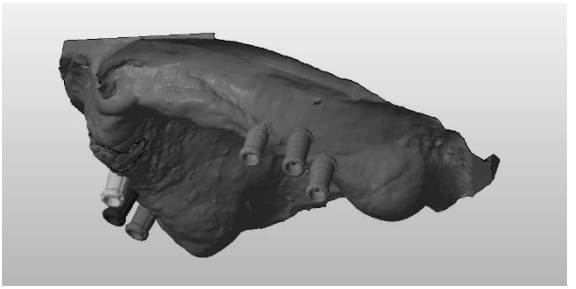

Figure 14. Position of the implants has been planned on the model of the intraoral situation.

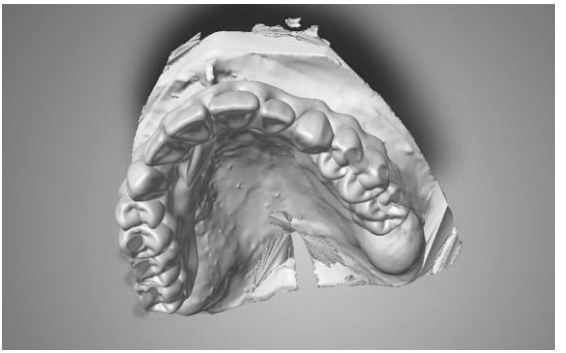

Figure 15. The position of the implants has been checked in accordance to the position of the artificial teeth.

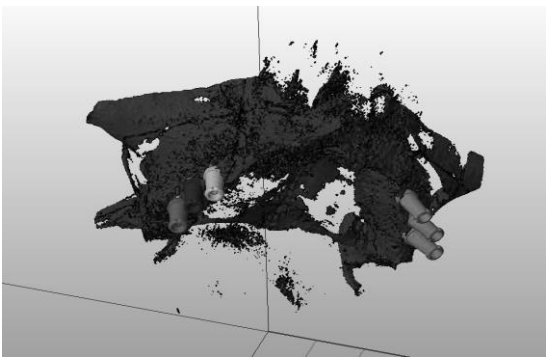

Figure 16. The full engagement of the implants in the bone has been checked on the virtual model created on the basis of CBCT.

The surgical guide can play three roles. The first and most important is that it makes it possible to perform the implantation in very difficult cases. The second role is that it gives the patient an idea about the desired effect of treatment at the beginning of the treatment process. With some adjustments, the surgical guide may also be used as a provisional suprastructure. The tunnels for drills must be covered with acrylic material.

The final task for the designer is to choose the material from which the surgical guide will be made. Generally, two materials are available. The first is poly(methyl methacrylate) (PMMA) (Figures 17 and 18). In this case, the tunnels for the drill must be covered with steel sleeves with the diameter corresponding to the chosen implant system. The other option is to make the surgical guide from zirconia. The second solution allows the manufacturing of the surgical guide as a monoblock, with minimal risk of contamination of the

tunnels for drills with chips produced as a result of accidental touching the walls of the guide with drill. This solution also helps to provide greater accuracy and better shape tiny details on the guide. Zirconia surgical guide after painting and coating with glaze can be used as a temporary bridge. To use the PMMA guide as a bridge, it is necessary to replace the metal sleeves for drills with acryllic plugs.

It is also possible to manufacture the guides from chrome cobalt alloys or titanium alloys (Henriques et al., 2012; Mugoni et al., 2015). In this case, the guide can be used as a temporary or even permanent bridge. However, it is time consuming and more complex than manufacturing the surgical guides from PMMA or zirconia.

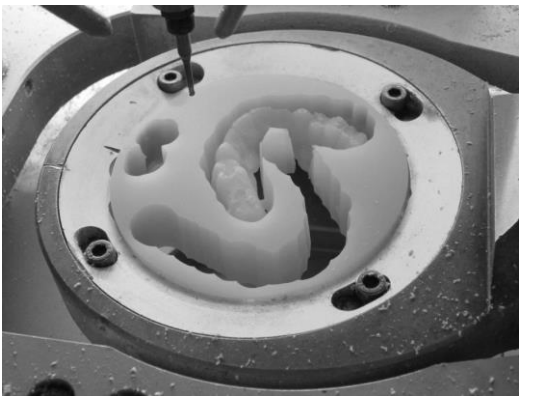

Figure 17. Milling proces of the surgical guide made from PMMA.

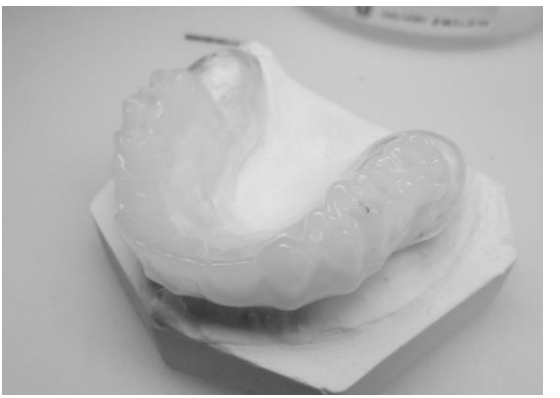

Figure 18. The surgical guide made of PMMA after milling and finishing process.

CONCLUSION

Computer-aided design of surgical guides based on CBCT scans is an efficient method that improves the effectiveness of implant placement procedures. This method reduces the time required for preoperative diagnosis. It also allows the introduction of implants in accordance with the pre-planned position in a predictable manner and in accordance with the requirements of the prosthetic superstructure. With surgical guides, a surgical procedure can be carried out in a quick and minimally invasive manner. The use of surgical guides in most cases helps to avoid flap surgeries and minimize the postoperative morbidity. It also helps increase the safety of the procedure, minimize the risk of postoperative complications, reduce pain after surgery and shorten the recovery time.

REFERENCES

Almog, D. M. Torrado, E., Meitner, S. W. Fabrication of imaging and surgical guides for dental implants. *Journal of Prosthetic Dentistry* 2001, 85: 504-508.

Bornstein, M. M., Halbritter, S., Harnisch, H., Weber, H. P., Buser, D. A retrospective analysis of patients referred for implant placement to a specialty clinic: indications, surgical procedures and early failures. *International Journal of Oral & Maxillofacial Implants*, 2008, 23: 1109-1116.

Cyganek, B., Siebert, J. An Introduction to 3D Computer Vision Techniques and Algorithms, *Wiley* 2009.

De Vos, W., Casselman, J., Swennen, G. R. J. Cone-beam computerized tomography (CBCT) imaging of the oral and maxillofacial region. *International Journal of Oral and Maxillofacial Surgery*, 2009, 38: 609-625.

Dreiseidler, T., Mischkowski, R. A., Neugebauer, J., Ritter, L., Zoller, J. E. Comparison of cone-beam imaging with orthopantomography and computerized tomography for assessment in presurgical implant dentistry. *International Journal of Oral and Maxillofacial Implants*, 2009, 24: 216-225.

Galanis, C. C., Sfantsikopoulos, M. M., Koidis, P. T., Kafantaris, N. M., Mpikos, P.G. Computer methods for automating preoperative dental implant planning, Implant positioning and size assignment. *Computer Methods and Programs in Biomedicine* 2007, 86: 30-38.

Giordano, M., Ausiello, P., Martorelli, M., Sorrentino, R. Reliability of computer designed surgical guides in six implant rehabilitations with two years follow-up. *Journal of Dentistry*2012, 28: 168-177.

Greenberg, A. M. Digital Technologies for dental implant treatment planning and guided surgery. *Oral and Maxillofacial Surgery Clinics of North America*, 2015, 27: 319-340.

Heinemann, F., Hasan, I., Bourauel, C., Biffar, R., Mundt, T. Bone stability around dental implants: Treatment related factors, *Annals of Anatomy*, 2015, 199: 3-8.

Henriques, B., Soares, D., Silva, F.S. Microstructure, hardness, corrosion resistance and porcelain shear bond strength comparison between cast and hot pressed CoCrMo alloy for metal-ceramic dental restorations. *Journal of the Mechanical Behaviour of Biomedical Materials* 2012, 12: 83-92.

Javed, F., Romanos, G. E. The role of primary stability for successful immediate loading of dental implants. *Journal of Dentistry*, 2010, 38: 612-620.

Liaw, K., Delfini, R. H., Abrahams, J. J. Dental implant complications. *Seminars in Ultrasound CT and MRI*, 2015, 36: 427-433.

Malara, P. Treatment of Large Cysts of the Mandible with Autografts of Cancellous Bone from the Tibia. In: A Textbook of Advanced Oral and Maxillofacial Surgery, Ed. MHK Motamedi, Intechopen, Rijeka 2013.

Meloni, S. M., De Riua, G., Lolli, F.M., Pisano, M., Deledda, A., Frisardi, G., Tullio, A. Computer-guided implant surgery, A critical review of treatment concepts. *Journal of Oral and Maxillofacial Surgery, Medicine and Pathology*, 2014, 26: 1-6.

Mora, M.A., Chenin, D.L., Arce, R.M. Software Tools and Surgical Guides in Dental Implant Guided Surgery. *Dental Clinics of North America* 2014, 3: 597-626.

Mugoni, C., Licciulli, A., Diso, D., Siligardi, C. Lanthanum glass infiltrated alumina/alumina composites for dental prosthetic applications. *Ceramics International* 2015, 41: 13090-13099.

Papaspyridakos, P., White, G.S., Lal, K. Flapless CAD/CAM-guided surgery for staged transition from failing dentition to complete arch implant rehabilitation, A 3-year clinical report. *Journal of Prosthetic Dentistry*, 2012, 107: 143-150.

Perez, L. A., Brooks, S. L., Wang, H. L., Eber, R. M. Comparison of linear tomography and direct ridge mapping for the determination of edentulous ridge dimensions in human cadavers. *Oral Surgery Oral Medicine Oral Pathology Oral Radiology and Endodontics*, 2005, 99: 748-754.

Ramos Chrcanovic, B., Albrektsson, T., Wennerberg, A. Tilted versus axially placed dental implants. *Journal of Dentistry* 2015, 43: 149-170.

Rohr, N., Coldea, A., Zitzmann, N. U., Fischer, J. Loading capacity of zirconia implant supported hybrid ceramic crowns. *Dental Materials* (in Print).

Silveira Rodrigues, R. C., Lapria Faria, A. C., Macedo, A. P., Chiarello de Mattos, M. G., Ribeiro R.F. Retention and stress distribution in distal extension removable partial dentures with and without implant association. *Journal of Prosthodontic Research*, 2013, 57: 24-29.

BIOGRAPHICAL SKETCH

Piotr Malara

Institute of Engineering Materials and Biomaterials,
Silesian University of Technology
Konarskiego 18a str., Gliwice, 44-100, Poland
Private Clinic for Oral and Maxillofacial Surgery DENTARIS
Lowiecka 12b str., Ruda Slaska, 41-707, Poland

Education:

1993-1998	Silesian Medical University in POLAND (Dentistry)
2001	PhD in medical sciences, Silesian Medical University thesis: Cationic Equilibrium in Coal-Miners' Teeth from Ruda Slaska
2001-2007	Residency in Department of Oral and Maxillofacial Surgery in Katowice
2007	Specialist Oral and Maxillofacial Surgeon
2008	Doctor of Science, Silesian Medical University
2013-2015	Master's programme in oral implantology Goethe University; Frankfurt am Main (Germany) Master's Thesis: Evaluation of the Proximal Tibia as a Donor Site for Pre-Implantation Procedures with Bone Grafting - a Retrospective Study MSc. in Oral Implantology

Research and Professional Experience:

1. maxillofacial surgery -bone grafting from intra- and extraoral donor sites
2. implantology - surgical and prosthetic procedures,
3. guided bone regeneration,
4. dental materials and biomaterials

Professional Appointments:

1. Associate Professor, Silesian University of Technology
2. Consultant Oral and Maxillofacial Surgeon, Clinic for Oral and Maxillofacial Surgery

Publications:

Malara P., Czech Z., Świderski W.: Influence of the light source and curing parameters on microhardnes of a silorane-based dental composite material. Arch. Metall. Mater. 2016, 61 (3): 985-990.

Chladek G., Basa K., Żmudzki J., *Malara P.*, Nowak A., Kasperski J.: Influence of aging solutions on wear resistance and hardness of selected resin-based dental composites. Acta Bioeng. Biomech. 2016, 18(3), 1-16.

Żmudzki J., *Malara P.*, Chladek G.: Full contoured tooth-implant supported 3-pointic all-ceramic denture during occlusal load transfer in lateral region. Arch. Metall. Mater. 2016, 61 (2A): 843-846.

Dobrzański L., Dobrzańska-Danikiewicz A., *Malara P.*, Gaweł T., Dobrzański L. B., Achtelik-Franczak A.: Fabrication of scaffolds from Ti6Al4V powders using the computer aided laser method. Arch. Metall. Mater. 2015, 60(2A): 1065-1070.

Malara P., Dobrzański L. B.: Computer-aided design and manufacturing of dental surgical guides based on cone beam computed tomography. Arch. Mater. Sci. Eng. 2015, 76 (2): 140-149.

Malara P., Dobrzański L. B., Dobrzańska J.: Computer-aided designing and manufacturing of partial removable dentures. J. Achiev. Mater. Manuf. Eng. 2015, 73(2): 157-164.

Malara P., Czech Z., Świderski W.: Degree of conversion of dental composite materials in relation to different lightcuring parameters. J. Achiev. Mater. Manuf. Eng. 2015, 70 (2): 60-69.

Malara P., Dobrzański L. B.: Designing and manufacturing of implantoprosthetic fixed suprastructures in edentulous patients on the basis of digital impressions. Arch. Mater. Sci. Eng. 2015, 76 (2): 163-171.

Malara P., Gołombek K., Szczęsna M.: Metallographic research of selected alloys used in dentistry. J. Achiev. Mater. Manuf. Eng. 2015, 73(2): 65-71.

Postek-Stefańska L., Stefański T., *Malara P.*, Kloc-Ptaszna A., Górniak M.: The influence of calcium-supplementation to orange juice to reduce enamel erosion within the oral environment. Pol. J. Environ. Stud. 2015, 24(6A): 43-48.

Malara P., Czech Z., Świderski W.: The influence of light curing parameters on wear resistance of selected resin-based dental composites. J. Achiev. Mater. Manuf. Eng. 2014 vol. 64 iss. 2, s. 62-71.

Malara P., Czech Z., Świderski W.: The effect of the curing time and the distance from the light source on hardness of Methacrylate and Silorane resin-based dental composite materials. Arch. Mater. Sci. Eng. 2014 vol. 70 nr 1, s. 28-38.

Świderski W., Czech Z., *Malara P.*: Badania wytrzymałości na ściskanie fotoreaktywnych wypełnień stomatologicznych utwardzanych światłem widzialnym. Przem. Chem. 2014, 93(12): 2214-2217.

Fischer A., *Malara P.*, Wiechuła D.: The Study of Barium Concentration in Deciduous Teeth, Impacted Teeth and Facial Bones of Polish Residents. Biol. Trace. Elem. Res. 2014, 161(1): 32-37.

In: Computed Tomography
Editor: Deborah Carter
ISBN: 978-1-53610-766-1

Chapter 2

ANATOMIC VARIATIONS OF MANDIBULAR CANAL AND MENTAL FORAMEN: AN IN-DEPTH ANALYSIS USING CONE BEAM COMPUTED TOMOGRAPHY

J. Muinelo-Lorenzo, A. Fernández-Alonso and M. M. Suárez-Cunqueiro*

Department of Surgery and Medical Surgical Specialties,
Medicine and Dentistry School, Santiago de Compostela University,
Santiago de Compostela, Spain

ABSTRACT

Cone beam computed tomography (CBCT) is increasingly being used as a diagnostic tool in dentistry, especially in the field of oral surgery. Its high resolution three dimensional images reveal anatomic structures more clearly.

The mandibular canal hosts the inferior alveolar nerve and vessels, which are critical anatomic structures for surgical procedures. The mandibular canal in several cases doesn't appear uniformly as a single canal, it may present various branching patterns. These bifid mandibular canals must be taken into consideration to avoid clinical complications.

* Corresponding author email: mariamercedes.suarez@usc.es

A number of classifications have been developed on anatomic and panoramic radiography surveys. However, the true incidence of bifid mandibular canal is underestimated on panoramic images due to the two-dimensional nature of panoramic radiography. The overlap of anatomic structures such as soft palate, airway, milohioid groove, and submandibular fossa may interfere with the visualization of these neurovascular bifid canals. Also, the buccolingual type of canals may be missed on panoramic images, but can be easily identified on CBCT images. CBCT allows for better depiction of small vascular canals regardless trabecular pattern.

The mental foramen is a bilateral opening in the anterolateral region of the mandible through which the mental nerve emerges. The mental nerve represents one of the terminal branches of the inferior alveolar nerve, and supplies the lower lip, cheeks, chin, and the vestibular gingiva of mandibular incisors. Although the mental foramen is one of the most important neurovascular landmarks in the anterior mandible, its identification is not always possible using panoramic radiographs. The visualization on panoramic images is influenced by mental foramen size, trabecular pattern, mental foramen emergence, and patient's age. However, a CBCT image improves mental foramen depiction, offering advantages over two-dimensional radiological images.

The mental foramen usually remains as a single structure, however in some cases, the mental nerve branches before exiting the mandible originating small foramina in the area surrounding the mental foramen known as accessory mental foramina. This anatomic landmark is not rare, it has been reported a rate of occurrence up to 20% in CBCT studies, and its position is crucial for surgical procedures involving this region, such as surgical rehabilitation after mandibular trauma, bone harvesting from the chin, root resection of mandibular premolars, and particularly for dental implants placement.

An accessory mental foramen located above the mental foramen directly affects the treatment planning using dental implants, since their position may limit surgical procedures. This was found in up to 4% of the population, which means it is necessary to consider these accessory foramina to the main mental foramen. An accessory mental foramen located closely to the apex of the lower teeth can simulate false periapical pathology. By using the CBCT, continuity with the mandibular canal can be easily identified which avoids unnecessary damage. Therefore, a CBCT image examination may be a very important aid before surgical treatments in the mandible.

Keywords: mandibular nerve, bifid mandibular canals, accessory mental foramen, mandibular anatomy, CBCT imaging, surgical planning

INTRODUCTION

Cone beam computed tomography (CBCT) is increasingly being used as a diagnostic tool in dentistry, especially in the field of oral surgery. Its high resolution three- dimensional images reveal anatomic structures more clearly. Oral and maxillofacial two-dimensional images have several superimpositions. The overlap of anatomic structures such as soft palate, airway, mylohyoid groove, and submandibular fossa may interfere with the visualization of these neurovascular canals, so that fine structures can be identified to a limit extent. Other mandibular structures such as the presence of large mandibular tori, difficult the depiction of the mandibular canal by attenuating the cortical contrast of the mandibular canal [1]. During surgical treatment, the position of neurovascular structures is based on the surgeon´s capability for interpretation these images and the limits the recognition of individual anatomical variations. Oral surgeons are acquainted with normal neurovascular landmarks, however anatomical variation must be considered. These individual deviations are often present and may hamper surgical procedures.

CBCT technology provides multiplanar reconstructions which allow identifying variations in anatomic structures better than 2D images. Size is an important factor for depiction of anatomic landmarks, and the volumetric CBCT data provides valuable sectional images which are essential in depicting fine anatomic landmarks. Also, CBCT scans may be analyzed by means of modern computed tomography software, then it may be possible a detailed dynamic study prior to surgeries.

MANDIBULAR CANAL

Anatomy

The mandibular canal hosts the inferior alveolar nerve and vessels, which are critical structures for surgical procedures. The inferior alveolar nerve is the largest branch of the mandibular nerve. It runs through the infratemporal fossa before entering into the lower jaw through mandibular foramen. Then, it courses together with the inferior alveolar artery into the mandibular canal constituting the inferior neurovascular bundle. The inferior alveolar artery runs in a superior and lingual position inside the mandibular canal. It is exclusively situated bucally in the mandibular ramus. The inferior alveolar nerve is located

anterior and medial at the mandibular foramen in 60% of cases. Less often it is situated laterally (20%), posteriorly (10%) or, independently (10%) from the artery [2]. The mandibular canal gives off the following terminal branches: the mental nerve, the larger branch that emerges from the mental foramen, and the incisive nerve that continues inside the mandible to innervate the anterior teeth and gingiva. Anatomic dissections have revealed branches from the inferior alveolar nerve, arising high in the infratemporal fossae, and passing through one or various small foramina in the retromolar region supplying the mandibular molars, area denominated retromolar foramina. These foramina may also be the exit of mandibular branching originated in the mandibular ramus. The fibers passing through the retromolar foramen innervate part of the temporal and buccinators muscles, the retromolar trigone, the buccal mucosa, the buccal gingiva of molars and premolars, and the pulp of the third molar. Vessels from inferior alveolar artery have been identified coursing the retromolar foramen to get anastomosis with branches of the buccal and facial arteries [3, 4].

Other anatomic important variations for surgeries are the presence of an anterior loop, partial obliterations of the canal, and the presence of accessory mental foramina. The potential presence of these variations must be taken into consideration to avoid clinical complications.

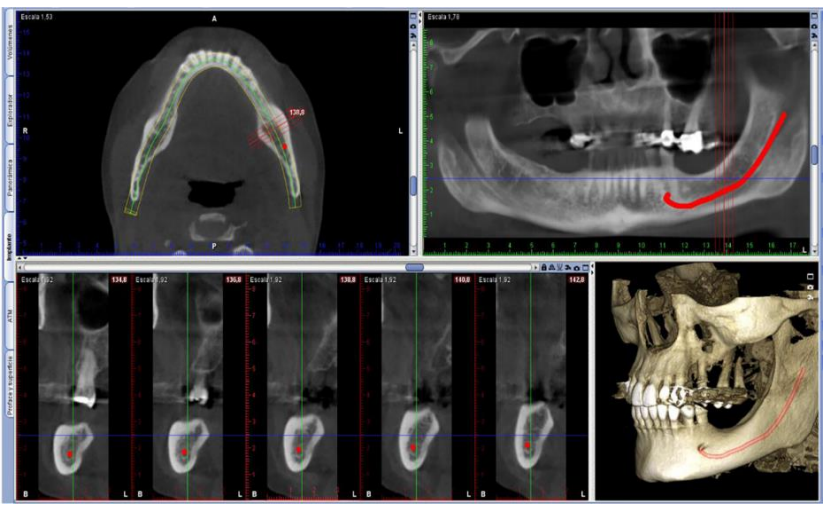

Figure 1. CBCT reconstructions of a mandible to identify the three-dimensional course of the mandibular canal. The mandibular canal is highlighted in cross-sectional and panoramic views (Planmeca Romexis Software®).

Mandibular Canal on CBCT

Since its entering from the internal surface of the mandible, the mandibular canal appears as radiolucent duct which may courses downwards progressively, go ahead and down more sharply, or in a catenary curve form (Figure 1). It generally moves forward close to the mandibular lingual cortical surface. However, it may courses next to the buccal cortex in wide mandibles. This was observed in 6% of mandibles. The diameter of the canal ranges from 2.6 mm to 4.3 mm [5-9].

The mandibular canal is not identified in all panoramic radiographies. It has been reported that it is only recognized in 63% of cases, with a clear visibility in only 25% [10, 11]. The presence and position of the mandibular canal by panoramic radiographs can be considered presumptive, and their presence occasionally cannot be asserted firmly. The visibility of the mandibular canal on panoramic radiography is influenced by the degree of corticalization of the canal. The canal is better identified in the mental foramen region, and in the posterior mandibular region, next to the third mandibular molar, because the canal walls become denser in those areas. The mandibular canal is also better visualized in younger patients, and those presenting high bone densities. The CBCT is an important tool for proper identification of the mandibular canal in those areas where the canal has a poor corticalization, or showing low cancellous bone density.

Bifid Mandibular Canals on CBCT

The mandibular canal does not often appear uniformly as a single canal, due to an incomplete fusion during the embryologic development, then it may present various branching patterns. The mandibular canal may often give rise to medial, lateral, inferior and superior branches. Oliver [12] describes the mandibular canal as a single canal in only 60% of the mandibles, and with various branching patterns through its intraosseous course in the others. The bifid mandibular canal constitutes a relatively common anatomic variation in the population. CBCT studies provide rates up to 65%. However, the panoramic radiography reveals a very low prevalence of bifid mandibular canals, ranging from 0.08% to 16.8% (Table 1). The true incidence of bifid mandibular canal is underestimated on panoramic images due to the two-dimensional nature of panoramic radiography. Also, it has been reported that only 45% of bifid canals present a complete corticalization, thereby hampering

its depiction on panoramic radiographs [13]. Compared to panoramic radiography, CBCT allows for better depiction of small vascular canals regardless trabecular pattern.

Table 1. Review of the prevalence of the bifid mandibular canals, comparison between panoramic radiography and CBCT. The prevalence is higher in CBCT studies (n/d: no data analysis, no diff.: no statistical significant differences)

Bifid mandibular canals (BMC) on panoramic radiography (PAN)				
	PAN (N)	**BMC prevalence (%)**	**Gender**	**Age**
Nortjé [14,15] (1977–1978) (South Africa)	3612	0.9%	No diff.	No diff.
Durst and Snow[16] (1980) (USA)	1024	8.3%	n/d	n/d
Grover and Lorton [17] (1983) (USA)	5000	0.08%	4 male / 0 females	n/d
Langlais [18] (1985) (USA)	6000	0.9%	No diff.	n/d 0.01%(10s);0.21%(20s); 0.18%(30s); 0.11%(40s);0.08%(50s); 0.01%(50s)
Zografos [19] (1990) (Greek)	700	0.4%	No diff.	n/d
Sanchis [20] (2003) (Spain	2012	0.3%	>freq. women	No diff.
Bogdan[21] (2006) (Hungary)	1000	0.2%	No diff.	n/d
Kim [22] (2011) (South Korea)	1000	0.03%	n/d	n/d
Kashabah [23] (2013) (Syria)	2400	0.9%	No diff.	n/d
Neves [24] (2013) (Brazil)	127	7.4%	n/d	n/d
Kuczynski [25] (2014) (Brazil)	3024	1.9%	n/d	n/d
Muinelo-Lorenzo [26] (2014) (Spain)	225	16.8%	No diff.	No diff.
Kalantar [27] (2015) (Iran)	5000	1.2%	No diff.	No diff.

Bifid mandibular canals on CBCT				
	CBCT (N)	**BMC prevalence (%)**	**Gender**	**Age**
Yi [29] (2015) (China)	216	18%	n/d	n/d
Shen [13] (2014) (Taiwan)	308	41.2%	n/d	n/d
Rashsuren [9] (2014) (Korea)	500	22.6%	No diff.	No diff. 6.6%(20s);11.2%(30s); 9.1%(40s);14.2%(50s);14.6%(60s)
Leite [30] (2014) (Brazil)	250	12%	n/d	n/d
Muinelo-Lorenzo [26] (2014) (Spain)	225	36.8%	>freq. males	No diff. 39.3%(<50s), 33.6%(≥50s)
Kang [31] (2014) (Korea)	1933	10.2%	No diff.	No diff.
Neves [24] (2014) (Brasil)	127	9.8%	n/d	n/d
Orhan [32] (2013) (Turkey) (children)	63	42.8%	n/d	No diff.
Fu [8] (2012) (Taiwan) (TC)	173	30.6%	>freq. males	n/d
de-Oliveira [33] (2012) (Belgium)	100	19%	No diff.	No diff.
Orhan [34] (2011) (Turkey)	242	66.5%	No diff.	n/d
Kuribayashi [35] (2010) (Japan)	310	15.6%	No diff.	n/d
Naitoh [36] (2009) (Japan)	122	64.8%	No diff.	n/d

A number of bifid mandibular canals classifications have been developed on anatomic and panoramic radiography studies. The most widely used classification on CBCT has been conducted by Naitoh [36]. Four types of bifid canals were determined (Figures 2-3):

- Retromolar canal. The canal branches from the mandibular canal in the mandibular ramus, and courses upwards reaching the retromolar area. Retromolar area consists of a triangular depression, delimited medially by the temporal crest, and laterally by the anterior border of the mandibular ramus. The opening of the retromolar canal is denominated retromolar foramen.

- Anterior canal. It originates from the upper surface of the canal, and may confluence or not with the canal.
- Dental canal. The bifurcation runs to the dental root of the third or second molar
- Buccolingual canal. The bifid canal exits from the main canal in a lingual or buccal direction.

The diameter of the bifid canals on cross-sectional slices varies from 1 to 2.2 mm, approximately, and they reach 1 to 1.5 cm of length on sagittal slices [8, 9, 13, 31, 33, 34]. About 49% to 65% of bifid canals exceed half the diameter of the mandibular canal. Anterior and retromolar are the longest types of bifid canals. The confluence of the bifid canal and the mandibular canal originates an upper and a lower angle. The upper angle ranges, on average, from 120º to 150º, depending on the type of bifurcation. Because of their shape, anterior canals and retromolar canals have the highest and the lowest upper angle, respectively. The inferior angle is on average between 30º and 40º, and retromolar and anterior canals present the highest and the lowest inferior angles, respectively [13, 26, 34]. The most predominant types of bifurcation are retromolar and anterior canals, both accounts for 75% of bifurcations.

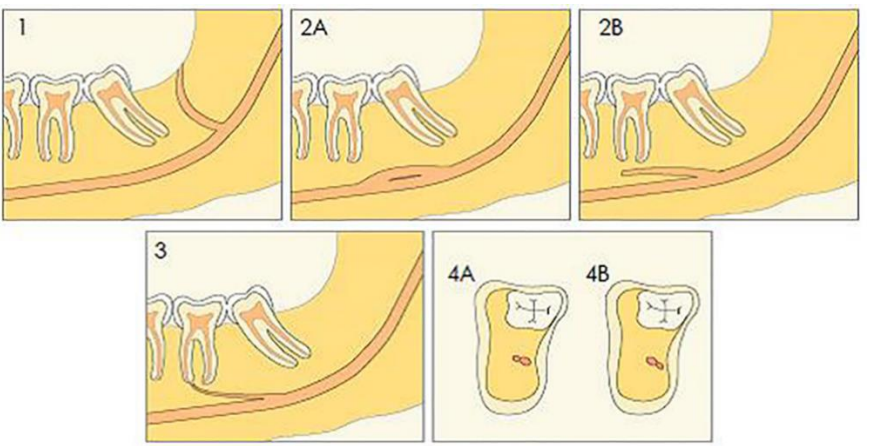

Figure 2. Naitoh's classification of bifid mandibular canals: 1 Retromolar canal. 2A Anterior canal with confluence. 2B Anterior canal without confluence. 3 Dental canal. 4A,B Buccolingual canals.

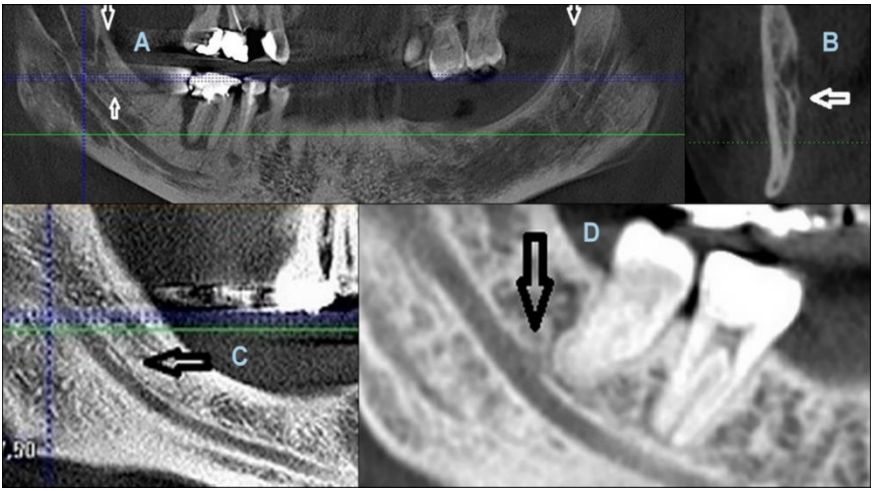

Figure 3. Types of bifid mandibular canals: A Panoramic reconstruction showing a retromolar canal and an anterior canal arising from the retromolar canal in the right side. The left side also presents a retromolar canal. B Lingual canal on a cross-sectional image from the mandibular ramus. C Sagittal reconstruction of a hemimandible with anterior canal showing confluence with the mandibular canal. D Sagittal reconstruction of a hemimandible with a dental canal to the molar apex (i-CAT Vision software®).

The retromolar foramen is a structure that has been recently considered since it constitutes the entry of certain neurovascular structures in the mandible, apart from being the exit of bifid retromolar canals. It is commonly unilateral, with a size ranging from 1 to 2 mm. The prevalence of retromolar foramina on CBCT has been reported to be between 1.7% and 75.4% [35, 37].

Clinical Implications of Bifid Mandibular Canals and Retromolar Foramen

Performing surgeries in the mandible implies to take into account the possible complications of the bifid canal lesion. The CBCT is a useful tool before any surgical procedures such as dental implant placement. The bifid canals may be localized in potential sites for implants placement, thus it could be injured during the drilling procedure. The implant position may be modified to avoid sensory disturbances or profuse bleedings. Also, it may increase the risk of peri-implant formation of fibrous tissue causing inadequate outcome in osseo-integration. The presence of retromolar canals must be considered

before bone harvesting from the mandibular ramus for augmentation procedures, and before the removal of third molar teeth. The retromolar area represents a donor region for bone harvesting, and the presence of bifid retromolar canals could difficult it. The retromolar foramen is pierced by nervous and vascular content which may be injured during the flap reflection. It is necessary to identify its course to avoid vascular and neural injuries. The presence of bifid dental canals also presents clinical importance during routinary procedures such as dental extractions and root canal treatment [9, 36].

CBCT analysis for mandibular fractures is very helpful for proper alignment of the mandibular canal. Also, it may reveal bifurcations of the mandibular canal. The presence of these bifurcations further complicated the proper positioning of the fragments. A thorough volumetric analysis must be conducted to identify possible bifurcations to avoid entrapment or impingement of the neurovascular canals during the fracture healing.

In daily clinical practice, there are cases in which adequate anesthesia is not achieved using an inferior alveolar blockage. The presence of bifid mandibular canals, especially in the retromolar region, may be the reason for failing. The presence of a bifurcation should be considered when anaesthesia is reached in the ipsilateral lip and mental area, but no dental anaesthesia is achieved after inferior alveolar blockage. The CBCT allows identifying patients with bifurcations more clearly than panoramic radiography, helping us to perform alternative anaesthetic procedures, such as Akinosi and Gow Gates techniques. The presence of a retromolar canal may also be the cause of inadequate anesthesia in the retromolar and buccal mucosae.

Patients with removable dentures can present important bone resorption in the retromolar area. In some cases, the prostheses may produce pain due to the pressure exerted on the neurovascular bundle, when a retromolar canal emerges through the retromolar foramen. In these cases, identify this variant requires prosthesis design modification.

MENTAL FORAMEN

Anatomy

The mental foramen is a bilateral opening in the anterolateral region of the mandible through which the mental nerve emerges. The mental nerve represents one of the terminal branches of the inferior alveolar nerve, and

supplies the lower lip, cheeks, chin, and the vestibular gingiva of mandibular incisors. The mental foramen usually remains as a single structure, however, in some cases, the mental nerve bifurcates, before exiting the mandible, originating small foramina in the area surrounding the mental foramen known as accessory mental foramina [38].

Mental Foramen on CBCT

The mental foramen is one of the most important neurovascular landmarks in the anterior mandible, but its identification is not always possible using panoramic radiographs. The visualization on panoramic images is influenced by mental foramen size, trabecular pattern, mental foramen emergence, and patient's age. However, CBCT allows a depiction of mental foramen in 100% of cases [39, 40] (Figure 4).

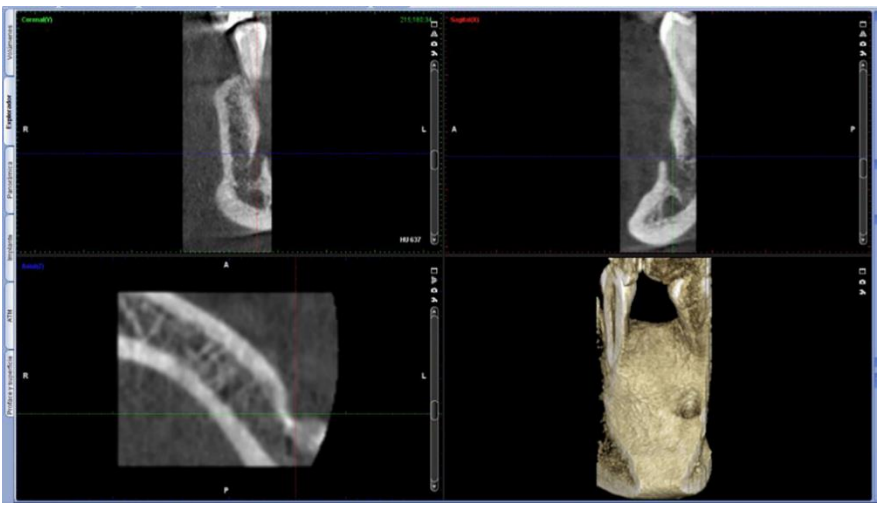

Figure 4. Sectional CBCT showing the left mental foramen (Planmeca Romexis Software®).

The mental foramen is commonly oval and located midway between alveolar crest and the lower mandibular border. The mental foramen has on average a diameter ranging from 2.3 to 3 mm, a height ranging from 2.6 to 3.7 mm, and width from 3.2 to 4.1 mm [32, 41-44]. It is generally located coronally to the inferior alveolar canal, and close to the apex of the second inferior premolar, or between the two inferior premolars. Its position is

superior to the premolar apexes between 25% and 38% of patients. Mental nerve and foramen may vary in their location, emerging direction, morphology, size, and number. Mental foramen is located approximately 12-15 mm from the mandibular inferior border, and on average 28 mm lateral to the midline [42, 45]. Its position may range from 22 to 31 mm to the midline, and between 9 and 15 mm to inferior border. Variations in mental foramen characteristics and position with respect to the dentition are determined by gender, age, periodontal disease and bone loss after tooth extraction.

Accessory Mental Foramen on CBCT

The accessory mental foramen is usually single and unilateral but it was reported cases with up to four accessory foramina (Figure 5). This anatomic landmark is not rare, it has been reported a rate of occurrence up to 14% in CBCT studies (Table 2). It was described passing through the cortical mandibular surface the presence of other different small foramina called buccal or nutritional foramina [46]. They are smaller in size and do not communicate with the mandibular inferior alveolar nerve. They are a passage for the lower lip, submental, and facial nerves deep into the cancellous bone.

Table 2. Review of prevalence of the accessory mental foramina. Comparison between panoramic radiography and CBCT. The prevalence of accessory mental foramina is markedly higher in CBCT studies (n/d: no data analysis, no diff.: no statistical significant differences)

Accessory mental foramina (AMF) on panoramic radiography (PAN)	PANs N (N hem.)	AMF prevalence % (% hem.)	Gender	Age
Muinelo-Lorenzo [47] (2015) (Spain)	344 (688)	6.3% (3.1hem.)	No diff.	No diff.
Capote [48] (2015) (Brazil)	500 (1000)	(3% hem.)	n/d	n/d
Kqiku [49] (2013) (Kosovo)	500	<1%	n/d	n/d
Neves [24] (2013) (Brazil)	127 (254)	(1.2% hem.)	n/d	n/d
Naitoh [50] (2011) (Japan)	365	≈3.7%	n/d	n/d
Al-Khateeb [51] (2007) (Jordan)	860 (1720)	10%	n/d	n/d

AMF on CBCT	CBCTs N	AMF prevalence %	Gender	Age
Muinelo-Lorenzo [47] (2015) (Spain)	344	13%	No diff.	No diff.
Iwanaga [52] (2015) (Japan)	63	14.3%	n/d	n/d
Carruth [41] (2015) (USA)	106	6.6%	n/d	n/d
Khojastepour [39] (2015) (Iran)	156	5.1%	No diff.	No diff.
Leite [30] (2014) (Brazil)	250	3.2%	No diff.	No diff.
Cantekin [53] (2014) (Turkey)	275	6.5% (children)	No diff.	n/d
Santos [54] (2013) (Brazil)	58	5.1%	n/d	n/d
Neves [24] (2013) (Brazil)	127	7.4%	n/d	n/d
Göregen [55] (2013) (Turkey)	315	6.3%	No diff.	n/d
Orhan [32] (2013) (Turkey)	63	6.3% (children)	n/d	n/d
Sisman [56] (2012) (TC) (Turkey)	504	2%*	No diff.	No diff.
Kalender [42] (2012) (Turkey)	193	6.5%	No diff.	n/d
Imada [44] (2012) (Brasil)	100	3%	n/d	n/d
de Oliveira-Santos [33] (2012) (Belgium)	100	14%	n/d	n/d
Oliveira Santos [57] (2011) (Belgium)	285	9.4%	No diff.	No diff.
Naitoh [50] (2011) (Japan)	365	7.7%	n/d	n/d
Naitoh [58] (2010) (Japan)	28	7.1%	n/d	n/d
Haktanir [59] (2010) (Turkey) CT	285	9.4%	No diff.	No diff.
Naitoh [36] (2009) (Japan)	157	7%	No diff.	No diff.
Katakami [43] (2008) (Japan)	150	10.7%	n/d	n/d

Clinical Implications of Mental Foramen and Accessory Mental Foramina

The position of the mental foramen and the accessory mental foramina are crucial for surgical procedures involving this region, such as surgical rehabilitation after mandibular trauma, bone harvesting from the chin, root resection of mandibular premolars, and particularly for dental implants placement (Figures 6-8).

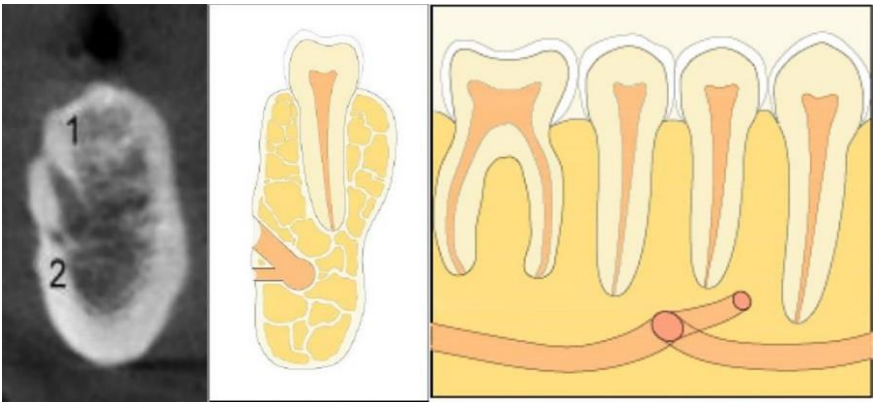

Figure 5. Cross-sectional CBCT image representing the mental foramen (1), and an accessory mental foramen (2). Cross-sectional and sagittal drawings of a mandible with an accessory mental foramen.

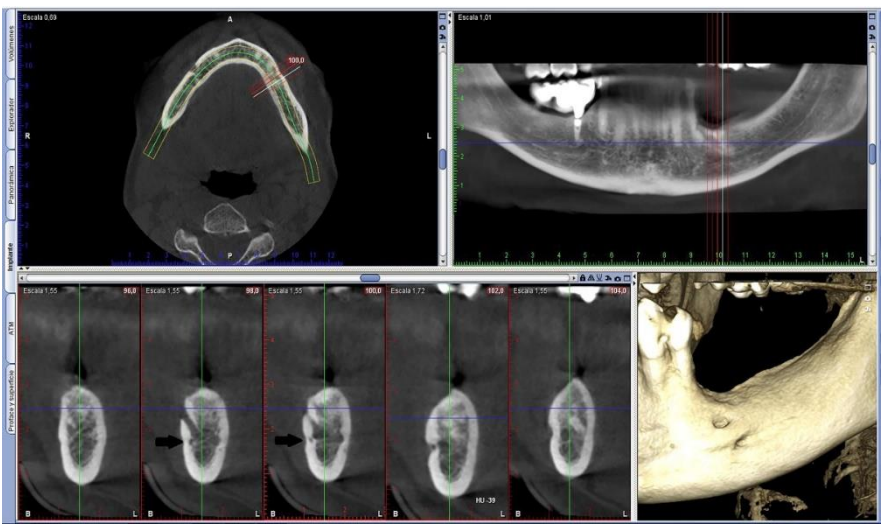

Figure 6. CBCT reconstructions of a 65-year-old male patient with an accessory mental foramen in the left hemimandible. The accessory mental foramen is placed posteriorly and inferiorly to the mental foramen (Planmeca Romexis Software®).

An accessory mental foramen located above the mental foramen directly affects the treatment planning using dental implants, since their position may limit surgical procedures (Figure 9). This was found in up to 4% of the population, which means it is necessary to consider these accessory foramina to the main mental foramen [47, 57]. An accessory mental foramen located

closely to the apex of the lower teeth can simulate false periapical pathology. By using CBCT, continuity with the mandibular canal can be easily identified avoiding diagnostic mistakes. Therefore, a CBCT image examination may be a very important aid before surgical treatments in the mandible.

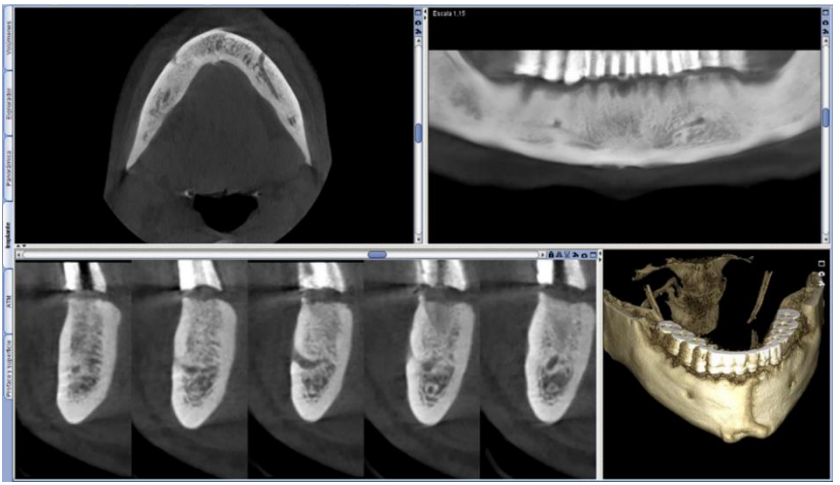

Figure 7. Multiplanar reconstructions of mandible to view the mental foramen three-dimensional position before implant placement. There is no accessory mental foramen. A radiopaque scanning template allows a more precise location of the mental foramina (Planmeca Romexis Software®).

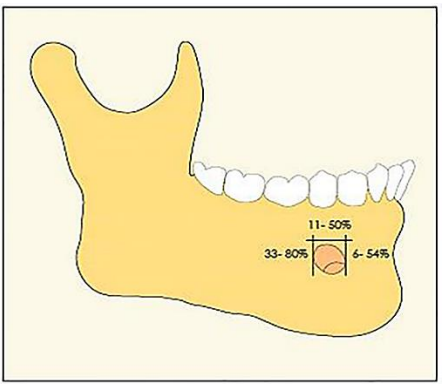

Figure 8. Distribution of the position of the accessory mental foramina with respect to the mental foramen. CBCT studies have observed that between 11% and 50% of the accessory mental foramina are located above the mental foramen apex (i-CAT Vision software®).

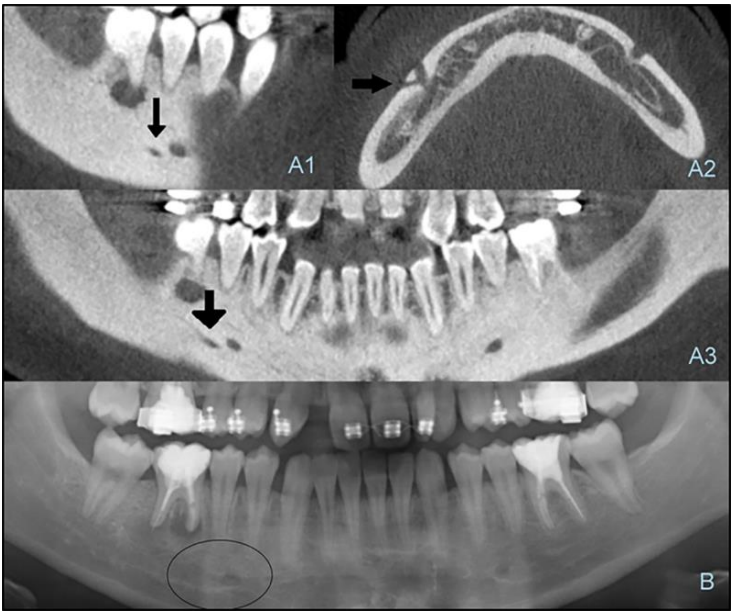

Figure 9. A1, A2, A3 Sagittal, axial and panoramic reconstructions of a 31 years old male patient with an accessory mental foramina located posteriorly with respect to the right mental foramen (i-CAT Vision® software). B The accessory mental foramina cannot be identified with panoramic radiography (Sidexis® neXt Generation).

REFERENCES

[1] Juodzbalys, G, Wang, H. L., (2010). Identification of the mandibular vital structures: practical clinical applications of anatomy and radiological examination methods. *J Oral Maxillofac Res.* 1, e1.

[2] Roda, R. S., Blanton, P.L., (1994). The anatomy of local anesthesia. *Quintessence Int.* 25, 27-38.

[3] Kodera, H., Hashimoto, I., (1995). [A case of mandibular retromolar canal: elements of nerves and arteries in this canal]. *Kaibogaku Zasshi.* 70, 23-30.

[4] Schejtman, R., Devoto, F. C., Arias, N. H., (1967). The origin and distribution of the elements of the human mandibular retromolar canal. *Arch Oral Biol.* 12, 1261-1268.

[5] Anderson, L. C., Kosinski, T. F., Mentag, P. J., (1991). A review of the intraosseous course of the nerves of the mandible. *J Oral Implantol.* 17, 394-403.

[6] Gowgiel, J. M., (1992). The position and course of the mandibular canal. *J Oral Implantol.* 18, 383-385.

[7] Tamas, F., (1987). Position of the mandibular canal. *Int J Oral Maxillofac Surg.* 16, 65-69.

[8] Fu, E., Peng, M., Chiang, C. Y., Tu, H. P., Lin, Y. S., Shen, E. C., (2014). Bifid mandibular canals and the factors associated with their presence: a medical computed tomography evaluation in a Taiwanese population. *Clin Oral Implants Res.* 25, e64-67.

[9] Rashsuren, O., Choi, J. W., Han, W. J., Kim, E. K., (2014) Assessment of bifid and trifid mandibular canals using cone-beam computed tomography. *Imaging Sci Dent.* 44, 229-236.

[10] Klinge, B., Petersson, A., Maly, P., (1989). Location of the mandibular canal: comparison of macroscopic findings, conventional radiography, and computed tomography. *Int J Oral Maxillofac Implants.* 4, 327-332.

[11] Lindh, C., Petersson, A., Klinge, B., (1992). Visualisation of the mandibular canal by different radiographic techniques. *Clin Oral Implants Res.* 3, 90-97.

[12] Oliver, E., (1927). The inferior dental canal and its nerve in the adult. *Ann Anat Pathol.* 4, 975-987.

[13] Shen, E. C., Fu, E., Fu, M. M., Peng, M., (2014). Configuration and corticalization of the mandibular bifid canal in a Taiwanese adult population: a computed tomography study. *Int J Oral Maxillofac Implants.* 29, 893-897.

[14] Nortje, C. J., Farman, A. G., Grotepass, F. W., (1977). Variations in the normal anatomy of the inferior dental (mandibular) canal: a retrospective study of panoramic radiographs from 3612 routine dental patients. *Br J Oral Surg.* 15, 55-63.

[15] Nortje, C. J., Farman, A. G., de V Joubert, J. J., (1977). The radiographic appearance of the inferior dental canal: an additional variation. *Br J Oral Surg.* 15, 171-172.

[16] Durst, J. H., Snow, J. E., (1980). Multiple mandibular canals: oddities or fairly common anomalies? *Oral Surg Oral Med Oral Pathol.* 49, 272-273.

[17] Grover, P. S., Lorton, L., (1983). Bifid mandibular nerve as a possible cause of inadequate anesthesia in the mandible. *J Oral Maxillofac Surg.* 41, 177-179.

[18] Langlais, R. P., Broadus, R., Glass, B. J., (1985). Bifid mandibular canals in panoramic radiographs. *J Am Dent Assoc.* 110, 923-926.

[19] Zografos, J., Mutzuri, A., (1989). [Incidence of double mental foramen in a sample of Greek population]. *Odontostomatol Proodos.* 43, 521-523.

[20] Sanchis, J. M., Penarrocha, M., Soler, F., (2003). Bifid mandibular canal. *J Oral Maxillofac Surg.* 61, 422-424.

[21] Bogdan, S., Pataky, L., Barabas, J., Nemeth, Z., Husza, T., Szabo, G., (2006). Atypical courses of the mandibular canal: comparative examination of dry mandibles and x-rays. *J Craniofac Surg*. 17, 487-491.

[22] Kim, S. T., Hu, K. S., Song, W. C., Kang, M. K., Park, H. D., Kim, H. J., (2009). Location of the mandibular canal and the topography of its neurovascular structures. *J Craniofac Surg*. 20, 936-939.

[23] Kasabah, S., Modellel, Y., (2014). Classification of bifid mandibular canals in the Syrian population using panoramic radiographs. *East Mediterr Health J.* 19, S178-183.

[24] Neves, F. S., Nascimento, M. C., Oliveira, M. L., Almeida, S. M., Boscolo, F. N., (2014). Comparative analysis of mandibular anatomical variations between panoramic radiography and cone beam computed tomography. *Oral Maxillofac Surg.* 18, 419-424.

[25] Kuczynski, A., Kucharski, W., Franco, A., Westphalen, F. H., de Lima, A. A., Fernandes, A., (2014). Prevalence of bifid mandibular canals in panoramic radiographs: a maxillofacial surgical scope. *Surg Radiol Anat*. 36, 847-850.

[26] Muinelo-Lorenzo, J., Suarez-Quintanilla, J. A., Fernandez-Alonso, A., Marsillas-Rascado, S., Suarez-Cunqueiro, M. M., (2014). Descriptive study of the bifid mandibular canals and retromolar foramina: cone beam CT vs panoramic radiography. *Dentomaxillofac Radiol.* 43, 20140090.

[27] Kalantar Motamedi, M.H., Navi, F., Sarabi, N., (2015). Bifid mandibular canals: prevalence and implications. *J Oral Maxillofac Surg.* 73, 387-390.

[28] Villaca-Carvalho, M. F., Manhaes, L. R. Jr., de Moraes, M. E., Lopes, S.L., (2016). Prevalence of bifid mandibular canals by cone beam computed tomography. *Oral Maxillofac Surg*. 20, 289-294.

[29] Yi, G., Qiaohong, Z., Xiaoqian, H., (2015). [Analysis of bifid mandibular canal via cone beam computed tomography]. *Hua Xi Kou Qiang Yi Xue Za Zhi.* 33, 158-160.

[30] Leite, G. M., Lana, J. P., de Carvalho Machado, V., Manzi, F. R., Souza, P. E., Horta, M.C., (2014). Anatomic variations and lesions of the mandibular canal detected by cone beam computed tomography. *Surg Radiol Anat.* 36, 795-804.

[31] Kang, J. H., Lee, K. S., Oh, M. G., Choi, H. Y., Lee, S. R., Oh, S. H., Choi, Y. J., Kim, G.T., Choi, Y. S., Hwang, E. H., (2014). The incidence and configuration of the bifid mandibular canal in Koreans by using cone-beam computed tomography. *Imaging Sci Dent,* 44, 53-60.

[32] Orhan, A. I., Orhan, K., Aksoy, S., Ozgul, O., Horasan, S., Arslan, A., Kocyigit, D., (2013). Evaluation of perimandibular neurovascularization with accessory mental foramina using cone-beam computed tomography in children. *J Craniofac Surg.* 24, e365-369.

[33] de Oliveira-Santos, C., Souza, P. H, de Azambuja Berti-Couto, S., Stinkens, L., Moyaert, K., Rubira-Bullen, IR., Jacobs, R., (2012). Assessment of variations of the mandibular canal through cone beam computed tomography. *Clin Oral Investig.* 16, 387-393.

[34] Orhan, K., Aksoy, S., Bilecenoglu, B., Sakul, B. U., Paksoy, C. S., (2011). Evaluation of bifid mandibular canals with cone-beam computed tomography in a Turkish adult population: a retrospective study. *Surg Radiol Anat.* 33, 501-507.

[35] Kuribayashi, A., Watanabe, H., Imaizumi, A., Tantanapornkul, W., Katakami, K., Kurabayashi, T., (2010) Bifid mandibular canals: cone beam computed tomography evaluation. *Dentomaxillofac Radiol.* 39, 235-239.

[36] Naitoh, M., Nakahara, K., Hiraiwa, Y., Aimiya, H., Gotoh, K., Ariji, E., (2009). Observation of buccal foramen in mandibular body using cone-beam computed tomography. *Okajimas Folia Anat Jpn.* 86, 25-29.

[37] Patil, S., Matsuda, Y., Nakajima, K., Araki, K., Okano, T., (2013). Retromolar canals as observed on cone-beam computed tomography: their incidence, course, and characteristics. *Oral Surg Oral Med Oral Pathol Oral Radiol*. 115, 692-699.

[38] Toh, H., Kodama, J., Yanagisako, M., Ohmori, T., (1992). Anatomical study of the accessory mental foramen and the distribution of its nerve. *Okajimas Folia Anat Jpn.* 69, 85-88.

[39] Khojastepour, L., Mirbeigi, S., Mirhadi, S., Safaee, A., (2015) Location of Mental Foramen in a Selected Iranian Population: A CBCT Assessment. *Iran Endod J.* 10, 117-121.

[40] Parnia, F., Moslehifard, E., Hafezeqoran, A., Mahboub, F., Mojaver-Kahnamoui, H., (2012). Characteristics of anatomical landmarks in the mandibular interforaminal region: a cone-beam computed tomography study. *Med Oral Patol Oral Cir Bucal.* 17, e420-425.

[41] Carruth, P., He, J., Benson, B.W., Schneiderman, E. D., (2015). Analysis of the Size and Position of the Mental Foramen Using the CS 9000 Cone-beam Computed Tomographic Unit. *J Endod.* 41, 1032-1036.

[42] Kalender, A., Orhan, K., Aksoy, U., (2012). Evaluation of the mental foramen and accessory mental foramen in Turkish patients using cone-beam computed tomography images reconstructed from a volumetric rendering program. *Clin Anat.* 25, 584-592.

[43] Katakami, K., Mishima, A., Shiozaki, K., Shimoda, S., Hamada, Y., Kobayashi, K., (2008). Characteristics of accessory mental foramina observed on limited cone-beam computed tomography images. *J Endod.* 34, 1441-1445.

[44] Imada, T. S., Fernandes, L. M., Centurion, B. S., de Oliveira-Santos, C., Honorio, H. M., Rubira-Bullen, I. R., (2014). Accessory mental foramina: prevalence, position and diameter assessed by cone-beam computed tomography and digital panoramic radiographs. *Clin Oral Implants Res.* 25, e94-99.

[45] von Arx, T., Friedli, M., Sendi, P., Lozanoff, S., Bornstein, M.M., (2013). Location and dimensions of the mental foramen: a radiographic analysis by using cone-beam computed tomography. *J Endod.* 39, 1522-1528.

[46] Fuakami, K., Shiozaki, K., Mishima, A., Shimoda, S., Hamada, Y., Kobayashi, K., (2011). Detection of buccal perimandibular neurovascularisation associated with accessory foramina using limited cone-beam computed tomography and gross anatomy. *Surg Radiol Anat.* 33, 141-146.

[47] Muinelo-Lorenzo, J., Suarez-Quintanilla, J. A., Fernandez-Alonso, A., Varela-Mallou, J., Suarez-Cunqueiro, M. M., (2015). Anatomical characteristics and visibility of mental foramen and accessory mental foramen: Panoramic radiography vs. cone beam CT. *Med Oral Patol Oral Cir Bucal.* 20, e707-714.

[48] Capote, T. S., Goncalves Mde, A., Campos, J. A., (2015). Retromolar Canal Associated with Age, Side, Sex, Bifid Mandibular Canal, and Accessory Mental Foramen in Panoramic Radiographs of Brazilians. *Anat Res Int.* 434083.

[49] Kqiku, L., Weiglein, A., Kamberi, B., Hoxha, V., Meqa, K., Stadtler, P., (2013). Position of the mental foramen in Kosovarian population. *Coll Antropol.* 37, 545-549.

[50] Naitoh, M., Yoshida, K., Nakahara, K., Gotoh, K., Ariji, E., (2011). Demonstration of the accessory mental foramen using rotational panoramic radiography compared with cone-beam computed tomography. *Clin Oral Implants Res.* 22, 1415-1419.

[51] Al-Khateeb, T., Al-Hadi Hamasha, A., Ababneh, K.T., (2007). Position of the mental foramen in a northern regional Jordanian population. *Surg Radiol Anat.* 29, 231-237.

[52] Iwanaga, J., Saga, T., Tabira, Y., Nakamura, M., Kitashima, S., Watanabe, K., Kusukawa, J., Yamaki, K., (2015). The clinical anatomy of accessory mental nerves and foramina. *Clin Anat.* 28, 848-856.

[53] Cantekin, K., Sekerci, A., (2014). Evaluation of the accessory mental foramen in a pediatric population using cone-beam computed tomography. *J Clin Pediatr Dent.* 39, 85-89.

[54] Santos, O. Jr., Pinheiro, L. R., Umetsubo, O. S., Sales, M. A., Cavalcanti, M.G., (2013). Assessment of open source software for CBCT in detecting additional mental foramina. *Braz Oral Res.* 27: 128-135.

[55] Goregen, M., Miloglu, O., Ersoy, I., Bayrakdar, I. S., Akgul, H. M., (2013). The assessment of accessory mental foramina using cone-beam computed tomography. *Turkish J Med Sci.* 43, 479-483.

[56] Sisman, Y., Sahman, H. Sekerci, A., Tokmak, T.T., Aksu, Y., Mavili, E., (2012) Detection and characterization of the mandibular accessory buccal foramen using CT. *Dentomaxillofac Radiol.* 41, 558-563.

[57] Oliveira-Santos, C., Souza, P. H., de Azambuja Berti-Couto, S., Stinkens, L., Moyaert, K., Van Assche, N., Jacobs, R., (2011). Characterisation of additional mental foramina through cone beam computed tomography. *J Oral Rehabil.* 38, 595-600.

[58] Naitoh, M., Nakahara, K., Suenaga, Y., Gotoh, K., Kondo, S., Ariji, E., (2010). Comparison between cone-beam and multislice computed tomography depicting mandibular neurovascular canal structures. *Oral Surg Oral Med Oral Pathol Oral Radiol Endod.* 109, e25-31.

[59] Haktanir, A., Ilgaz, K., Turhan-Haktanir, N., (2010) Evaluation of mental foramina in adult living crania with MDCT. *Surg Radiol Anat.* 32, 351-356.

Reviewed by Maria Mercedes Suárez Cunqueiro.

In: Computed Tomography
Editor: Deborah Carter
ISBN: 978-1-53610-766-1

Chapter 3

ACCURATE ANALYSIS OF NASOPALATINE CANAL USING CONE BEAM COMPUTED TOMOGRAPHY

A. Fernández-Alonso, J. Muinelo-Lorenzo and M. M. Suárez-Cunqueiro
Department of Surgery and Medical Surgical Specialties,
University of Santiago de Compostela,
Santiago de Compostela, Spain

ABSTRACT

The nasopalatine canal is an anatomic limitation that interferes with implant placement when ridge resorption is present. The nasopalatine canal is connected to the nasal cavity through the foramina of Stenson, and to the oral cavity through the incisive foramen. The nasopalatine canal contains the terminal branch of the descending nasopalatine artery and the nasopalatine nerve. Due to nasopalatine canal anatomy being highly variable, for dental implant treatment planning and placement, a precise anatomic description is necessary.

The critical region anterior to the nasopalatine canal is defined as an anatomic area that we should not invade surgically, to avoid neurovascular complications and failure of implant osseointegration. Due to bone ridge resorption after tooth loss, the nasopalatine canal can occupy up to 58% of buccal plate width, the area available for implant placement. This critical region may be evaluated with accuracy three

dimensionally using cone beam computed tomography (CBCT) to ensure proper implant position.

This chapter shows the morphometric characteristics of the nasopalatine canal, the nasopalatine angle, the dimensions of the buccal bone plate, and the palatal bone plate relative to the nasopalatine canal. This description is based on the analysis of three anatomic planes by CBCT.

Keywords: computed tomography, cone beam, incisive canal, nasopalatine canal, incisive foramen, foramina of Stenson, buccal bone plate, palatal bone plate, premaxilla bone

INTRODUCTION

Cone beam computed tomography (CBCT) is a tridimensional radiological technique for evaluating any bone structure of the patient, obtaining adequate precision on the three anatomic planes, despite obtaining only one base image (axial slice) through which the other image planes (sagittal and coronal slices) are reconstructed. In this chapter we evaluate different anatomic structures of the oral and maxillofacial region, in particular from the region of the nasopalatine canal.

Premaxillary Region

The nasopalatine canal is an anatomic limitation that interferes with implant placement when ridge resorption is present [1-4]. Radiological studies with CBCT make it possible to analyze anatomic variations of the nasopalatine canal [5, 6] and to determine the degree of buccal bone plate resorption in the anterior maxilla region after tooth loss [7-15]. The critical region anterior to the nasopalatine canal is defined as an anatomic area that we should not invade surgically, to avoid neurovascular complications and failure of implant osseointegration. Due to bone ridge resorption, the nasopalatine canal can occupy up to 58% of buccal plate width, the area available for implant placement. Buccal bone plate resorption occurs after tooth extractions, dento-alveolar trauma, periradicular and periodontal pathology, or because of tumors or cysts. The pattern of bone resorption has been studied by many authors, [7-

14] and it is generally horizontal, from the buccal surface to the palatal surface of the buccal bone plate [11].

This critical region may be evaluated with accuracy three dimensionally to ensure proper implant position. In general, the accuracy of measurements using linear CBCT is adequate [16-18]. However, it should be noted that measurement accuracy may be affected by the quality of the image due to attenuation of soft tissues, metal artifacts, patient movement, and variation of the radiation used in CBCT [19].

In the sagittal slice, the following anatomic structures are present in CBCT (Figure 1). In this chapter we will evaluate the nasopalatine canal and the adjacent premaxillary bone.

- Anterior nasal spine
- Premaxillary bone
- Alveolar bone processes
- Vomer
- Stenson foramina
- Nasopalatine canal
- Incisive foramen
- Nasal fossa
- Palatine processes of maxillary
- Transversal palatine suture
- Horizontal plate of palatine bone
- Posterior nasal spine

Nasopalatine Canal: Brief Anatomic Description

Williams et al. [20] describes the nasopalatine canal as being located in the midline of the palate, posterior to the roots of the central maxillary incisors. The nasopalatine canal is connected to the nasal cavity through the foramina of Stenson, and to the oral cavity through the incisive foramen. The nasopalatine canal contains the terminal branch of the descending nasopalatine artery and the nasopalatine nerve [20, 21]. In addition, it contains fibrous connective tissue, adipose tissue, and even minor salivary glands. Inadequate attention to this anatomic region may lead to nerve injury and impede dental implant osseointegration [22, 23].

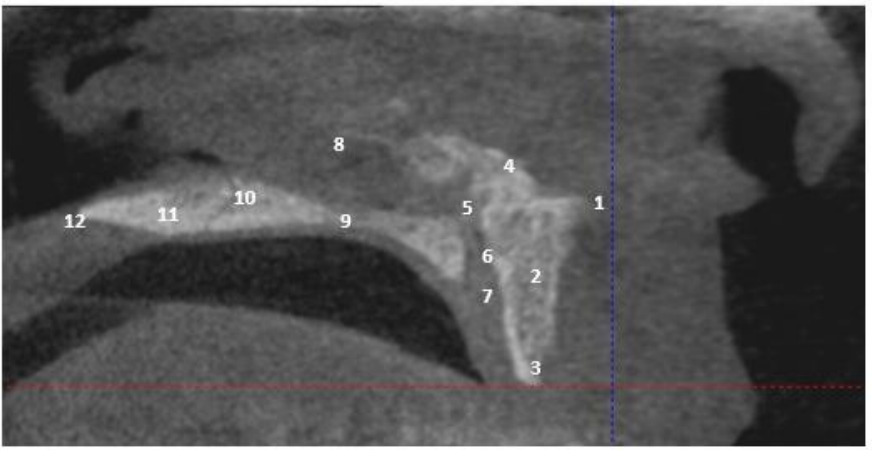

Figure 1. Anatomic structures: (a) anterior nasal spine, (b) premaxillary bone, (c) alveolar bone processes, (d) vomer, (e) Stenson foramina, (f) nasopalatine canal, (g) incisive foramen, (h) nasal fossa, (i) palatine processes of maxillary, (j) transversal palatine suture, (k) horizontal plate of palatine bone, and (l) posterior nasal spine.

Due to the nasopalatine canal anatomy being highly variable, for dental implant treatment planning and placement, a precise anatomic description is necessary for carrying out adequate implant treatment planning and insertion of dental implants [22, 24-29].

Analysis Using CBCT: Nasopalatine Canal Evaluation

For an analysis of the complete nasopalatine canal we must study the three anatomic planes and determine landmarks for careful study that are reproducible. This section will show how to systematically study the anterior area of the premaxilla, step by step, in a simultaneous 3D study, using linear measurements and the location of a simple landmark from which to develop the rest of the analysis.

Measurements of the nasopalatine canal, buccal bone plate, and palatal bone plate are carried out in three locations, level 1, level 2, and level 3 (Figure 2), defined in the following sections.

Axial Slice

To begin the analysis we focus first on the axial slices; CBCT images allow identifying the incisive foramen at level 1, the diameters of the nasopalatine canal at level 2, and the Stenson foramina at level 3.

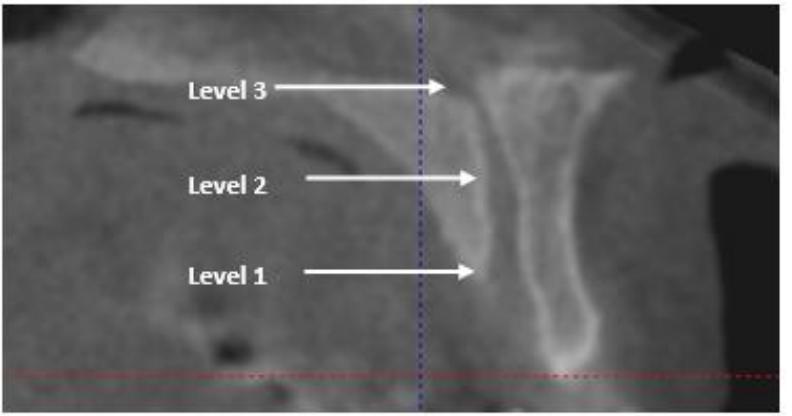

Figure 2. Levels to standardize analysis of the nasopalatine canal. level 1: incisive foramen; level 2: midpoint of the nasopalatine canal length; level 3: Stenson foramina.

The principal evaluations that scientific research [30-32] performs are:

- Level 1: buccal-palatal diameter (bpD1) and transversal diameter (tD1) of nasopalatine canal
- Level 2: buccal-palatal diameter (bpD2) and transversal diameter (tD2) of nasopalatine canal
- Level 3: in most cases only a morphological analysis can be performed, due to low image quality in the nasal floor region

Sagittal Slice

On the sagittal slices, CBCT images allow identifying the complete course of the nasopalatine canal. The principal evaluations that scientific research [30-32] performs are:

- Nasopalatine canal length
- Level 1: nasopalatine canal sagittal diameter (SD1)
- Level 2: nasopalatine canal sagittal diameter (SD2)
- Level 3: nasopalatine canal sagittal diameter (SD3)

Coronal Slice

On the axial slices, CBCT images allow identifying the complete course of the nasopalatine canal. The principal evaluations that scientific research [30-32] performs are:

- Level 1: coronal diameter of nasopalatine canal (CD1)
- Level 2: coronal diameter of nasopalatine canal (CD2)
- Level 3: coronal diameter of nasopalatine canal (CD3)

Detailed Analysis of Nasopalatine Canal in CBCT

The measures presented in the previous section are explained below in detail; we obtain a complete analysis of the nasopalatine canal on three levels and in the three anatomic planes.

Level 1

Level 1, Axial Slice

In the axial slice we must first locate the nasopalatine canal in the anterior region of the premaxilla, when the incisive foramen is completely closed (Figure 3). This is the first landmark and it is named level 1. To visualize the closed incisive foramen it is necessary to perform a dynamic vision in the axial plane.

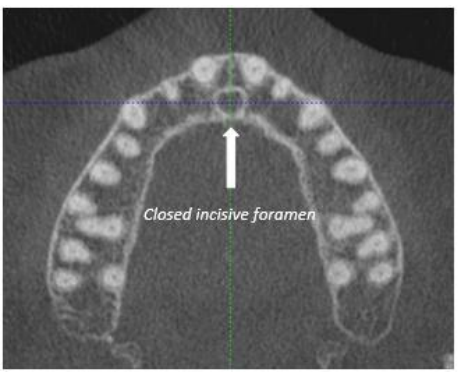

Figure 3. Localization of level 1. The incisive foramen is completely closed in axial slice.

Buccal-palatal diameter of nasopalatine canal at level 1. The bpD1 corresponded to the maximum diameter between the buccal and palatal bone cortical of the nasopalatine canal (Figure 4).

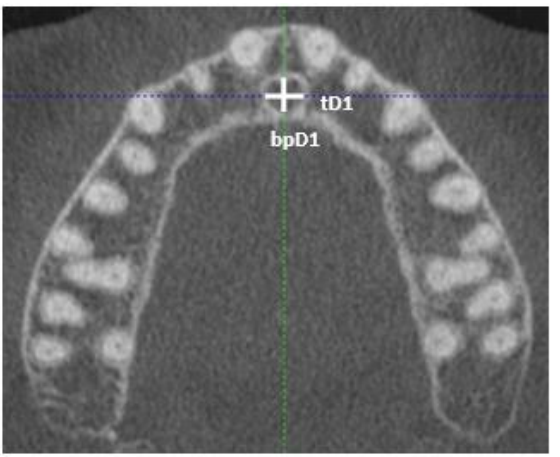

Figure 4. Axial plane. bpD1: buccal-palatal diameter of nasopalatine canal at level 1; tD1: transversal diameter at level 1.

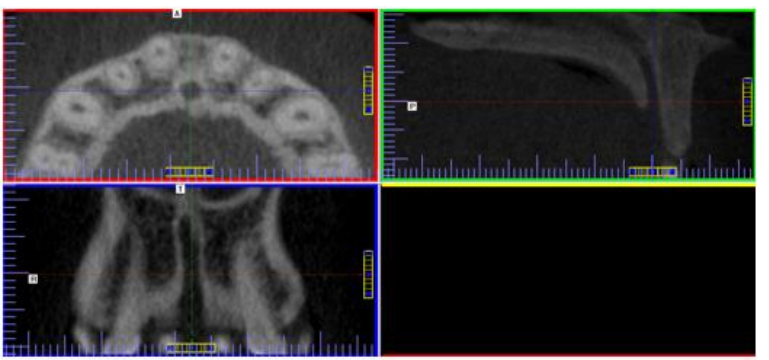

Figure 5. Simultaneous localization, level 1, in the three anatomic planes due to placement of the cursors in the center of the nasopalatine canal in the axial plane.

Transversal diameter of nasopalatine canal at level 1. The tD1 is the maximum diameter perpendicular to bpD1 (Figure 4). At this time level 1 is located, and it is recommended to perform measurements in the sagittal and coronal planes to optimize working time (Figure 5).

Level 1, Sagittal Slice

Sagittal diameter of nasopalatine canal at level 1. SD1 corresponded to the maximum diameter between the buccal and palatal bone cortical of the nasopalatine canal (Figure 6).

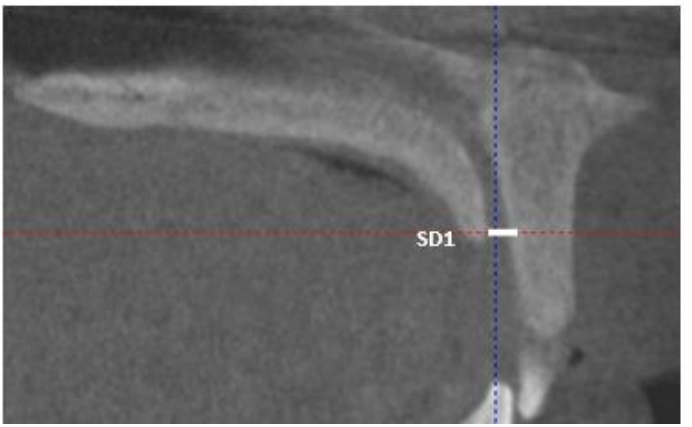

Figure 6. Sagittal plane. SD1: sagittal diameter of nasopalatine canal at level 1.

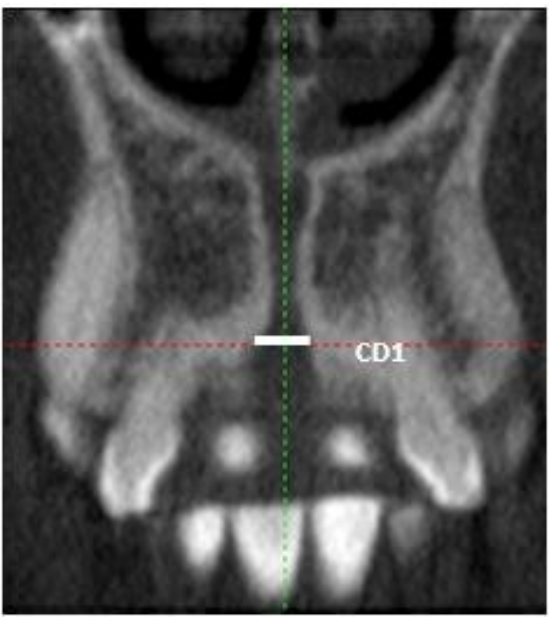

Figure 7. Coronal slice. CD1: coronal diameter of nasopalatine canal at level 1.

Level 1, Coronal Slice

Coronal diameter of nasopalatine canal at level 1. CD1 corresponded to the maximum diameter between both bone corticals of the nasopalatine canal (Figure 7).

Level 2

To locate level 2, move the horizontal line to the middle point of the length of the nasopalatine canal on the sagittal plane. Nasopalatine canal length is defined as the distance from the incisive foramen to the foramina of Stenson (Figure 8).

Level 2: Sagittal Slice

Sagittal diameter of nasopalatine canal at level 2. SD2 corresponded to maximum diameter between the buccal and palatal bone cortical of the nasopalatine canal (Figure 8). At this time level 2 is located simultaneously in the axial and coronal planes, and it is recommended to perform measurements in these planes to optimize working time (Figure 9).

Level 2, Axial Slice

Buccal-palatal diameter of nasopalatine canal at level 2.

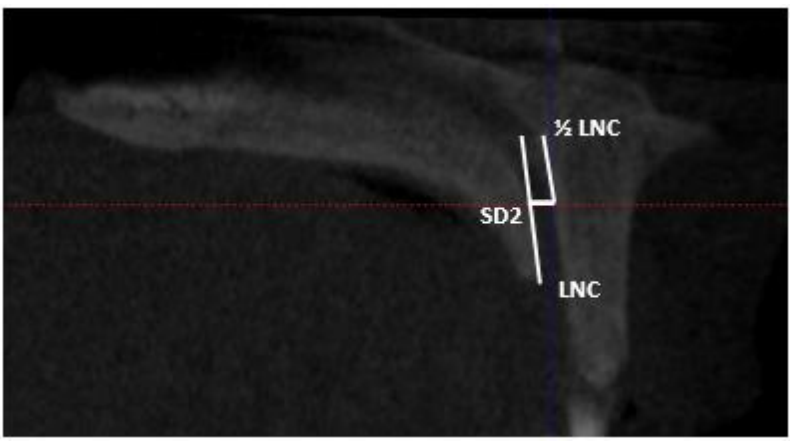

Figure 8. Sagittal slice, localization of level 2. LNC (length of nasopalatine canal); ½LNC: midpoint of LNC to locate level 2; SD2: sagittal diameter of nasopalatine canal at level 2.

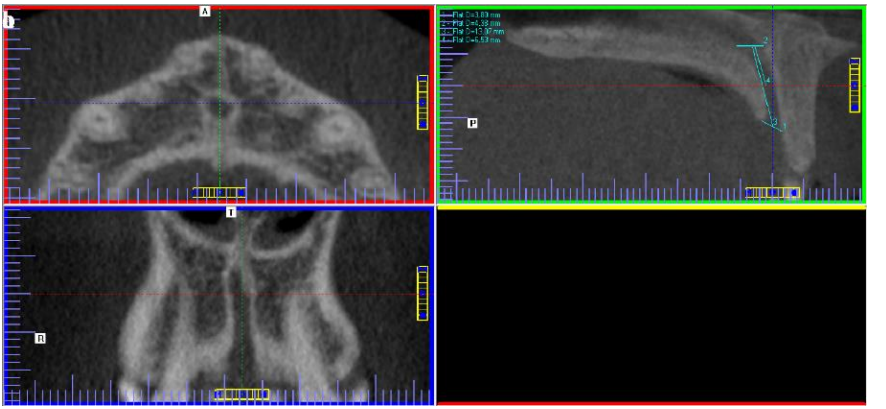

Figure 9. Simultaneous localization level 2 in the three anatomic planes due to placement of the cursors in the center of the nasopalatine canal in the axial plane.

The bpD2 corresponded to the maximum diameter between the buccal and palatal bone cortical of the nasopalatine canal. (Figure 10).

Transversal diameter of nasopalatine canal at level 2. The tD2 is the maximum diameter perpendicular to bpD2 (Figure 10).

Level 2, Coronal Slice

Coronal diameter of nasopalatine canal at level 2.

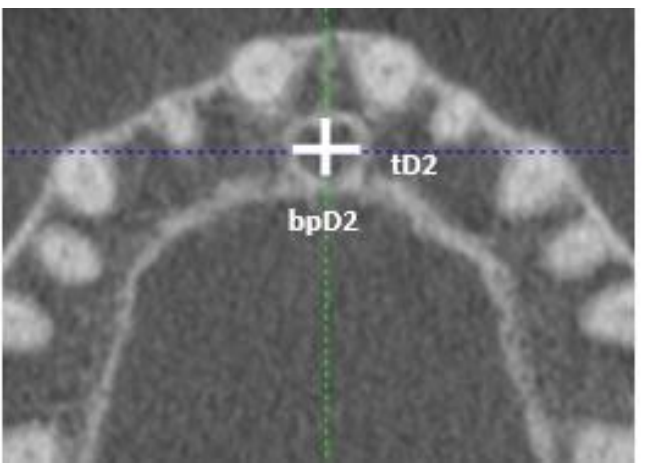

Figure 10. Axial slice. bpD2: buccal-palatal diameter of nasopalatine canal at level 2; tD2: transversal diameter at level 2.

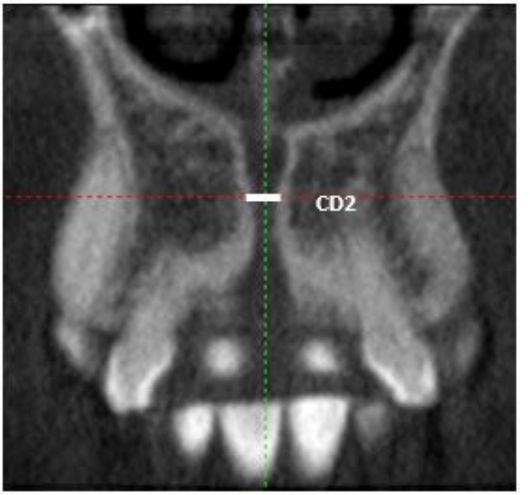

Figure 11. Coronal slice. CD2: coronal diameter of nasopalatine canal at level 2.

CD2 corresponded to the maximum diameter between both bones cortical of the nasopalatine canal (Figure 11).

Level 3

To locate level 3, move the horizontal line to the foramina of Stenson on the sagittal plane (Figure 12).

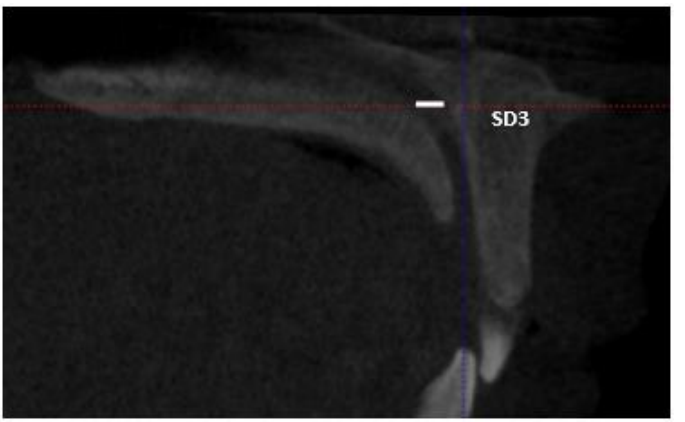

Figure 12. Sagittal slice, localization of level 3. SD3: sagittal diameter of nasopalatine canal at level 3.

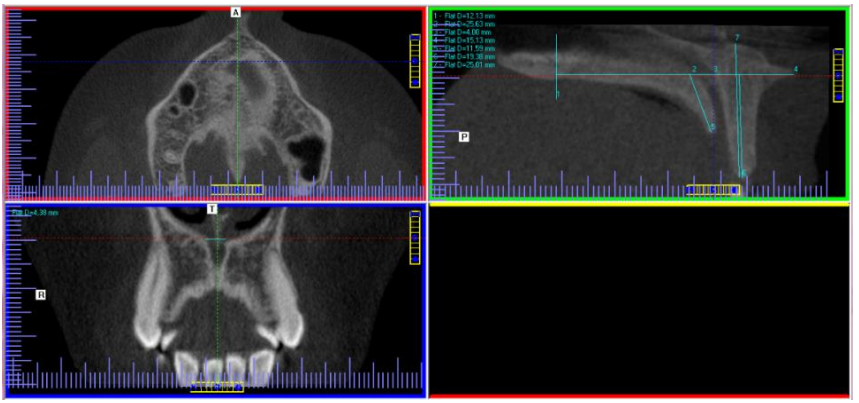

Figure 13. Simultaneous localization, level 3, in the three anatomic planes due to placement of the cursor in the center of the nasopalatine canal in the axial plane.

Level 3, Sagittal Slice

Sagittal diameter of nasopalatine canal at level 3. SD3 corresponded to the maximum diameter between the buccal and palatal bone cortical of the nasopalatine canal (Figure 12). At this time level 3 is located simultaneously in the axial and coronal planes, and it is recommended to perform measurements in the coronal plane to optimize working time. The axial slice cannot be measured due to a low-quality image at the foramina of Stenson (Figure 13).

Coronal diameter of nasopalatine canal at level 3. CD3 corresponded to the maximum diameter between both bones cortical of the nasopalatine canal (Figure 14).

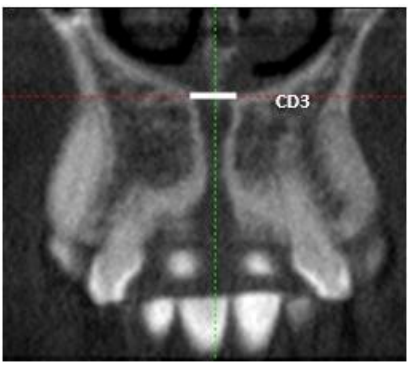

Figure 14. Coronal slice. CD3: coronal diameter of nasopalatine canal at level 3.

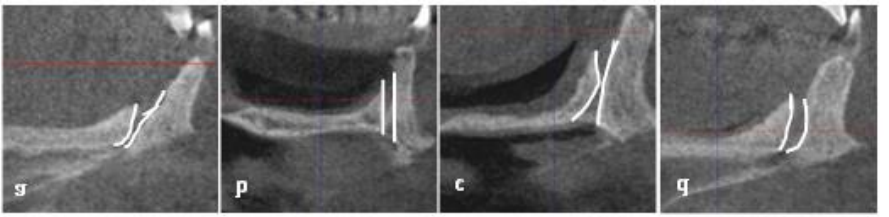

Figure 15. Sagittal shapes of nasopalatine canal. (a) funnel-like; (b) cylindrical; (c) hourglass-like; and (d) banana-like.

Figure 16. Sagittal direction and course of nasopalatine canal. (a) vertical straight; (b) vertical curved; (c) slanted straight; and (d) slanted curved.

Classifications of the Anatomic Variants of Nasopalatine Canal in the Three Dimensions

Sagittal Shapes of Nasopalatine Canal

In sagittal slices, the nasopalatine canal may present the following anatomic variants [27] (Figure 15):

- Funnel-like. The nasopalatine canal presents a wide incisive foramen and narrow foramina of Stenson.
- Cylindrical. The incisive foramen and foramina of Stenson have a similar width.
- Hourglass-like. The nasopalatine canal has a narrow isthmus in the middle.
- Banana-like. The nasopalatine canal has a wider area in its medial portion, i.e., it has the shape of a banana or half-moon.

Sagittal Direction and Course of Nasopalatine Canal

The nasopalatine canal can also be classified according to its sagittal direction and course [28] (Figure 16). The nasopalatine canal direction is

considered vertical when the canal is perpendicular from the nasal floor to the oral cavity, and it is considered oblique when it is not perpendicular.

The nasopalatine canal course is considered straight when the canal connects the foramina of Stenson and incisive foramen without breaking the linearity; and, the nasopalatine canal course is considered curved when the linearity from the foramina of Stenson is changed to the incisive foramen. Four categories are distinguished:

- Vertical straight (Ia)
- Vertical curved (Ib)
- Slanted straight (IIa)
- Slanted curved (IIb)

Coronal Shapes of Nasopalatine Canal

In coronal slices, the anatomic variants of the nasopalatine canal were classified into three groups [24] (Figure 17):

- Single canal. The nasopalatine canal does not show septations from the incisive foramen to the foramina of Stenson.
- Two parallel canals. The nasopalatine canal shows one septation from the incisive foramen to the foramina of Stenson.
- Variations of the Y-type canal. The nasopalatine canal shows one or more septations at the foramina of Stenson portion.
    - Ya, with one incisive foramen and two foramina of Stenson
    - Yb, with one incisive foramen and three foramina of Stenson
    - Yc, with one incisive foramen and more than three foramina of Stenson

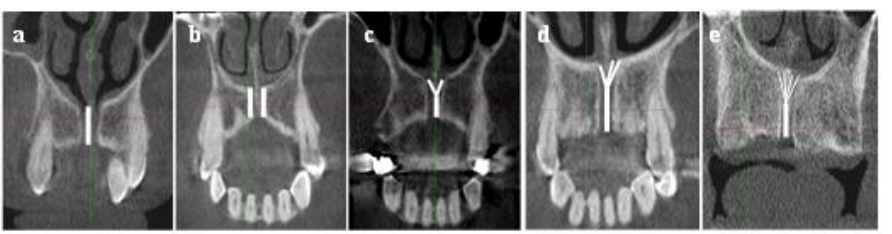

Figure 17. Coronal shapes of nasopalatine canal. (a) single canal; (b) two parallel canals; (c) Ya-type canal; (d) Yb-type canal; and (e) Yc-type canal.

Additionally, a patient could have a combination of nasopalatine canal coronal shapes—all nasopalatine canal slices were analyzed travelling from the anterior to the posterior view, i.e., performing a dynamic vision of the coronal plane (Figure 18).

Axial Shapes of Nasopalatine Canal

In axial slices, the anatomic variants of the nasopalatine canal are classified according to the number of incisive foramina and the number of foramina of Stenson.

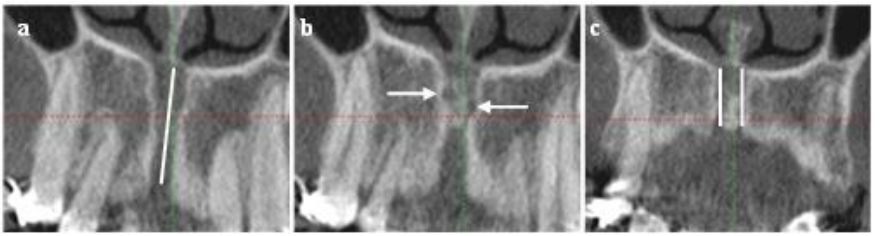

Figure 18. Anteroposterior radiological succession on coronal plane. (a) nasopalatine canal with a single canal; (b) anastomosis of a single canal with two parallel canals; and (c) nasopalatine canal with two parallel canals.

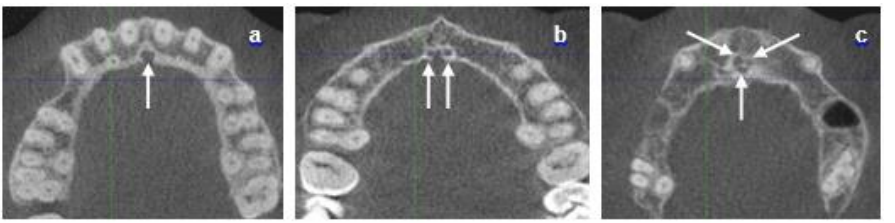

Figure 19. Axial slices at level 1. (a) one incisive foramen; (b) two; and (c) three incisive foramina.

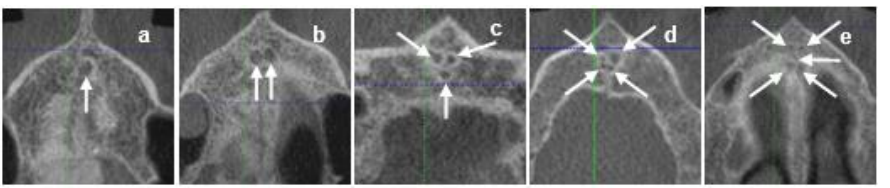

Figure 20. Axial slice at level 3. (a) one Stenson foramen; (b) two; (c) three; (d) four; and (e) five Stenson foramina.

The number of openings in the incisive foramen and the openings in the foramina of Stenson are shown in CBCT images Figures 19 and 20.

Conventional 2D Radiographs Versus CBCT Images

Intraoral and panoramic radiographs are the basic X-rays used in dentistry [33]. These radiological images serve to get an overview of the jaw or skull, to detect impacted teeth, to determine jaw pathology for medium or large size, and to evaluate the temporomandibular joint [34].

These radiological techniques represent a very important contribution to visualize the oral and maxillofacial structures. However, being 2D projections, they have limitations, such as certain magnification; overlapping anatomic structures and pathological entities; nonexact determination of the relationship between teeth and surrounding anatomic structures; [35] and, although these 2D images allow visualization of the mesial, distal, and apical areas, they do not allow analysis of the buccal and lingual areas [36-38].

Conventional computed tomography (CT) and CBCT are radiological techniques that allow a 3D study. CBCT was developed as an alternative to CT. CBCT emits a cone beam X-ray, presenting lower radiation than CT. The irradiated area can be selected, which allows obtaining data of segmented anatomic areas with faster data acquisition and thus fewer artifacts are generated by the movement of patients. This is more economical than CT.

However, CBCT has disadvantages compared to CT, such as less detail of soft tissues, more scattered radiation, and a greater number of artifacts due to dental restorations (e.g., amalgam reconstructions, fixed prostheses, implants) [16, 17, 39].

When the nasopalatine canal is analyzed with 2D radiographs, limitations versus CBCT are clear, as highlighted below (Figure 21):

- Elongation of anatomic structures (incisors and nasopalatine canal)
- Unclear for locating the incisive foramen
- Unclear for locating foraminas of Stenson
- Inability to do anteroposterior anatomic study
- Inability to specify shape of the nasopalatine canal

Figure 21. (a) 2D radiography of nasopalatine canal; (b) axial slice of nasopalatine canal on CBCT; (c) sagittal slice of nasopalatine canal on CBCT; and (d) coronal slice of nasopalatine canal on CBCT.

Clinical Implications

Due to the close relationship between the nasopalatine canal and the roots of the upper central incisors, careful radiological analysis is necessary when rehabilitation with dental implants is planned in this area. To this we must add that the anterior maxillary area is the area with the highest aesthetic demand, so dental implant placement should not be based only on surgical positioning splints, because we can cause damage to the nasopalatine canal [1, 3, 4]. The analysis must be completed with a 3D radiological study. Thus, the correct position of the dental implant is planned without damaging the nasopalatine canal, if necessary with assessment of bone regeneration of the buccal bone plate.

Recent studies [30, 32, 40, 41] show variability in morphology and in the number of nasopalatine canal channels; therefore CBCT is recommended to

help assure better anesthesia and to avoid any complications arising from surgery.

The nasopalatine canal contains the most nerves, arteries, and veins nourishing the premaxillary region. Invasion of the nasopalatine canal should be avoided to not cause neurovascular complications and paresthesias. Therefore, another clinical implication is the necessity of assessing the direction and course of the nasopalatine canal for dental implant placement in this region.

Evaluation of a single anatomic plane on CBCT does not provide statistically significant information [32] from the nasopalatine canal or the premaxilla region. This can generate an inaccurate clinical idea of nasopalatine canal morphometry, which can cause complications in the surgery. Therefore, careful analysis in the three anatomic planes is of fundamental clinical relevance to avoid the failure of osseointegration [42] and subsequent medical problems, [24, 43] such as hemorrhages and/or sensory dysfunction, during placement of dental implants or any other procedure in the vicinity of the nasopalatine canal area.

REFERENCES

[1] Artzi Z., Nemcovsky C. E., Bitlitum I., Segal P. Displacement of the incisive foramen in conjunction with implant placement in the anterior maxilla without jeopardizing vitality of nasopalatine nerve and vessels: a novel surgical approach. *Clin. Oral Implants Res*., 2000;11(5):505 - 10.

[2] Penarrocha M., Carrillo C., Uribe R., Garcia B. The nasopalatine canal as an anatomic buttress for implant placement in the severely atrophic maxilla: a pilot study. *Int. J. Oral Maxillofac. Implants*, 2009;24(5): 936 - 42.

[3] Rosenquist J. B., Nystrom E. Occlusion of the incisal canal with bone chips: a procedure to facilitate insertion of implants in the anterior maxilla. *Int. J. Oral Maxillofac. Surg*., 1992;21(4):210 - 11.

[4] Scher E. L. Use of the incisive canal as a recipient site for root form implants: preliminary clinical reports. *Implant Dent*., 1994;3(1):38 - 41.

[5] de Oliveira-Santos C., Rubira-Bullen I. R., Monteiro S. A., Leon J. E., Jacobs R. Neurovascular anatomical variations in the anterior palate observed on CBCT images. *Clin. Oral Implants Res*., 2013;24(9): 1044 - 48.

[6] Valcu M., Rusu M. C., Sendroiu V. M., Didilescu A. C. The lateral incisive canals of the adult hard palate: aberrant anatomy of a minor form of clefting? *Rom. J. Morphol. Embryol*., 2011;52(3):947 - 49.

[7] Atwood D. A. Some clinical factors related to rate of resorption of residual ridges. *J. Prosthet. Dent*., 2001;86(2):119 - 25.

[8] Atwood D. A. Bone loss of edentulous alveolar ridges. *J. Periodontol*., 1979;50(4):11 - 21.

[9] Araujo M. G., Lindhe J. Dimensional ridge alterations following tooth extraction: an experimental study in the dog. *J. Clin. Periodontol*., 2005;32(2):212 - 18.

[10] Mercier P. Resorption patterns of the residual ridge. In: Block M. S., Kent J. N., Guerra L. R. *Implants in Dentistry: Essentials of Endosseous Implants for Maxillofacial Reconstruction*. Philadelphia: Saunders; 1997.

[11] Cawood J. I., Howell R. A. A classification of the edentulous jaws. *Int. J. Oral Maxillofac. Surg*., 1988;17(4):232 - 36.

[12] Cawood J. I., Howell R. A. Reconstructive preprosthetic surgery. I. Anatomical considerations. *Int. J. Oral Maxillofac. Surg*., 1991;20(2): 75 - 82.

[13] Pietrokovski J., Starinsky R., Arensburg B., Kaffe I. Morphologic characteristics of bony edentulous jaws. *J. Prosthodont*., 2007;16(2): 141 - 47.

[14] Trombelli L., Farina R., Marzola A., et al. Modeling and remodeling of human extraction sockets. *J. Clin. Periodontol*., 2008;35(7):630 - 39.

[15] Van der Weijden F., Dell'Acqua F., Slot D. E. Alveolar bone dimensional changes of post-extraction sockets in humans: a systematic review. *J. Clin. Periodontol*., 2009;36(12):1048 - 58.

[16] Mozzo P., Procacci C., Tacconi A., Martini P. T., Andreis I. A. A new volumetric CT machine for dental imaging based on the cone-beam technique: preliminary results. *Eur. Radiol*., 1998;8(9):1558 - 64.

[17] Kamburoglu K., Murat S., Kolsuz E., et al. Comparative assessment of subjective image quality of cross-sectional cone-beam computed tomography scans. *J. Oral Sci*., 2011;53(4):501 - 508.

[18] Suomalainen A., Vehmas T., Kortesniemi M., Robinson S., Peltola J. Accuracy of linear measurements using dental cone beam and conventional multislice computed tomography. *Dentomaxillofac. Radiol*., 2008;7(1):10 - 17.

[19] Periago D. R., Scarfe W. C., Moshiri M., et al. Linear accuracy and reliability of cone beam CT derived 3-dimensional images constructed using an orthodontic volumetric rendering program. *Angle Orthod.*, 2008;78(3):387 - 95.

[20] Williams P. L., Warwick R., Dyson M., Bannister L. H. *Gray's Anatomy*. Edinburgh: Churchill Livingstone; 1989.

[21] Rouvière H., Delmas A. *Human Anatomy: Descriptive, Topography and Functional*. Barcelona: Masson; 1991.

[22] Buser D., Martin W., Belser U. C. Optimizing esthetics for implant restorations in the anterior maxilla: anatomic and surgical considerations. *Int. J. Oral Maxillofac. Implants*, 2004;19 Suppl.:43 - 61.

[23] Branemark P. I. Osseointegration and its experimental background. *J. Prosthet. Dent.*, 1983;50(3):399 - 410.

[24] Bornstein M. M., Balsiger R., Sendi P., von Arx T. Morphology of the nasopalatine canal and dental implant surgery: a radiographic analysis of 100 consecutive patients using limited cone-beam computed tomography. *Clin. Oral Implants Res.*, 2011;22(3):295 - 301.

[25] Guncu G. N., Yildirim Y. D., Yilmaz H. G., et al. Is there a gender difference in anatomic features of incisive canal and maxillary environmental bone? *Clin. Oral Implants Res.*, 2013;24(9):1023 - 26.

[26] Liang X., Jacobs R., Martens W., et al. Macro- and micro-anatomical, histological and computed tomography scan characterization of the nasopalatine canal. *J. Clin. Periodontol.*, 2009;36(7):598 - 603.

[27] Mardinger O., Namani-Sadan N., Chaushu G., Schwartz-Arad D. Morphologic changes of the nasopalatine canal related to dental implantation: a radiologic study in different degrees of absorbed maxillae. *J. Periodontol.*, 2008;79(9):1659 - 62.

[28] Song W. C., Jo D. I., Lee J. Y., et al. Microanatomy of the incisive canal using three-dimensional reconstruction of microCT images: an ex vivo study. *Oral Surg. Oral Med. Oral Pathol. Oral Radiol. Endod.*, 2009;108(4):583 - 90.

[29] Tözüm T. F., Guncu G. N., Yildirim Y. D., et al. Evaluation of maxillary incisive canal characteristics related to dental implant treatment with computerized tomography: a clinical multicenter study. *J. Periodontol.*, 2012;83(3):337 - 43.

[30] Fernandez-Alonso A., Suarez-Quintanilla J. A., Rapado-Gonzalez O., Suarez-Cunqueiro M. M. Morphometric differences of nasopalatine canal based on 3D classifications: descriptive analysis on CBCT. *Surg. Radiol. Anat.*, 2015.

[31] Fernandez-Alonso A., Suarez-Quintanilla J. A., Muinelo-Lorenzo J., et al. Three-dimensional study of nasopalatine canal morphology: a descriptive retrospective analysis using cone-beam computed tomography. *Surg. Radiol. Anat*., 2014;36(9):895 - 905.

[32] Fernandez-Alonso A., Antonio Suarez-Quintanilla J., Muinelo-Lorenzo J., et al. Critical anatomic region of nasopalatine canal based on tridimensional analysis: cone beam computed tomography. *Sci. Rep*., 2015;5:12568.

[33] Boeddinghaus R., Whyte A. Current concepts in maxillofacial imaging. *Eur. J. Radiol*., 2008;66(3):396 - 418.

[34] Fazel R., Krumholz H. M., Wang Y., et al. Exposure to low-dose ionizing radiation from medical imaging procedures. *N. Engl. J. Med*., 2009;361(9):849 - 57.

[35] Cotti E., Vargiu P., Dettori C., Mallarini G. Computerized tomography in the management and follow-up of extensive periapical lesion. *Endod. Dent. Traumatol*., 1999;15(4):186 - 89.

[36] Patel S., Dawood A., Mannocci F., Wilson R., Pitt Ford T. Detection of periapical bone defects in human jaws using cone beam computed tomography and intraoral radiography. *Int. Endod. J*., 2009;42(6): 507-15.

[37] Patel S., Dawood A., Whaites E., Pitt Ford T. New dimensions in endodontic imaging: part 1. conventional and alternative radiographic systems. *Int. Endod. J*., 2009;42(6):447 - 62.

[38] Patel S. New dimensions in endodontic imaging: part 2. cone beam computed tomography. *Int. Endod. J*., 2009;42(6):463 - 75.

[39] Arai Y., Tammisalo E., Iwai K., Hashimoto K., Shinoda K. Development of a compact computed tomographic apparatus for dental use. *Dentomaxillofac. Radiol*., 1999;28(4):245 - 48.

[40] El Nahass H., et al. Analysis of the dimensions of the labial bone wall in the anterior maxilla: a cone-beam computed tomography study. *Clin. Oral Implants Res.*, 2014.

[41] Thakur A. R., Burde K., Guttal K., Naikmasur V. G. Anatomy and morphology of the nasopalatine canal using cone-beam computed tomography. *Imaging Sci. Dent*., 2013;43(4):273 - 81.

[42] Albrektsson T., Johansson C. Osteoinduction, osteoconduction and osseointegration. *Eur. Spine J*., 2001;10 Suppl. 2:S96 - 101.

[43] Jacobs R., Lambrichts I., Liang X., et al. Neurovascularization of the anterior jaw bones revisited using high-resolution magnetic resonance imaging. *Oral Surg. Oral Med. Oral Pathol. Oral Radiol. Endod*., 2007;103(5):683 - 93.

In: Computed Tomography
Editor: Deborah Carter
ISBN: 978-1-53610-766-1

Chapter 4

AN ASSESSMENT OF MORPHOMETRIC CHARACTERISTICS OF THE GREATER PALATINE CANAL USING CONE BEAM COMPUTED TOMOGRAPHY

O. Rapado-González, J. C. Pérez-Varela and M. M. Suárez-Cunqueiro*
Surgery and Medical Surgical Specialties,
Medicine and Dentistry School,
University of Santiago de Compostela,
Santiago de Compostela, Spain

ABSTRACT

Lorem ipsum dolor sit amet, consectetuer adipiscing elit. Maecenas porttitor congue massa. Fusce posuere, magna sed pulvinar ultricies, purus lectus malesuada libero, sit amet commodo magna eros quis urna. Nunc viverra imperdiet enim. Fusce est. Vivamus a tellus. Pellentesque habitant morbi tristique senectus et netus et malesuada fames ac turpis egestas. Proin pharetra nonummy pede. Mauris et orci. Cone Beam Computed Tomography (CBCT) is a useful tool for evaluating the greater palatine canal morphometrically on the three anatomic planes. The

*Corresponding author email: mariamercedes.suarez@usc.es

greater palatine canal is located in a critical anatomic area and has a great clinical relevance. The pterygopalatine fossa is connected to the oral cavity by the greater palatine canal. The pterygopalatine fossa contains the maxillary nerve, the maxillary artery, the venous rami and the pterygopalatine ganglion. The palatine nerves descend since pterygopalatine fossa through the greater palatine canal. The greater palatine nerve emerges on the palate through the greater palatine foramen and the lesser palatine nerves emerge through the lesser palatine foramina. The position of the greater palatine foramen is of great interest to dentists, maxillofacial surgeons and otolaryngologists for anesthetic purposes, and also for obtaining connective tissue grafts for periodontal purposes. The greater palatine canal allows blocking of the maxillary nerve and therefore allows anesthesia of the sinus, the maxillary teeth, the tissue palatal and the nasal region. Due to the greater palatine foramen being hidden by palatal mucosa thickness, a clinical and radiological location is necessary for treatment planning of several oral surgical procedures. CBCT images of the greater palatine foramen describe the dimensions and position of each greater palatine foramen with respect to different landmarks. An exact location of the greater palatine foramen is necessary to avoid damaging the greater palatine neurovascular bundle. Morphometric classifications of the greater palatine canal are important to applying anesthesia correctly and to avoid hemorrhagic risks. It is necessary to keep in mind that the greater palatine canal is a bone structure with numerous morpho-anatomical variations. The anatomy of the greater palatine canal can be a limiting factor in the block of the maxillary nerve. Nowadays, CBCT images provide an exhaustive anatomic description of the greater palatine foramen and the greater palatine canal in the axial, sagittal and coronal slices.

Keywords: cone-beam computed tomography, greater palatine foramen, greater palatine canal, lesser palatine canal, lesser palatine foramina, palatal region

INTRODUCTION

Cone Beam Computed Tomography (CBCT) is a promising technique for evaluating different anatomic structures of the oral and maxillofacial region. CBCT is a useful imaging modality to evaluate through the multiplanar images, the entire bony volume creating 3D-reconstructions not only of jaw

structures but also other areas of interest for clinicians. In the maxilla, CBCT images enable an exact reproduction of numerous anatomic structures as follows:

- Maxillary sinus
- Schneider membrane
- Nasal cavity and paranasal sinus
- Facial sutures and bones
- Temporomandibular joint
- Anterior region of maxilla
- Root and canal morphologies dental

On the other hand, CBCT images are essential in the diagnosis, treatment planning and post-therapeutic evolution of different dental and bone pathologies, related to periodontics, orthodontics, endodontics, implantology and restorative dentistry. In this sense, it is necessary to have an exhaustive anatomic description of neurovascular structures. In the palatal region, the greater palatine bundle is of interest to oral and maxillofacial surgeons, dentists and otolaryngologists.

Palatal Region

The palatal region originates at the top wall of the oral cavity and the osseo-membranous septum separating the oral cavity of the nasal cavities. Morphologically it represents a concave shape, both anteroposterior and transverse directions, covered entirely by oral mucosa. Above and laterally, it is limited by the upper dental arch, and a posterior ends in a free edge. It presents a palatal raphe on the midline, where at an anterior level it ends at the incisive papilla (at the incisive foramen) and at a posterior level it ends in the uvula. It also presents anteriorly and laterally narrow and irregular protrusions, denominated palatal transverse folds or palatal ridges. In the palatal region two anatomical structures are differentiated, the hard and soft palates [1].

The hard palate is formed by the palatine process of the maxilla in its two previous thirds and horizontal plates of the palatine bones in its posterior third. The palatine processes originate in the upper region of the medial side of each

alveolar process. Both palatine processes are linked by the midline palatal suture. The posterior portion of the hard palate is formed by the horizontal plates of the palatine bones. The palatine bone is formed by a horizontal plate and a vertical plate. The vertical plate is formed by its internal surface and part of the side wall of the nasal cavity. The horizontal plate has a smooth top face (*nasal*) forming part of the floor of the nasal cavities, and a lower rough face (*buccal*) forming the most posterior portion of the palatal vault, in which the lateral and medial palatal grooves are observed. Its posterior edge, confined to hard palate, and gives insertion to the palatal aponeurosis and muscles of the soft palate. The horizontal plate is projected medially from the underside of the palatine bone and joins with its partner in the midline, and on the same side with the palatine process of the maxilla. Above, both horizontal plates are linked with both palatine processes of the maxilla by the transverse palatine suture or palate-maxillary suture. The union of both horizontal plates in the midline and its backward projection from hard palate originates the posterior nasal spine. Both palatine bones contribute to the formation of the palatal vault, the nasal cavities, the orbit and the pterygomaxillary fossa [2-4].

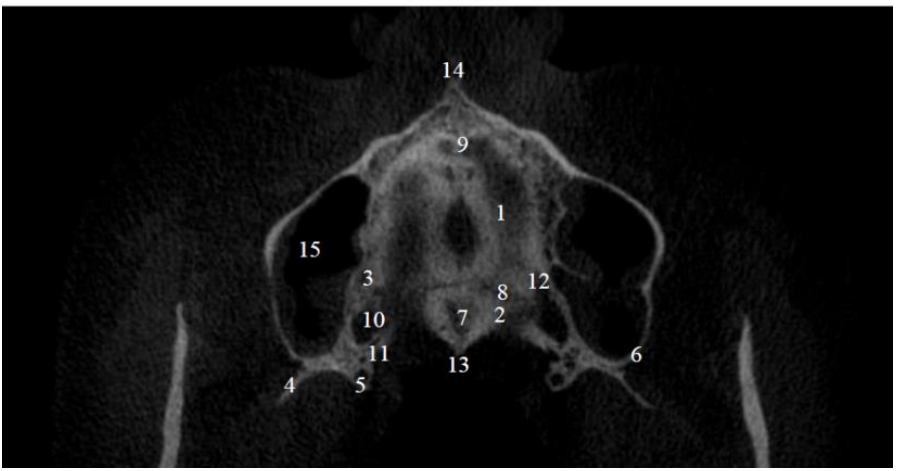

Figure 1. Anatomic structures of the palatal region: 1) palatine process of the maxilla, 2) horizontal plate of the palatine bone, 3) alveolar process, 4) pyramidal process of the palatine bone, 5) hook pterygoid, 6) maxillary tuberosity, 7) midline palatal suture, 8) transverse palatine suture, 9) incisive foramen, 10) greater palatine foramen, 11) lesser palatine foramen, 12) palatine grooves, 13) posterior nasal spine, 14) anterior nasal spine, and 15) maxillary sinus.

In the palatal region, the following anatomical structures are present on CBCT images (Figure 1):

1. Palatine processes of the maxilla
2. Horizontal plate of the palatine bone
3. Alveolar processes
4. Pyramidal process of the palatine bone
5. Hook pterygoid
6. Maxillary tuberosity
7. Midline palatal suture
8. Transverse palatine suture
9. Incisive foramen
10. Greater palatine foramen
11. Lesser palatine foramen
12. Palatine grooves
13. Posterior Nasal Spine
14. Anterior Nasal Spine
15. Maxillary sinus

Greater Palatine Canal and Greater Palatine Foramen

The pterygopalatine fossa is a complicated anatomical structure with the shape of a reverse pyramid. Inside is located the neurovascular bundle formed by the maxillary nerve, accompanied by the artery, the vein branches, and the pterygopalatine ganglion [5]. The pterygopalatine fossa presents numerous communications with other anatomical regions, such as the infratemporal fossa, the middle cranial fossa, the oral cavity, the orbit, the nasal cavity, the nasopharyngeal, and the cranial cavity [6]. At a lower level, the pterygopalatine fossa communicates with the oral cavity through the greater palatine canal, which leads to the greater palatine foramen on the surface of the palate.

Greater Palatine Neurovascular Bundle: Innervation and Vascularization

The maxillary nerve is the second branch of the trigeminal nerve (V2) with a wholly sensory function. The maxillary nerve enters in the pterygopalatine fossa through the round foramen resulting in numerous collateral branches. Attached to the maxillary nerve, the sphenopalatine

ganglion of Meckel is located where the greater palatine nerve (above) and the minor palatine nerves (middle, rear or accessories) originate. The greater palatine nerve is the main trunk of the palatine nerves. It emerges on the palate through the greater palatine foramen, innervating the mucosa of the hard palate and periodontal tissue of molars and premolars.

In its intra-canal route the inferior nasal nerve innervates the lower turbinate mucosa. The palatine nerves initially descend together from the pterygopalatine fossa through the greater palatine canal, and in the lower third, the lesser palatine nerves are separated from the greater palatine canal to the pyramidal process. The lesser palatine nerves lead to the palate through the lesser palatine foramina. Its function is to innervate the membranous soft palate, the tonsils and the uvula [7]. The greater palatine nerve is accompanied by the descending palatine artery, the collateral branch of the internal maxillary artery. The greater palatine neurovascular bundle formed by the arteria, the vein, and the nerve descends from the pterygopalatine fossa through the greater palatine canal, emerging on the palate through the greater palatine foramen.

On the palate, the greater palatine nerve runs forward in a groove almost up to the incisor teeth where it anastomoses with branches of the nasopalatine bundle.

Radiologic Analysis

A descriptive analysis of the greater palatine canal, greater palatine foramen and pterygopalatine fossa has been reported on High Resolution Computed Tomography (HRCT) [8-13] and CBCT studies [14-19] (Table 1):

A View on HRCT Based to Literature: Greater Palatine Foramen and Greater Palatine Canal

The following measurements have been determined on HRCT images [8-13]:

- Distance from the greater palatine foramen to the sphenopalatine foramen
- Distance from the greater palatine foramen to the orbital floor
- Distance from the greater palatine foramen to the midline maxillary suture

- Distance from the greater palatine foramen to the posterior border of the hard palate
- Distance from the greater palatine foramen to the alveolar ridge
- Distance from the greater palatine foramen to the incisive foramen
- Distance from the greater palatine foramen to the tip of pterygoid hamulus
- Distance from the greater palatine foramen to the posterior nasal spine
- Distance from the greater palatine foramen to the occlusal plane
- Distance from the greater palatine foramen to the anterior teeth
- Anteroposterior and transversal diameters of the greater palatine foramen
- Position of the greater palatine foramen in relation to the upper molars
- Length of the greater palatine canal
- Height of the pterygopalatine fossa
- Volume of the pterygopalatine fossa
- Mucosal thickness of the greater palatine canal
- Angle between the greater palatine foramen and the hard palate
- Angle between the greater palatine canal and vertical axis of the pterygopalatine fossa
- Angle among midline maxillary suture and incisive foramen and greater palatine foramen
- Evaluation of the presence of the greater palatine foramen posterior palatine crest
- Number of the lesser palatine foramen
- Evaluating of the greater palatine foramen opening direction

A View on CBCT Based to Literature: Greater Palatine Foramen and Greater Palatine Canal

The following measurements have been determined in the axial, sagittal and coronal slices [14-19]:

Axial Slices

CBCT images allow identifying the greater palatine foramen in axial slices. The principal objectives of the CBCT studies [16, 17, 19] on this plane were analyzed:

- Distance from the greater palatine foramen to the midline maxillary suture
- Distance from the greater palatine foramen to the buccal bone plane
- Distance from the greater palatine foramen to the posterior nasal plane
- Distance from the greater palatine foramen to the anterior nasal spine
- Distance from the greater palatine foramen to the alveolar ridge
- Anteroposterior and transversal diameters of the greater palatine foramen
- Position of the greater palatine foramen in relation to the upper molars

Table 1. HRCT and CBCT studies of the greater palatine foramen and greater palatine canal

Authors	Type of study	Anatomic structures
Das et al., 2006	HRCT	Greater palatine foramen
Douglas et a.l, 2006	HRCT	Greater palatine foramen, greater palatine canal, pterygopalatine fossa
McKinney et al., 2010	HRCT	Greater palatine foramen, greater palatine canal, pterygopalatine fossa
Howard et al., 2010	CBCT	Greater palatine canal
Hwang et al., 2011	HRCT	Greater palatine foramen, pterygopalatine fossa
Kang et al., 2012	HRCT	Greater palatine foramen
Sheikki et al., 2013	CBCT	Greater palatine canal
Ikuta et al., 2013	CBCT	Greater palatine foramen
Tomaszewska et al., 2014	HRCT	Greater palatine foramen, lesser palatine foramen
Rapado et al., 2015	CBCT	Greater palatine foramen, greater palatine canal
Yilmaz et al., 2015	CBCT	Greater palatine foramen
Aoun et al., 2015	CBCT	Greater palatine foramen

Sagittal Slices

CBCT images allow identifying the greater palatine canal in sagittal slices. The principal objectives of the CBCT studies [14, 15, 17] on this plane were the following:

- Length of the greater palatine canal
- Anatomic paths of the greater palatine canal
- Diameter of the greater palatine canal

Coronal Slices

CBCT images allow identifying the greater palatine canal in coronal slices. The principal objectives of the CBCT studies [14-17] on this plane were the following:

- Length of the greater palatine canal
- Anatomic paths of the greater palatine canal
- Diameter of the greater palatine canal
- Distance from the greater palatine canal to the midline maxillary suture

A Detailed Analysis on CBCT: Greater Palatine Foramen and Greater Palatine Canal

CBCT images show the morphoanatomical characteristics of the greater palatine foramen and the greater palatine canal in the three anatomical slices: axial, sagittal and coronal.

A thorough knowledge of the greater palatine foramen and canal requires the use of different anatomical landmarks on the three anatomical planes.

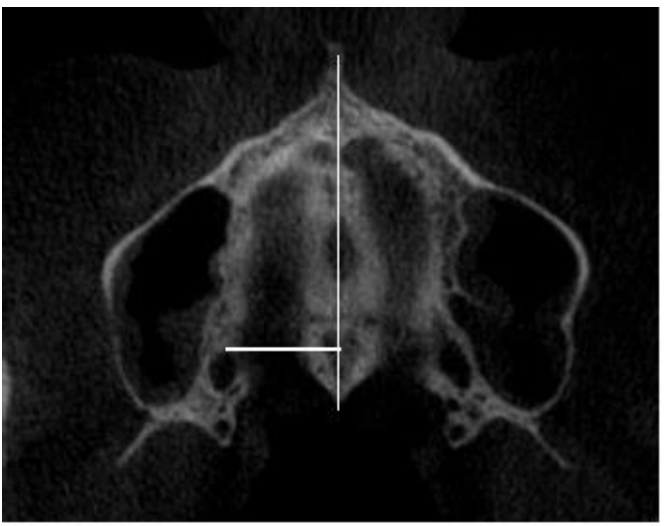

Figure 2. Distance from the greater palatine foramen to the midline maxillary suture.

Axial Slices

Axial slices show the distance and position of the greater palatine foramen in respect to various anatomical structures (bone or tooth) identified in the palatal region:

Distance from the greater palatine foramen to the midline maxillary suture (Figure 2). Greater palatine foramen distance to the midline maxillary suture has a range between 6-20.5 mm [16, 17, 19].

Distance from the greater palatine foramen to the posterior nasal plane (Figure 3).

The posterior nasal plane represents the most posterior point of the posterior nasal spine. Greater palatine foramen distance to the posterior nasal plane has a range between 0-9.75 mm [17].

Distance from the greater palatine foramen to the anterior nasal spine (Figure 4). The anterior nasal spine is located at a distance of greater palatine foramen between 39.05-60 mm [17, 19].

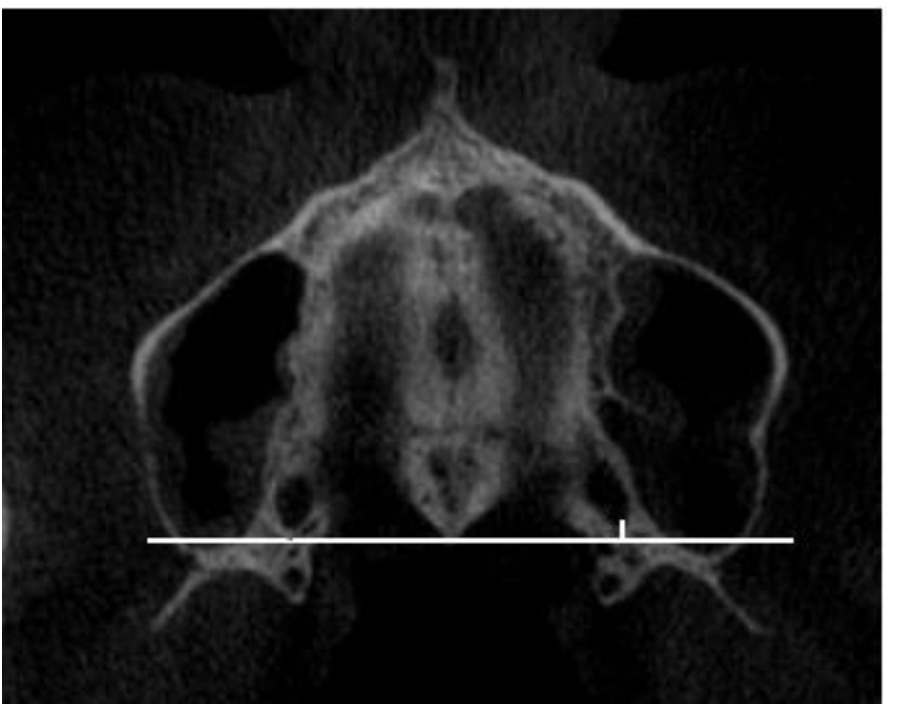

Figure 3. Distance from the greater palatine foramen to the posterior nasal plane.

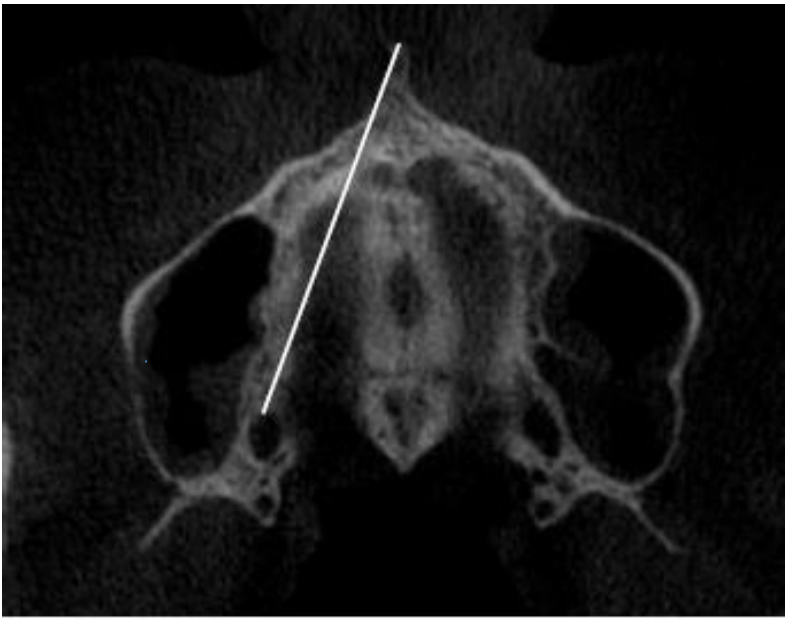

Figure 4. Distance from the greater palatine foramen to the anterior nasal spine.

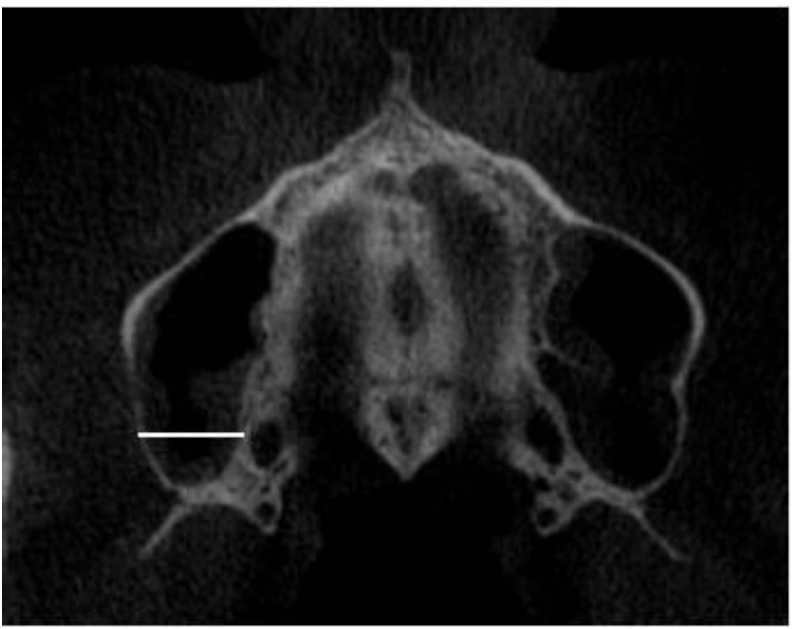

Figure 5. Distance from the greater palatine foramen to the alveolar ridge.

Distance from the greater palatine foramen to the alveolar ridge (Figure 5). Greater palatine foramen distance to the buccal bone plate has a range between 5-19.75 mm [17].

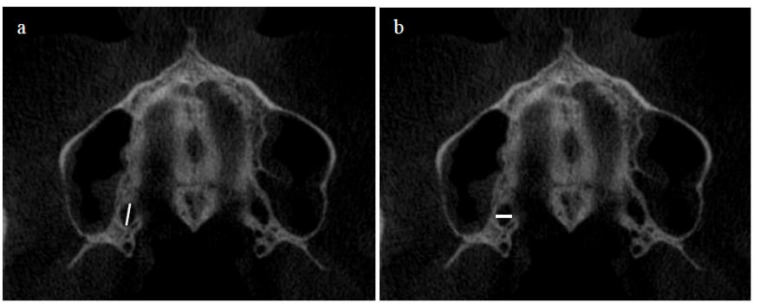

Figure 6. Diameters of the greater palatine foramen: a) anterior-posterior diameter and b) tranverse diameter.

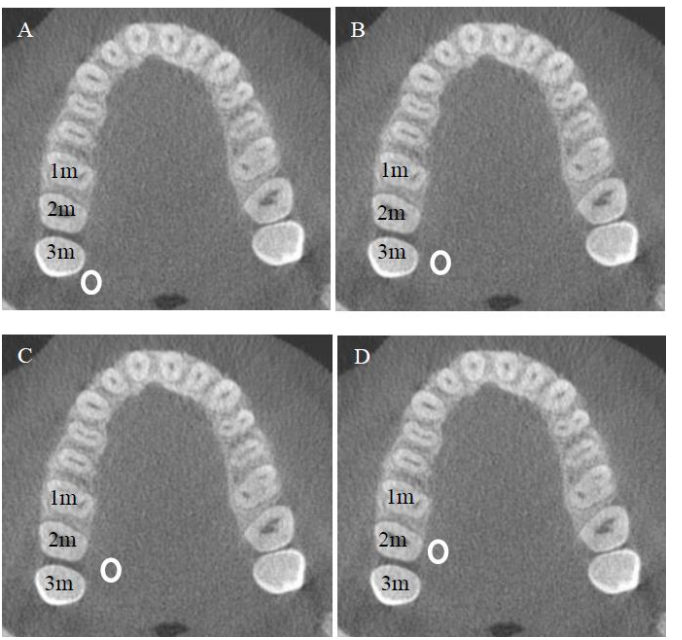

Figure 7. Position of the greater palatine foramen: A) distal to the third molar, B) opposite to the third molar, C) between the third and second molar, and D) opposite to the second molar.

Diameters of the greater palatine foramen: a) anterior posterior diameter, was defined as the distance from the most anterior to posterior point of the foramen; b) transverse diameter, was defined as the distance from the most medial to distal point of the foramen (Figure 6). The anterior-posterior diameter has a range of 3.64-9.46 mm. The transverse diameter has a range of 1-4.50 mm [17].

Regarding the position of the greater palatine foramen with respect to the maxillary molars, the greater palatine foramen is usually located opposite the third maxillary molar.

However, other possible locations of the greater palatine foramen are distal to the third molar, between the third and second molar, and opposite the second maxillary molar (Figure 7) [16, 18, 19].

Morphology of the greater palatine foramen presents different anatomical variations (Figure 8).

Furthermore, in the posterior palatal region, the greater palatine foramen is accompanied by the presence of one or more foramina, through which the lesser palatine nerves emerge on the palate (Figure 9).

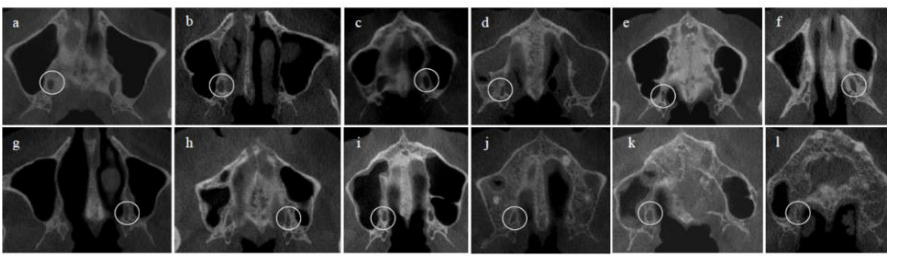

Figure 8. Anatomical variations of the greater palatine foramen in axial slices: a) circular, b) drop of water, c) oval, d) banana, e) eight, f) diamond, g) smoke, h) teardrop, i) kidney, j) triangle, k) crescent, and l) slot.

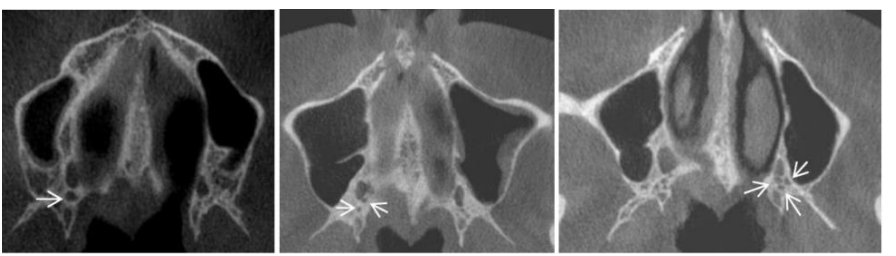

Figure 9. Palatine lesser foramina in axial slices.

Sagittal Slices

Sagittal slices show the anatomy of the greater palatine canal from the lower portion of the pterygopalatine fossa until its emergence on the palate (Figure 10).

To display the union of the greater palatine canal and the pterygopalatine fossa, it is necessary to perform a dynamic vision of the sagittal plane on CBCT (Figure 11).

Greater Palatine Canal Length

The greater palatine canal length has been examined by several CBCT researchers based on different landmarks. Howard et al. [14] were the first authors determining the greater palatine canal length on CBCT images. They established the pterygoid canal as the superior limit of the greater palatine canal and the greater palatine foramen as the inferior limit.

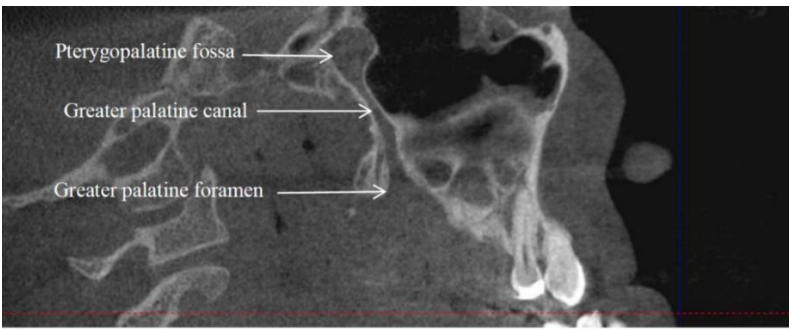

Figure 10. Sagittal image of the pterygopalatine fossa, greater palatine canal and greater palatine foramen.

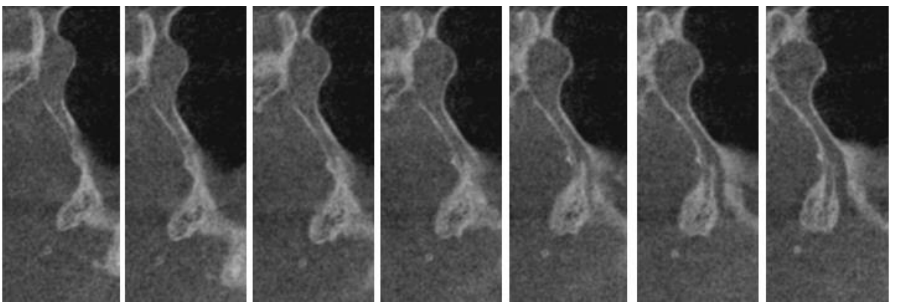

Figure 11. Sagittal slices showing the anatomic communication of the pterygopalatine fossa with the hard palate trough the greater palatine canal.

Sheikhi et al. [15] use the same landmarks to determine the greater palatine canal length.

Sagittal slices allow determining the point where the greater palatine canal flared to the pterygopalatine fossa as the superior limit of the canal. This is another landmark to determine greater palatine canal length. Greater palatine canal length has a range between of 8.06-40 mm [14, 15, 17].

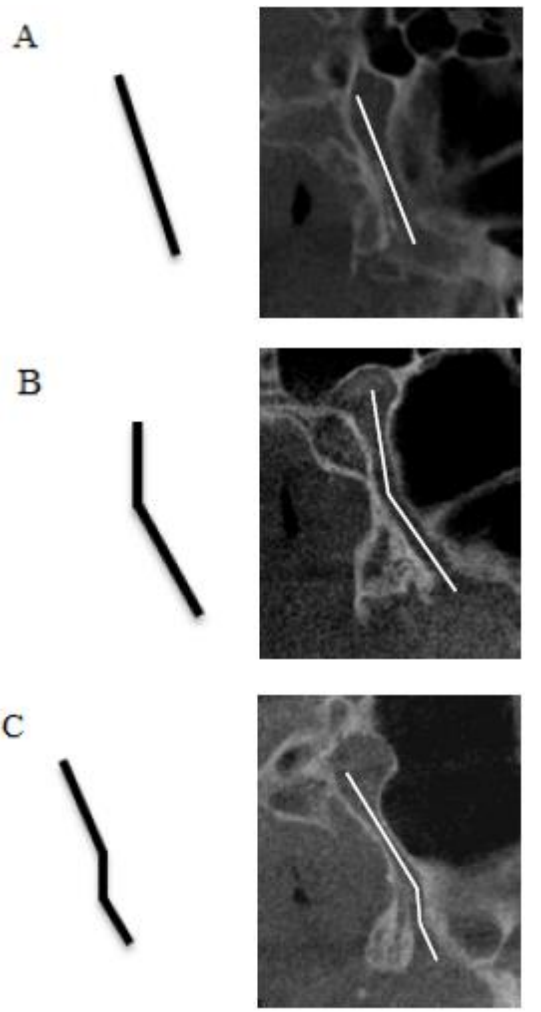

Figure 12. Anatomic routes of the greater palatine canal in sagittal slices: A) anterior-inferior direction, B) inferior and anterior-inferior direction, and C) inferior, anterior-inferior and inferior direction.

Anatomic Routes of the Greater Palatine Canal

The greater palatine canal presents different anatomic routes from the pterygopalatine fossa to the hard palate in sagittal slices (Figure 12) [14, 15]:

- Route anterior-inferior from the pterygopalatine fossa.
- Route with inferior direction, changing to anterior-inferior direction.
- Route with inferior direction, changing firstly to anterior-inferior direction, and finally to inferior direction.

According to the greater palatine foramen morphology, the canal presents different anatomical variations (Figure 13).

Besides, the sagittal slices show the lesser palatine canal through which the lesser palatine nerves emerge on the hard palate (Figure 14).

Coronal Slices

Coronal slices show the anatomy of the greater palatine canal from the lower portion of the pterygopalatine fossa until its emergence on the palate (Figure 15).

Besides, coronal images allow measuring the length of the greater palatine canal.

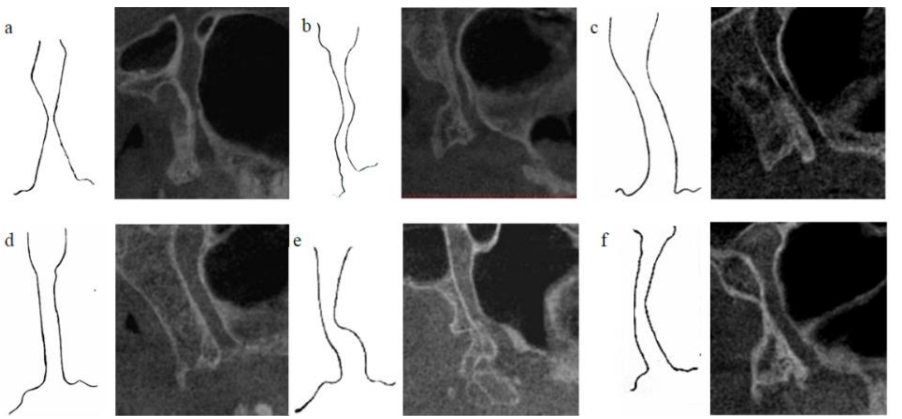

Figure 13. Anatomical variants of the greater palatine canal: a) hourglass, b) "E" shape, c) "ʃ" shape, d) straight, e) waterfall, and f) curve canals.

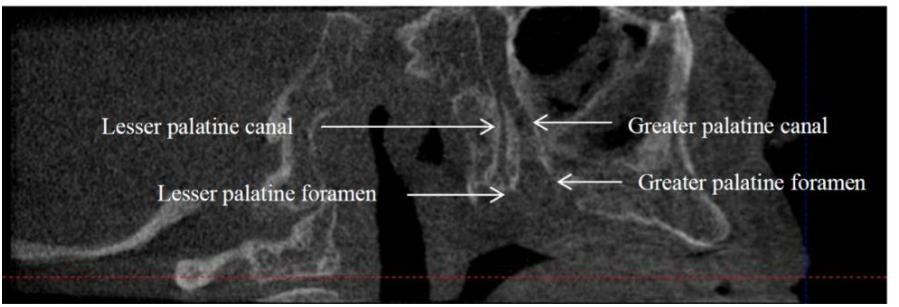

Figure 14. Sagittal image of the greater palatine canal, greater palatine foramen, lesser palatine canal and lesser palatine foramen.

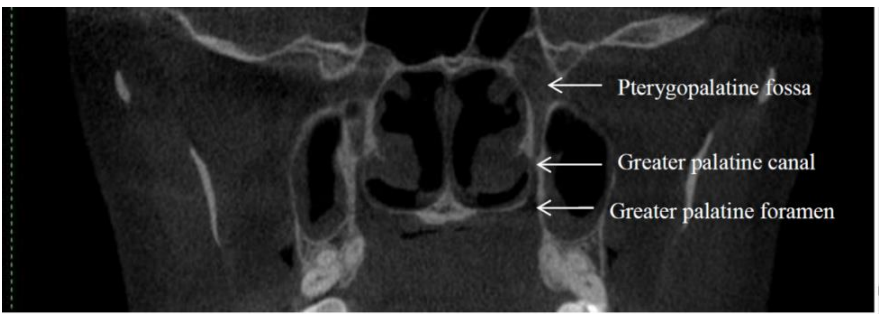

Figure 15. Coronal image of the greater palatine canal, greater palatine foramen, lesser palatine canal and lesser palatine foramen.

Anatomic Routes of the Greater Palatine Canal

The greater palatine canal presents different anatomic routes from the pterygopalatine fossa to the hard palate in coronal slices (Figure 16) [14, 15]:

- Route directed inferiorly from the pterygopalatine fossa.
- Route with inferior-lateral direction, changing to inferior direction.
- Route with inferior-lateral direction changing to inferior-medial direction.
- Route with inferior-lateral direction, changing first to inferior direction, and finally to inferior-medial direction.

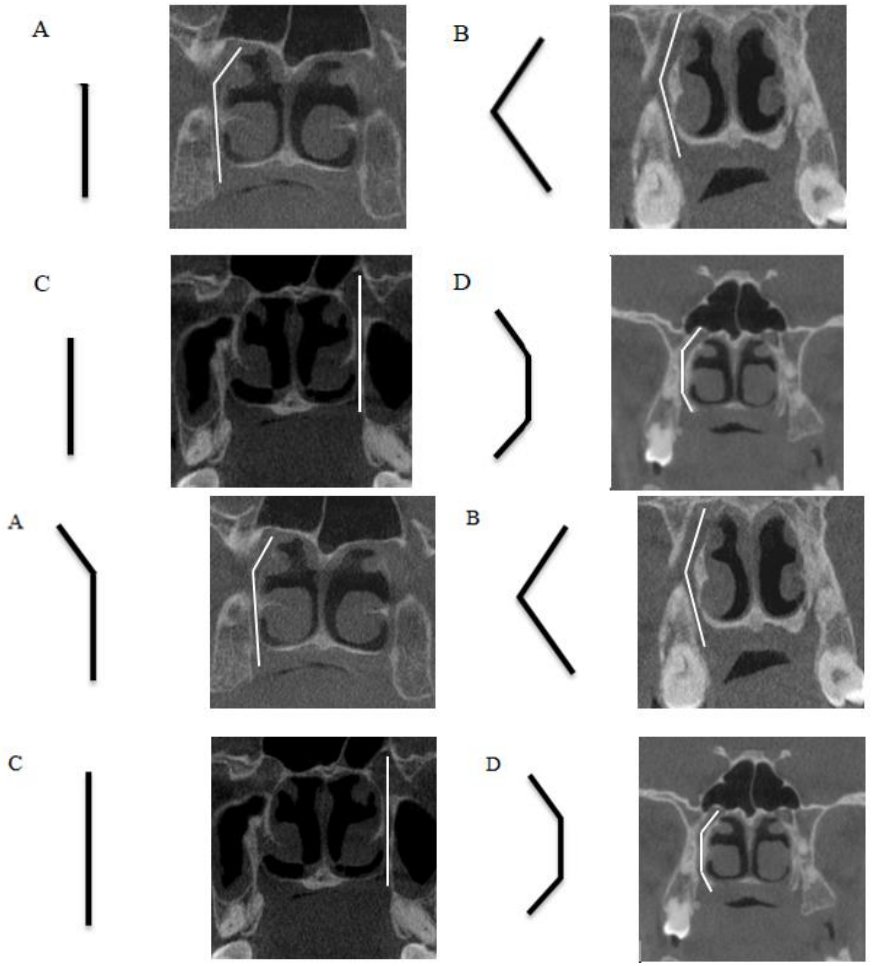

Figure 16. Anatomic routes of the greater palatine canal in coronal slices: A) inferior-lateral and inferior direction, B) inferior-lateral and inferior-medial direction, C) inferior direction, and D) inferior-lateral, inferior and inferior-medial direction.

CLINICAL IMPLICATIONS

An exhaustive knowledge of the greater palatine foramen and greater palatine canal are necessary for dentists, maxillofacial surgeons and otolaryngologists. The position and location of the greater palatine foramen is key to the realization of various therapeutic procedures as follows: dental

treatments (restorative, implants, dental extractions, drain abscesses), periodontal treatments (harvesting sub-epithelial connective tissue grafts), maxillary (orthognathic osteotomy Le Fort, oral maxillofacial syndromes and chronic pain), and nasal (maxillary sinus surgery, septo-rhinoplasty). Anesthesia applied through the greater palatine canal affects the maxillary teeth, palate and gingival tissue, half face skin, nasal cavity and sinuses. Moreover, administration of anesthesia through the greater palatine canal reduces intraoperative bleeding during endoscopic sinuses surgery and septo-rhinoplasty, and allows better control of the posterior epistaxis [9].

A detailed anatomic description of the greater palatine canal is necessary to avoid clinical complications derived from the technique of maxillary nerve block. These complications include diplopia, strabismus, ptosis, intravascular injection, anesthesia into the nasopharynx, damage to neural tissue, pterygopalatine fossa and/or infratemporal abscess, meningitis and anesthetic failure [8, 10].

In this sense, is very important to know the anatomical variations of the greater palatine foramen and greater palatine canal for anesthetic planning of different dental and/or surgical treatments. The bone morphology of these structures could be a limiting factor in access to the pterygopalatine fossa and, therefore maxillary nerve block.

REFERENCES

[1] Rouviére H., Delmas A. Anatomie humaine. Descriptive, topographique et fonctionnelle. Tête et cou. París: Masson; 2002.

[2] Testut L., Latarjet A. Traité d'anatomie humaine. Ostéologie, arthrologie, myologie. París: Octave Doin; 1899.

[3] Drake R. L., Vogl W., Mitchell A. W. M. Gray's Anatomy for Students. Philadelphia: Churchill Livingstone; 2005.

[4] Henderson S. J., Derart D. A. Anatomy for Students of Dentistry. Edinburgh: Churchill Livingstone; 1978.

[5] Lang J. Clinical Anatomy of the Nose, Nasal Cavity and Paranasal Sinuses. New York: Thieme Medical Publishers; 1989.

[6] Chen C. C., Chen Z. X., Yang X. D., Zheng J. W., Li Z. P., Huang F., Kong F. Z., Zhang C. S. Comparative research of the thin transverse sectional anatomy and the multislice spiral CT on pterygopalatine fossa. *Turk. Neurosurg.*, 2010; 20:151 – 8.

[7] Suárez N. C., Gil-Carcedo G. L. M., Marco A. J., Medina E. J., Ortega del Alamo P., Trinidad P. J. Tratado de Otorrinolaringología y Cirugía de Cabeza y Cuello. Buenos Aires: Médica Panamericana; 2007.

[8] Das S., Kim D., Cannon T. Y., Ebert C. S. Jr., Senior B. A. High-resolution computed tomography analysis of the greater palatine canal. *Am. J. Rhinol*., 2006; 20:603 – 8.

[9] Douglas R., Wormald P. J. Pterygopalatine fossa infiltration through the greater palatine foramen: where to bend the needle. *Laryngoscope,* 2006; 116:1255 – 7.

[10] McKinney K. A., Stadler M. E., Wong Y. T., Shah R. N., Rose A. S., Zdanski C. J., Ebert C. S. Jr., Wheless S. A., Senior B. A., Drake A. F., Zanation A. M. Transpalatal greater palatine canal injection: Radioanatomic analysis of where to bend the needle for pediatric sinus surgery. *Am. J. Rhinol. Allergy,* 2010; 24:385 – 8.

[11] Hwang S. H., Seo J. H., Joo Y. H., Kim B. G., Cho J. H., Kang J. M. An anatomic study using three-dimensional reconstruction for pterygopalatine fossa infiltration via the greater palatine canal. *Clin. Anat.*, 2011; 24:576 – 82.

[12] Kang S. H., Byun I. Y., Kim J. H., Park H. K., Kim M. K. Three-dimensional analysis of maxillary anatomic landmarks for greater palatine nerve block anesthesia. *J. Craniofac. Surg.,* 2012; 23:e199 - 202.

[13] Tomaszewska I. M., Tomaszewski K. A., Kmiotek E. K., Pena I. Z., Urbanik A., Nowakowski M., Walocha J. A. Anatomical landmarks for the localization of the greater palatine foramen–a study of 1200 head CTs, 150 dry skulls, systematic review of literature and meta-analysis. *J. Anat.*, 2014; 225:419 – 35.

[14] Howard-Swirzinski K., Edwards P. C., Saini T. S., Norton N. S. Length and geometric patterns of the greater palatine canal observed in cone beam computed tomography. *Int. J. Dent.,* 2010; doi:10.1155/2010/ 292753.

[15] Sheikhi M., Zamaninaser A., Jalalian F. Length and anatomic routes of the greater palatine canal as observed by cone beam computed tomography. *Dent. Res. J. (Isfahan),* 2013; 10:155 – 61.

[16] Ikuta C. R., Cardoso C. L., Ferreira-Júnior O., Pereira Lauris J. R., Souza P. H., Rubira-Bullen I. R. Position of the greater palatine foramen: an anatomical study through cone beam computed tomography images. *Surg. Radiol. Anat.*, 2013; 35:837 – 42.

[17] Rapado-González O., Suárez-Quintanilla J. A., Otero-Cepeda X. L., Fernández-Alonso A., Suárez-Cunqueiro M. M. Morphometric study of the greater palatine canal: cone-beam computed tomography. *Surg. Radiol. Anat.,* 2015; doi:10.1007/s00276-015-1511-y.

[18] Yilmaz H. G., Boke F., Ayali A. Cone-beam computed tomography evaluation of the soft tissue thickness and greater palatine foramen location in the palate. *J. Clin. Periodontol.*, 2015; 42:458 – 61.

[19] Aoun G., Nasseh I., Sokhn S., Saadeh M. Analysis of the greater palatine foramen in a Lebanese population using cone-beam computed tomography technology. *J. Int. Soc. Prev. Community Dent*., 2015; 5(Suppl. 2):S82 – 8.

In: Computed Tomography
Editor: Deborah Carter
ISBN: 978-1-53610-766-1

Chapter 5

USING HIGH RESOLUTION COMPUTED TOMOGRAPHY IMAGES TO ASSESS THE RISKS OF PATHOLOGICAL CHANGE OF PULMONARY PARENCHYMA

Hongyang Jiang, He Ma* and Mengdi Gao
Sino-Dutch Biomedical and Information Engineering School,
Northeastern University, Shenyang, China

ABSTRACT

Lung cancer is one of the most concerned diseases around the world. Generally, its mortality is very high because the malignant tissue of lung cannot be checked out timely. Once cancerous cells in pulmonary parenchyma are detected in the early stage, the cure rate can be enhanced. A large collection of high resolution computed tomography (CT) images and their diagnostic information make it possible to analyze a new suspected case based on these historical data using data mining technologies. Although lung CT images provide us much valuable pathological information about cancerization, it is tough to extract and utilize it directly due to its irregularity in content. Thus, applying the current content based image retrieval (CBIR) schemes to assess a medical image can produce an exciting and promising effect. In this chapter, we

* Corresponding author email: mahe@bmie.neu.edu.cn

will review and discuss the application of the state-of-art CBIR schemes in pathological risk analysis of lung CT images.

Keywords: pulmonary parenchyma, high resolution computed tomography, content based image retrieval, risk analysis

INTRODUCTION

With the development of the medical imaging techniques, a large amount of high-quality computed tomography (CT) images accumulated a lot, which contained much precious pathological information. For most of cancers, especially the lung cancer that is the most fatal cancer in the world [1], necessary medical treatment may greatly prolong one's life if the patient can obtain precautions and early therapy. In most cases, late therapeutic process may torment the patient's body and spirit. Serious end-stage lung disease is incurable not only because of the undeveloped medical technology but also the great economic costs on therapy. To some extent, it is insignificant for the latent patients to merely detect the disease when they felt unwell, because they may possibly miss the best treatment period. The main focus for the researchers should be seeking some methods that can make some early warning about patients' hidden healthy crisis with the help of abundant medical pathological data. In this case, imperative precautions about lethal factors of the lung cancer are extremely imminently. Compared with the past, present medical data are plentiful, including literal information, graphic information and video information, which provide challenges and opportunities for researchers to explore significant physical rules and then to help sub-healthy people against latent diseases. CT imaging technology developed fast and was applied to lesion detection in different parts of human body, especially in the lung. Actually lung CT images reflect the health condition of the whole pulmonary, but radiologists can hardly interpret it roundly. In this situation, the computer played an important role to help them to solve this problem. Many scholars have designed image retrieval systems based on the image's content by means of computer's strong calculation and analysis abilities [2]. The content based medical image retrieval system (CBMIRS) can compensate human's deficiencies, which is proved to be a useful computer aided diagnosis (CAD) system [3].

As medical imaging skills developed and the CAD technology improved, more and more superb images and precise locations of lesion are accumulated

and depicted. In the Meantime, advanced picture archiving and communication systems (PACS) are built in some hospitals [4]. Associated with the other two systems, Hospital Information Systems (HIS) and Radiology Information Systems (RIS), PACS is mainly used to obtain, transmit, preserve and display medical images under the DICOM standard [5]. Although some valuable information is indeed contained in those medical images, we do not know how to take advantage of it adequately. In recent years, there are many researchers focusing on information and image retrieval based on the textual record, the image content or both of them [6]. Generally, textual records are written by doctors and only reflect their unilateral viewpoints of diagnosis. However, the image content has multiple perspectives, which is difficultly illustrated by only one person.

Researchers have focused on mainly two kinds of retrieval ways. One way is using vision image form to make the correlation analysis, which is known as the query-by-visual-example (QBVE) [7], and the other way is to retrieve images by semantic content, which is named as semantic retrieval [8]. Through validation by other researchers, vision similarity alone can hardly reflect real correlations [9]. Moreover, complex and deep semantic retrieval is still required to realize and develop. Presently scholars have proposed some effective medical image retrieval systems, such as Image Yale Image Finder (YIF), Retrieval for Medical Application (IRMA) and iMedline [10]. Through analyzing both the vision similarity and semantic relevance, these systems can seek out the optimal image we want. However, other experiments also showed that the lung nodule detection can be implemented through viewing conventional film or videotaped helical CT images [11]. During past several years, researchers have always been working on clinical problems, such as lesion detection and disease assessment [12, 13]. At the same time, some scholars have already made risk prediction about breast cancer pathology by analyzing image content [14, 15]. It is certain that abundant unaware information may be found with the help of progressive detecting methods. According to subjects' habits, environment and heredity, researchers may conclude the risk factors of pulmonary diseases [16], but few of them focus on the early pathological phenomena of pulmonary. In this chapter, detailed diagnostic information about the pulmonary parenchyma is provided by the radiologists. The method designed by this chapter can sum up correlation of tissue structures among pulmonary images.

IMAGE PREPARATION AND RETRIEVAL SYSTEM

Data Set

CBIR systems need us to prepare image data that contain details of characteristics made by specialists, so we can validate the CBIR systems' performance. A total of 115 patients' clinical lung CT images with specific pathological diagnostic information were supplied by Guangdong medical college. Among these patients, there were 49 females and 66 males and the youngest and oldest of them was 39 and 85 years old, respectively. A return visit was completed for each patient and 27 of the patients died or suffered from recidivation, which can be considered as persuasive labels of malignancy of lung cancer. Among these lung CT images, nine pathological characteristics about the lung were diagnosed, including lobulation, density, periphery symptom, relation to pleura, gene RRM1 level, gene ERCC1 level, anaplastic lymphoma kinase (ALK), immunohistochemical (SABC) gene ERCC1, and cancer pathology. Before we analyzed these characteristics of pulmonary parenchyma tissues, several steps of image preprocessing should be taken.

Pulmonary Parenchyma Segmentation

The content of provided lung CT images almost including equipment, clothes, thoracic tissues and other systematic noises outside the pulmonary parenchyma, were not inappropriate to make analysis. To make these lung CT images suitable for big data processing, a fast and efficient lung content cutting method was designed, which is displayed in Figure 1. All the lung CT images were processed in five steps. First, global maximum between-class variance (OTSU) method was executed for classifying the raw lung image into two classes: the white part and the black part [17]. Second, considering peculiarities of pulmonary morphology, this system adopted a self-adaptive disc to eliminate noise in the whole images, such as impulses and bubbles. Third, pulmonary contour was recognized through analyzing the relative position information between the thorax and lung. Fourth, by combining both of the erosion and dilation operators based on 8-connected region standard, this study eliminated the esophagus between the two pulmonary lobes and smooth the contours of pulmonary lobes. Finally, the whole lung content was segmented. Through reverse enhancement, which can make gray images linearly inverted within the gray level range, we obtained a quite obvious pulmonary parenchyma.

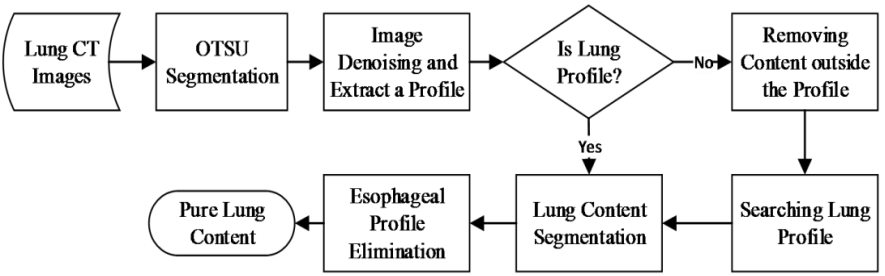

Figure 1. Pulmonary parenchyma segmentation flow chart.

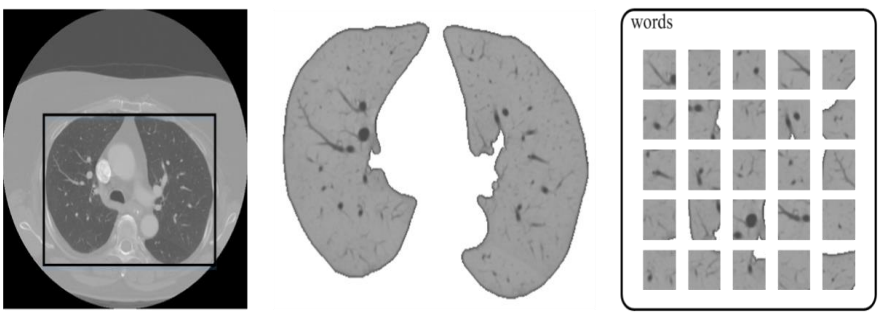

Figure 2. Lung CT images processing performance: from original images to image words.

Interference and noises outside of the lung content can be seen clearly from the original lung CT image (Figure 2. (a)). After processing the original pulmonary image, the whole pulmonary parenchyma is segmented, which is shown in Figure 2. (b).

Feature Selection and Vocabulary Construction

Analyzing the content of images based on patches [18], this system designed a rectangle of $N \times N$ pixels. The rectangle is just a standard sliding window which is used to extract image words (Figure 2. (c)). The definition of a word is explained as follows:

Definition 1: There is a hypothetical image space $I \in R^2$, where I has the size of $x \times y$ pixels, if there is another image space $w \in R^2$ and w is part of I

($w \in I$), where w is signified as $l \times l$ pixels ($l < x$ & $l < y$), then w is named as a word.

Using the standard sliding window created by this system, each lung content image was sampled. To avoid omitting any parts of the pulmonary parenchyma, this system set half of the word length as the sampling step length. As the word length used in this study was 32 pixels, so the sampling step was set as 16 pixels. Besides, the sampling window moved in vertical or horizontal direction during image words collection. However, a very small step length was inadvisable as the huge amount of blocks greatly aggravate the computational burden. This study also designed a word selection criterion, that is, any word whose pixels contain more than 90% pulmonary pixels was regarded as a valid word. Hence, each lung CT image can consist of a group of valid words. After word selection from the original image data, a large number of words were generated and can be taken as a corpus that contained most all the fragments of lung content. Generally, the corpus was so big that it will cost much time to analyze an unknown image. This study refined a vocabulary from the corpus for improving the image analysis ability. The definition of a vocabulary is as follows:

Definition 2: There exists a hypothetical word set V that contains K words, if these K words are obviously different from each other and any other word can belong to one of them, then V is addressed as a vocabulary and K is the size of the vocabulary.

To generate the image word and vocabulary, the system took two steps: word feature selection and vocabulary construction. Generally, texture features play an important role in expressing pixels tissues within an image. This system synthesized diverse texture features, including the gray level co-occurrence matrix (GLCM), Tamura features and the rotation invariant local binary pattern (riLBP), which were proposed by previous scholars, to represent each image word. GLCM is a gray level spatial dependence matrix, which reflects spatial relationship of pixels using statistical methods. The element (X, Y) of GLCM signified the number of times that a pixel of value X had a specific location relationship with a pixel of value Y [19]. After generation of the GLCM, correlation, contrast, homogeneity, entropy and energy can be calculated. Tamura feature is another famous texture feature that is defined and depicted by Tamura et al. in 1978 on the basis of human visual perception [20]. It contains toughness, regularity, contrast, coarseness, directionality and line-likeness. What's more, LBP is a straightforward and effective texture descriptor that shows a central pixel's neighboring pixels using the simple comparison operator [21]. In this system p_1, p_2, …, p_8 represent eight pixels

around the central pixel p_c. Through comparison between p_c and p_i ($i = 1,...,8$) which are shown in Equ.(1) and (2), we can obtain a binary number of eight-bits. Thus every pixel has a LBP code.

$$C_{LBP} = \sum_{i=1}^{8} f(p_i - p_c) \cdot 2^{i-1} \tag{1}$$

$$f(a) = \begin{cases} 1 & (a \geq 0) \\ 0 & (a < 0) \end{cases} \tag{2}$$

To reduce the complexity LBP encoding, this system adopted the rotation invariance local binary pattern (riLBP), that any code of LBP and its rotated codes can be seen as the same code. Through riLBP encoding, 34 different binary numbers were generated. In consequence, the rotation invariance histogram of riLBP codes was drawn and can be used to express an image. After finishing different kinds of texture features extraction, each image word can be denoted as a *1* by *M* feature vectors and *M* represented the number of texture feature values.

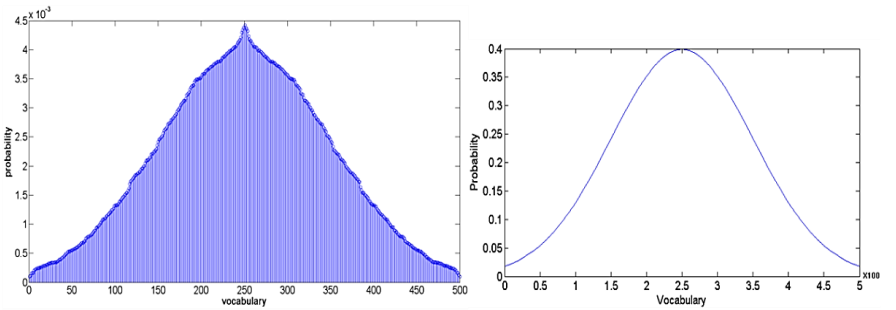

(a) Vocabulary distribution (b) Standard normal distribution

Figure 3. Vocabulary distribution of the image words extracted from original lung CT images based on fixed clustering start points K-means algorithm. (a) is the vocabulary distribution of this study and (b) is the standard normal distribution.

To avoid the heterogeneity and irregularity of vocabulary, this study improved K-means cluster method through fixing the clustering start points in advance. During the generation of vocabulary, the center points of K-means adjusted in a limited spatial position automatically [22]. As literary words are approximate to normal distribution, this chapter tried to construct an image word distribution with a very similar standard normal distribution (Figure

3.(b)). The experiment demonstrated that method of uniformly distributing cluster start points in a specific range can acquire a good approximation (Figure 3.(a)).

LDA Model for Image Retrieval and Analysis

In this system, an advanced probabilistic topic model named latent Dirichlet allocation (LDA) was used for analyzing the content of lung CT images. The LDA model can be interpreted as a kind of three-level hierarchical Bayesian model that has already been utilized in web text classification, document modeling and collaborative filtering [23, 24]. Through ceaseless development and research, the LDA model acquired very good performance in these fields and can expand into medical image analysis. As the characteristics of pulmonary parenchyma have been provided by radiologists, thus these characteristics can be considered as themes of lung content and each pulmonary image had its own distribution of themes. Based on their theme distributions, the correlation between any two images can be analyzed.

After the decomposition of each image into image words, the basic elements of LDA model were ready. In this system, LDA consisted of three important components: image word (sub-image with $N \times N$ pixels), the pulmonary image, and the topic (characteristic of pulmonary parenchyma). In this study, there are hypotheses that the image word was expressed by w_i, ($i \in \{1, 2, \ldots, V\}$); V is the number of words in the vocabulary, which was preset according to the size of the corpus; the pulmonary image was expressed by $P=\{ w_1, w_2, \ldots, w_N\}$, which was a group of N image words; the image corpus was expressed by $C=\{P_1, P_2, \ldots, P_M\}$, where M is the number of pulmonary images in the corpus. Additionally, we also took symbol z to represent the topic, which can be beneficial to latter discussion. The topic number is an important parameter influencing the results of the system. However, it does not have a fixed optimum value and needs to be modulated in accordance with different data set.

Evolved from probabilistic latent semantic analysis (PLSA) and latent semantic indexing (LSI), LDA has a strong summarizing ability [25]. In LDA model of this system, original pulmonary images can be considered as the image corpus and every pulmonary image was taken as a group of image words with some special meanings in it. In addition, the group of image words of each pulmonary contained random image topic mixtures, where every topic

also had a random collection of image words [26]. In other words, image word layer, pulmonary image layer and image topic layer constituted the whole LDA model.

The details of generative process of one random pulmonary image in the image corpus are illustrated in follow three steps:

1. Randomly choose the size of an image $N \sim \text{Poisson}(e)$
2. Randomly choose the number of topics $T \sim \text{Dir}(\alpha)$
3. Randomly choose each of the N image words w_i in the pulmonary image:
   (a) Choose a topic $z_i \sim \text{Multinomial}(T)$
   (b) Choose an image word w_n according to the probability $p(w_i|z_i,b)$ that is a polynomial conditional probability.

To utilize the LDA model, parameter initialization is required, including setting the number of words in the vocabulary (K) and the number of topics (T). Both of them construct a matrix β of $K \times T$ size and any element in β is represented by $\beta_{ij} = p(w_j = 1|z_i = 1)$. The value of β can be inferred through multi-iterations as discussed later. The probability density function of K-dimensional Dirichlet variable θ on (K-*1*) simplex function is displayed in Equ.(3):

$$p(\theta \mid \alpha) = \frac{\Gamma(\sum_{i=1}^{k} \alpha_i)\delta y}{\prod_{i=1}^{k} \Gamma(\alpha_i)} \theta_1^{\alpha_1 - 1} \cdots \theta_k^{\alpha_k - 1} \tag{3}$$

where the $\Gamma(x)$ is a Gamma function of multiple parameters and has a K-dimension parameter vector $\alpha=\{\alpha_1, \alpha_2, \ldots, \alpha_K\}(\alpha_i > 0)$. The parameters α will also be figured out through estimation algorithms. The joint distribution of prior parameter θ, image topic z and image word w are shown as follows:

$$p(\theta, z, w \mid \alpha, \beta) = p(\theta \mid \alpha) \cdot p(z_N, w \mid \alpha, \beta, \theta) \tag{4}$$

$$p(z_N, w \mid \alpha, \beta, \theta) = \prod_{n=1}^{N} p(z_n \mid \theta)\, p(w_n \mid z_n, \beta) \tag{5}$$

Then the conditional probability of a image $p(w|\alpha, \beta)$ can be expressed as Equ.(6):

$$p(w|\alpha,\beta)=\int\sum_{z_N}p(\theta,z_N,w|\alpha,\beta)d\theta \tag{6}$$

Finally, the conditional probability of the image corpus $p(C|\alpha, \beta)$ can be acquired in Equ.(7):

$$p(C|\alpha,\beta)=\prod_{d=1}^{M}\int p(\theta_d|\alpha)\left(\sum_{z_N}p(z_N,w|\alpha,\beta,\theta_d)\right)d\theta_d \tag{7}$$

Above are some probability functions that explained the generative process of an image on the basis of the LDA model. To adequately take advantage of LDA model for image analysis, reasonable parameters should be correctly estimated. As mentioned above, α was K dimensions parameters of Dirichlet function and the matrix β was the parameter combination of vector $\varphi_k(k\in[1,K])$ and b which is the parameter vector of φ_k. According to previous experiments and experience, the values of parameters α and b can be set in the beginning of running the LDA model. The primary task of us is to compute parameters z_n, θ_d and φ_k by iterating a series of probability functions for deducing topic distribution on each pulmonary image. Blei D M et al. used (expectation maximization) EM algorithm to search for a group of parameters z_n, θ_d and φ_k that can make the LDA model robust and efficient [26]. However, this system instead adopted Gibbs sampling that was validated to contribute to quickly approaching optimal parameters [27]. Based on the Gibbs sampling criterion, the topic distribution of an image corpus was generated through above functions:

$$p(z_i=k|z_{-i},w)=\hat{\theta}_{mk}\cdot\hat{\varphi}_{kt} \tag{8}$$

where,

$$\hat{\theta}_{mk}=\frac{n^{(k)}{}_{m,-i}+\alpha_k}{\sum_{k=1}^{K}(n^{(k)}{}_{m,-i}+\alpha_k)} \tag{9}$$

$$\hat{\varphi}_{kt} = \frac{n^{(t)}_{k,-i} + b_k}{\sum_{t=1}^{V}(n^{(t)}_{k,-i} + b_k)} \tag{10}$$

Finally, we can obtain the topic distribution of any pulmonary image by analyzing the image words it contained. Then a pulmonary image can be expressed as a topic vector $P_\theta=\{\theta_1, \theta_2, \ldots, \theta_T\}$, where θ_i is the probability of topic i of this pulmonary image and T is the number of topics. To figure out the correlation between two images, a distance measurement method, Kullback-Leibler Divergence (KLD), was used in this system [28]. The computational formula of KLD is shown as follows:

$$D_{KLD}(x \| y) = \sum_{t=1}^{T} p_t(\log_2 p_t - \log_2 q_t) \tag{11}$$

$$x = \{p_1, p_2, \ldots, p_T\} \tag{12}$$

$$y = \{q_1, q_2, \ldots, q_T\} \tag{13}$$

EXPERIMENTAL RESULTS

Unlike general pictures, lung CT images do not have very clear features that can be easily recognized by naked eyes. By feat of the LDA image retrieval system (LDAIRS), we can make image correlation analysis between any two images. Thus we can retrieve similar images according to their correlations. Using statistical method to analyze the retrieval results, we can make risk assessments and early precautions on a patient's lung disease. Predictions can be made using statistical analysis method. The retrieval results of LDAIRS were measured with precision and recall, the formulas of which are expressed as Equ. (13) and (14).

$$P = \frac{number\ of\ correct\ feedback\ images}{number\ of\ feedback\ images} \times 100 \tag{13}$$

$$R = \frac{number\ of\ correct\ feedback\ images}{number\ of\ entire\ correct\ images} \times 100 \tag{14}$$

where P and R represent the precision rate and recall rate, respectively.

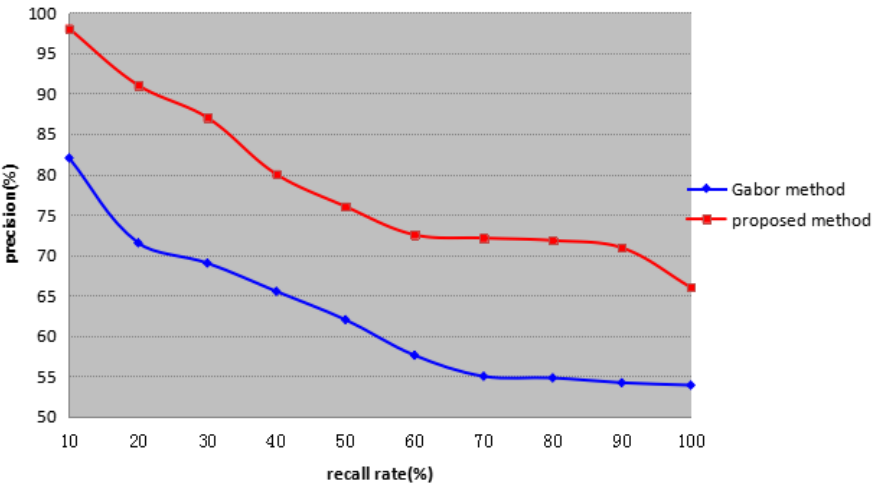

Figure 4. Precision and recall curve between proposed method and Gabor based retrieval method.

This chapter validated the performance of LDAIRS using 345 pulmonary images equally selected from 115 patients. As the number of pulmonary images with detailed diagnostic was very limited, so the leave one out cross validation method was executed. To illustrate the image retrieval ability of LDAIRS, this chapter made a comparison between this method and the global Gabor features based retrieval method (Figure 4) [29]. The results displayed that the LDAIRS obviously outperform the Gabor based method on medical image retrieval. As it was mentioned above, every pulmonary image was diagnosed on nine pathological characteristics. Each characteristic of pulmonary can be seen as a searching target label. The optimum retrieval results were that all the characteristics of feedback images were equal to those of the target pulmonary. In this chapter, we conclude two kinds of retrieval results. First, if all the characteristics of the feedback images were equal to those of the target image, these feedback images were regarded as the global matching images which can be also called an identical tissues here. Second, if

partial characteristics of feedback images were equal to those of the target image, a feedback image was the local matching image which was also called a similar tissue.

The LDAIRS can summarize the latent correlation among the images through multiple iterations without requiring supervised information. To start the LDAIRS, we first initialized the number of words in the vocabulary (*K*) and the number of topics (*T*). The values of *K* and *T* need to be preset based on both of the characteristic and size of the data set. Using the same values of *T* and *K*, this study repeatedly tested the effectiveness of random words distribution and normal words distribution with uniform clustering center points. Through retrieving 50 pulmonary images according to a target pulmonary image, we obtained the retrieval results in Table 1. The average retrieval accuracy of random word distribution was 0.63±0.06 and that of normal word distribution was 0.70±0.03. This experimental results demonstrated that normal distribution were more appropriate for describing pulmonary image words.

LDAIRS was adept in summarizing characteristics of pulmonary parenchyma. To demonstrate the retrieval performance of LDAIRS on different pulmonary characteristics, this chapter conducted ten times experiments to analyze the characteristics of a random selected pulmonary image. This experiment can be divided into five steps. First, the target pulmonary image was decomposed into image words. Second, the topic distribution of the whole image words was renewed by LDAIRS. Third, each pulmonary image was defined by a topic vector, including the target pulmonary image. Fourth, the relevance ranking between the target pulmonary image and each pulmonary image in the image corpus was listed. In the end, results of the target pulmonary image's characteristics were given by statistical analysis. Through assessing the top 100 correlated images, we obtained the prediction results which are displayed in Table 2. It is obvious that the retrieval accuracy of similar tissues outperformed that of identical tissue. From the retrieval results, we can make an assessment that how the characteristics of an unknown pulmonary image are. The characteristic among the retrieval results that had the biggest ratio can be considered as the predictive characteristic of the target pulmonary image. In Table 2, the minimum probability value of characteristic (squamous carcinoma) is 0.78 ± 0.04 and the maximum probability value of characteristic (ALK without mutation) is 0.98 ± 0.01. Moreover, all characteristics of the target pulmonary image can be given probability values, which can be seen as the significant reference for

radiologists. Hence, near-term morbidity of disease about lung can also be evaluated by experts.

Table 1. Retrieval results of random words distribution and normal words distribution

No. of test	Topic	Vocabulary Size	Random words distribution		Normal words distribution	
			Right	Wrong	Right	Wrong
1	5	400	32	18	34	16
2	5	500	34	16	37	13
3	5	700	29	21	35	15
4	5	800	30	20	34	16
5	10	500	27	23	36	15
6	10	600	36	14	38	12
7	10	900	33	17	35	15
8	15	300	34	16	33	17
9	15	600	30	20	35	14
10	15	700	29	21	35	15

Table 2. Performance of retrieval results of each characteristic

Characteristics of test image	Same characteristics	Standard deviation
Lobulation	0.90	0.02
Density	0.85	0.05
Periphery	0.86	0.03
Pleural	0.87	0.04
RRM1	0.86	0.03
ERCC1	0.88	0.04
ALK	0.98	0.01
ERCC1	0.86	0.02
Cancer	0.78	0.04
Identical tissue	0.76	0.03

DISCUSSION

Based on the idea of CBIR system, LDAIRS was first used for evaluating the pathological changes of pulmonary parenchyma. Much significant

information was contained in lung CT images. Each pulmonary image in the image corpus had diagnostic information about the characteristics of the lung. In LDAIRS, the LDA model was generated just based on the original pulmonary without using diagnostic information. The topic distribution of each image words was constructed and the correlation between each pulmonary image was created. Parameters in the system played an important role to improve the predictive ability of our system. By adjusting the parameter *K* and *T*, the retrieval effectiveness of different situation can be shown in Table 3. However, the selection of optimal parameters *K* and *T* were heuristic. According to experiments and the peculiarity of our image corpus, the optimum parameters can be achieved.

Table 2. Performance of different groups of parameters

Vocabulary Size	5 topics	10 topics	15 topics
200	0.50 ± 0.07	0.55 ± 0.04	0.48 ± 0.07
300	0.53 ± 0.08	0.59 ± 0.06	0.52 ± 0.02
400	0.55 ± 0.04	0.72 ± 0.01	0.62 ± 0.06
500	0.59 ± 0.06	0.72 ± 0.08	0.64 ± 0.03
600	0.66 ± 0.03	0.76 ± 0.03	0.72 ± 0.07
700	0.67 ± 0.03	0.69 ± 0.05	0.67 ± 0.09
800	0.64 ± 0.02	0.73 ± 0.04	0.70 ± 0.02
900	0.68 ± 0.05	0.77 ± 0.05	0.68 ± 0.03
1000	0.71 ± 0.03	0.73 ± 0.10	0.59 ± 0.08

Checking the diagnostic information provided by radiologists, we understood that pulmonary images had nine pathological characteristics. Hypothetically the possible optimum number of topics (*T*) was nine. The number of image words cropped from the entire image corpus was approximately 42000. In the circumstances, we assumed that the vocabulary sizes were multiples of one hundred words, including numbers from 200 to 1000, that is, nine different sizes of vocabulary. This chapter tested different groups of parameters (*K* and *T*) on this image corpus, which is displayed in Table 3. The results demonstrated that the average retrieval accuracy of 10 topics (0.69 ± 0.07) was better than that of 15 topics (0.61 ± 0.09) and that of 5 topics (0.62 ± 0.07). Moreover, choosing 10 topics in LDAIRS, the retrieval accuracy of 600 words and 900 words were 0.76 ± 0.03 and 0.77 ± 0.05, which were much better than others. Considering the computation cost both 600

words and 900 words, this chapter took 600 words and 10 topics as the optimal parameters.

It was known that more topics can increase the categories in the image corpus. In the same time, so many topics may cause coercive categorizing, which may break the strong correlation among some the pulmonary images. As was illustrated in Table 3, when the number of topics was set to 15, the retrieval performance was worse than that of 10 topics. This phenomenon was called over-categorization, which was still a challenging problem for researchers [30]. Different medical image corpus may have different special characters, so we need to approximate the perfect parameters with the help of the specific problem and professional knowledge. As a consequence, with the provided lung CT images, 10 topics and 600 words were the more suitable parameters.

CONCLUSION

The chapter introduces a novel LDAIRS for medical image retrieval and pathological analysis. To give a pertinent assessment on the status of pulmonary parenchyma, pathological changes of pulmonary parenchyma on different characteristics are the crucial indicators. Focusing on these pathological characteristics, the proposed LDAIRS can provide meaningful analysis about the tissue characteristic of pulmonary parenchyma. In LDAIRS, the number of words in the vocabulary and the number of topics are important parameters, which should be set depending on the size of used corpus. By means of LDAIRS, radiologists may easily do diagnosis without reducing accuracy. Combined with some deep learning technologies, such as convolutional neutral network (CNN), the LDAIRS may acquire more promising performance of risk assessment about pulmonary pathological changes.

ACKNOWLEDGMENTS

This research is supported by the Recruitment Program of Global Experts (Grant no.01270021814101/022), the Fundamental Research Funds for the Central Universities (Grant no.N151903002) and the Bureau of Science and Technology of Liaoning Province (Grant no.201501146).

REFERENCES

[1] Wang G, Zhang C, Li M, et al. Preliminary Application of High-Definition Computed Tomographic Gemstone Spectral Imaging in Lung Cancer. *J Comput Assist Tomogr*. 2014; 38: 77-81.

[2] Aggarwal P, Sardana H K, Jindal G. Content based medical image retrieval: Theory, gaps and future directions. *ICGST-GVIP J*. 2009; 9: 27-37.

[3] C. B. Akgul, D. L. Rubin, S. Napel, et al. Content-based image retrieval in radiology: current status and future directions. *J Digit Imaging*. 2011; 24: 208-222.

[4] Jinman Kim, Weidong Cai, Dagan Feng, et al. A new way for multidimensional medical data management: volume of interest (VOI)-based retrieval of medical images with visual and functional features. *IEEE T Inf Technol Biomed*. 2006; 10: 598-607.

[5] H. Muller, N. Michous, D. Bandon, et al. A review of content-based image retrieval systems in medical applications-clinical benefits and future directions. *Int J Med Inform.* 2004; 73: 1-23.

[6] Apostolova E, You D, Xue Z, et al. Image retrieval from scientific publications: Text and image content processing to separate multipanel figures. *J Am Soc Inf Sci Technol.* 2013; 64: 893-908.

[7] Egenhofer M J. Query processing in spatial-query-by-sketch. *J Vis Lang Comput.* 1997; 8: 403-424.

[8] Rasiwasia N, Moreno P J, Vasconcelos N. Bridging the gap: Query by semantic example. *IEEE Trans Multimedia*. 2007; 9: 923-938.

[9] Hsu W, Markey M K, Wang M D. Biomedical imaging informatics in the era of precision medicine: progress, challenges, and opportunities. *J Am Med Inf Assoc.* 2013; 20: 1010-1013.

[10] Demner-Fushman D, Antani S, Simpson M, et al. Design and development of a multimodal biomedical information retrieval system. *J Comput Sci Eng.* 2012; 6: 168-177.

[11] Iwano S, Makino N, Ikeda M, et al. Videotaped helical CT images for lung cancer screening. *J Comput Assist Tomogr*. 2000; 24: 242-246.

[12] Depeursinge A, Vargas A, Gaillard F, et al. Case-based lung image categorization and retrieval for interstitial lung diseases: clinical workflows. *Int J Comput Assist Radiol Surg.* 2012; 7: 97-110.

[13] Weissfeld J, Sciurba F C, Nishino M, et al. Subclinical Interstitial Lung Disease Visual Assessment and Computer Quantification on CT Images. *Am J Respir Crit Care Med.* 2014; 189: A6396.

[14] Sun W, Tseng T L B, Qian W, et al. Using multiscale texture and density features for near-term breast cancer risk analysis. *Med. Phys.* 2015; 42: 2853-2862.

[15] Boggs D A, Rosenberg L, Adams-Campbell L L, et al. Prospective Approach to Breast Cancer Risk Prediction in African American Women: The Black Women's Health Study Model. *J. Clin. Oncol.* 2015; 33: 1038-1044.

[16] Cassidy A, Myles J P, van Tongeren M, et al. The LLP risk model: an individual risk prediction model for lung cancer. *Br J Cancer.* 2008; 98: 270-276.

[17] Otsu N. A threshold selection method from gray-level histograms. Automatica, 1975; 11: 23-27.

[18] Zhang F, Song Y, Cai W, et al. Lung nodule classification with multilevel patch-based context analysis. *IEEE Trans Biomed Eng.* 2014; 61: 1155-1166.

[19] Mohanty A K, Senapati M R, Lenka S K. A novel image mining technique for classification of mammograms using hybrid feature selection. *Neural Comput Appl.* 2013; 22: 1151-1161.

[20] Tamura H, Mori S, Yamawaki T. Textural features corresponding to visual perception. *IEEE Trans Syst Man Cybern.* 1978; 8: 460-473.

[21] Guo Z, Zhang L, Zhang D. A completed modeling of local binary pattern operator for texture classification. *IEEE Trans Image Process.* 2010; 19: 1657-1663.

[22] Bishop C M. Pattern recognition and machine learning. Springer, 2006.

[23] Chien J T, Wu M S. Adaptive Bayesian latent semantic analysis. *IEEE Trans Audio Speech Lang Process.* 2008; 16: 198-207.

[24] Rasiwasia N, Vasconcelos N. Latent dirichlet allocation models for image classification. *IEEE Trans Pattern Anal Mach Intell.* 2013; 35: 2665-2679.

[25] Wang Y, Lee J S, Choi I C. Indexing by Latent Dirichlet Allocation and an Ensemble Model. *J Assoc Inf Sci Tech.* 2015; 67: 1736-1750.

[26] Blei D M, Ng A Y, Jordan M I. Latent dirichlet allocation. *J Mach Learn Res.* 2003; 3: 993-1022.

[27] Qiu Z, Wu B, Wang B, et al. Collapsed Gibbs Sampling for Latent Dirichlet Allocation on Spark. *J Mach Learn Res.* 2014; 36: 17-28.

[28] Dahlhaus R. On the Kullback-Leibler information divergence of locally stationary processes. *Stoch Process Their Appl.* 1996; 62: 139-168.

[29] Eitz M, Richter R, Boubekeur T, et al. Sketch-based shape retrieval. *ACM Trans Graph.* 2012; 31: 31.

[30] Leslie W D. Factors Affecting Short-Term Bone Density Precision Assessment and the Effect on Patient Monitoring. *J Bone Miner Res.* 2008; 23: 199-204.

INDEX

A

accessory mental foramina, viii, 24, 26, 33, 34, 35, 37, 38, 41, 42, 43
anatomy, ix, x, 4, 7, 19, 24, 25, 32, 38, 39, 42, 43, 45, 48, 63, 64, 65, 68, 80, 82, 85

B

bifid mandibular canals, viii, 23, 24, 27, 28, 29, 30, 31, 32, 39, 40, 41
biomechanics, 3

C

CAD, 6, 7, 8, 19
CAD/CAM, 6, 7, 8, 19
clinical implications, 31, 35, 61, 84
computed tomography, vii, ix, x, 2, 4, 21, 23, 25, 39, 40, 41, 42, 43, 45, 46, 60, 63, 64, 65, 67, 68, 72, 86, 87, 89, 90
cone beam computed tomography (CBCT), vii, viii, ix, 1, 2, 4, 6, 7, 8, 9, 11, 12, 16, 18, 21, 23, 24, 25, 26, 27, 28, 29, 31, 32, 33, 34, 35, 36, 37, 40, 41, 43, 46, 47, 48, 49, 50, 60, 61, 62, 64, 65, 67, 68, 69, 70, 72, 73, 74, 75, 80, 86

D

dental implant, vii, viii, ix, 1, 2, 3, 7, 18, 19, 20, 24, 31, 35, 36, 45, 47, 48, 61, 62, 64
dentistry, vii, 1, 2, 18, 19, 20, 22, 23, 25, 60, 63, 67, 69, 85

G

greater palatine canal, vii, ix, 67, 68, 71, 72, 73, 74, 75, 80, 81, 82, 83, 84, 85, 86, 87
greater palatine canal length, 80, 81
greater palatine foramen, ix, 68, 70, 71, 72, 73, 74, 75, 76, 77, 78, 79, 80, 82, 83, 84, 85, 86, 87
greater palatine neurovascular bundle, x, 68, 71, 72

I

imaging techniques, 6, 90
innervation, 71
introduction, 2, 18, 25, 46, 68, 90

L

LDA model, 96, 97, 98, 103

M

mandibular canal, vii, viii, ix, 23, 24, 25, 26, 27, 28, 29, 30, 31, 32, 37, 39, 40, 41, 42
mental foramen, vii, viii, 23, 24, 26, 27, 32, 33, 34, 35, 36, 37, 38, 40, 41, 42, 43

N

nasopalatine canal, vii, ix, 45, 46, 47, 48, 49, 50, 51, 52, 53, 54, 55, 56, 57, 58, 59, 60, 61, 62, 64, 65

P

palatal region, 68, 69, 70, 76, 79
premaxillary region, 46, 62
prostetically-driven implantology, 6

R

radiologic analysis, 72
retromolar foramen, 26, 29, 31, 32

S

segmentation, 92, 93

V

vascularization, 71

Z

zirconium dioxide, 3